RAMAN MICROSCOPY STUDIES OF INTERFACIAL CHEMISTRY WITHIN INDIVIDUAL POROUS SILICA PARTICLES

by

Jay Preston Kitt

A dissertation submitted to the faculty of
The University of Utah
in partial fulfillment of the requirements for the degree of

Doctor of Philosophy

Department of Chemistry

The University of Utah

May 2016

The University of Utah Graduate School

STATEMENT OF DISSERTATION APPROVAL

The dissertation of **Jay Preston Kitt**

has been approved by the following supervisory committee members:

Joel Mark Harris	, Chair	**12/4/15** Date Approved
John C. Conboy	, Member	**12/4/15** Date Approved
Shelley D. Minteer	, Member	**12/4/15** Date Approved
Marc D. Porter	, Member	**12/4/15** Date Approved
Ilya Zharov	, Member	**12/4/15** Date Approved

and by **Cynthia J. Burrows**, Chair/Dean of

the Department/College/School of **Chemistry**

and by David B. Kieda, Dean of The Graduate School.

ABSTRACT

Small molecule partitioning between aqueous and lipid-like phases is of importance in pharmaceutics, biology, and environmental chemistry. Measuring small-molecule partitioning has remained a challenge, however, due to the scale of current measurement techniques such as chromatographic columns and shake flasks, which require large sample volumes, long equilibration times, and *ex-situ* quantification steps. In the work presented in this dissertation, confocal Raman microscopy is applied to analyze, *in-situ*, the structure of lipid-like phases within single chromatographic support particles and their application to measuring small-molecule partitioning. The 2μm – 10μm diameter size of a single support particle is well-matched to the size of the confocal probe (~0.6μm diameter, 1 fL) of a 100X confocal microscope. The large (~300m^2/g) surface area within the porous particle concentrates surface-associated molecular populations, providing a large enough 'concentration' within the particle to measure partitioning despite the small cross-sections for Raman scattering. This dissertation covers the evolution of confocal Raman microscopy measurements within individual porous particles from measuring partitioning of pyrene into surface bound C_{18} alkyl chains, detecting octanol-water partitioning of naphthoic acid in reverse-phase chromatographic particles, and characterizing the structure of within-particle hybrid-phospholipid bilayers. This evolution represents a progression toward more biologically-relevant substrates for measuring small-molecule lipophilicity.

To Mom, Dad, and Vicki for a lifetime of support

“We must think critically, and not just about the ideas of others. Be hard on your beliefs. Take them out onto the verandah and beat them with a cricket bat. Be intellectually rigorous. Identify your biases, your prejudices, your privileges.”

— Tim Minchin

TABLE OF CONTENTS

ACKNOWLEDGEMENTS

This text is the culmination of several years of my work in the chemistry department at the University of Utah. What it represents, however, is the dedication of a group of exceptional individuals who have shaped my life, inspired me, pushed me forward, believed in, fought for, and struggled with me along the way.

Joel, your enthusiasm for science, your genuine curiosity for the world around you, and your dedication to your students are second to none. Thank you for always having an open door, for chats and advice about science and life, and for believing in a young man with a less-than perfect record.

David, you are an exceptional friend and colleague. Thanks for putting up with my charging into your office and interrupting you with wild ideas. Our conversations about science are always educational and those about life appreciated.

Eric, your science insight is always appreciated, be it related to lab work or proper preparation of fancy cocktails. The trips to Brewvies have been great.

Doug, we had good times and bad. Let the good times be the ones that stay in our memories. The time we spent climbing and hiking was formative and a great escape from the drear that the city can be.

Harris group members, past and present, Danielle, Grant, Emily, Chaoxiong, Natascha, Mike, Franki, Carol, and Jenna, thank you for making our lab a fun, science

driven atmosphere. It has been great working with you.

Ryan, Gardner, Nikita, David, and Jeremy, I couldn't ask for a better group of friends. Thank you for a lifetime of memories. Anytime you call, it will always seem like it was only yesterday we were up to no good.

Mark, Bonny, and Allegra, thank you for the support you offer and for accepting me with open arms into your family. It means a lot.

Danielle, thank you for being so endlessly supportive. You are great partner who is always there to revel with me in good times and build me up during the bad. Thank you for being patient and kind, and lastly for being willing to try so many of the hair-brained things that I like to call fun. I love you.

Vicki, thank you for being an exceptional big sister. It's the little things. Walking me into school on my first day of junior high. Listening when break-ups would get the best of me. Mill hollow. Going running. New Year's Eve parties. You are a supportive, and caring human and I'm happy our relationship has evolved the way it has.

To my amazing parents: Thank you for always being supportive, for sitting me down and painstakingly getting me through homework assignments as a stubborn young man, for having faith in me even as I tumbled through my high school years, for putting up with phone-calls from teachers and whomever else I managed to get the ire of. I cannot express how much it has meant to have such unwavering support. You have both always been there for me. Mom and Dad, I love you both and hope I can continue to make you proud.

CHAPTER 1

INTRODUCTION

1.1 Porous Silica Particles as Supports for Interfacial Chemistry

Many important chemical processes such as catalysis, biomolecular interactions, adsorption, and molecular separations occur at liquid-solid interfaces. One of the most common materials employed in the study of interfacial chemistry is planar silica (or similarly borosilicate glass). This is due to the stability of silica as a substrate, the ease with which the silica surface can be modified for specific applications using silane chemistry,[1] and because silica is optically transparent and can be used in a wide variety of light-based analytical techniques. Although these properties make planar silica substrates attractive for fundamental studies, planar interfaces are of limited use in process chemistry. This is due to the inefficiency of transport to and away from the interface and also because of the limited 'quantity' of interface in contact with solution. To address the efficiency and capacity challenges of performing chemical processes at silica interfaces, porous silica was developed, and more recently, spherical porous silica particles.[2] These particles are small, typically spherical, 2-μm to 50-μm diameter particles formed from amorphous silicon dioxide which have been physically or chemically modified such that the particle-structure contains voids or pores, which are connected throughout the interior of the structure (Figure 1.1). The surface area associated with the walls of the small (2-50 nm in diameter) pores

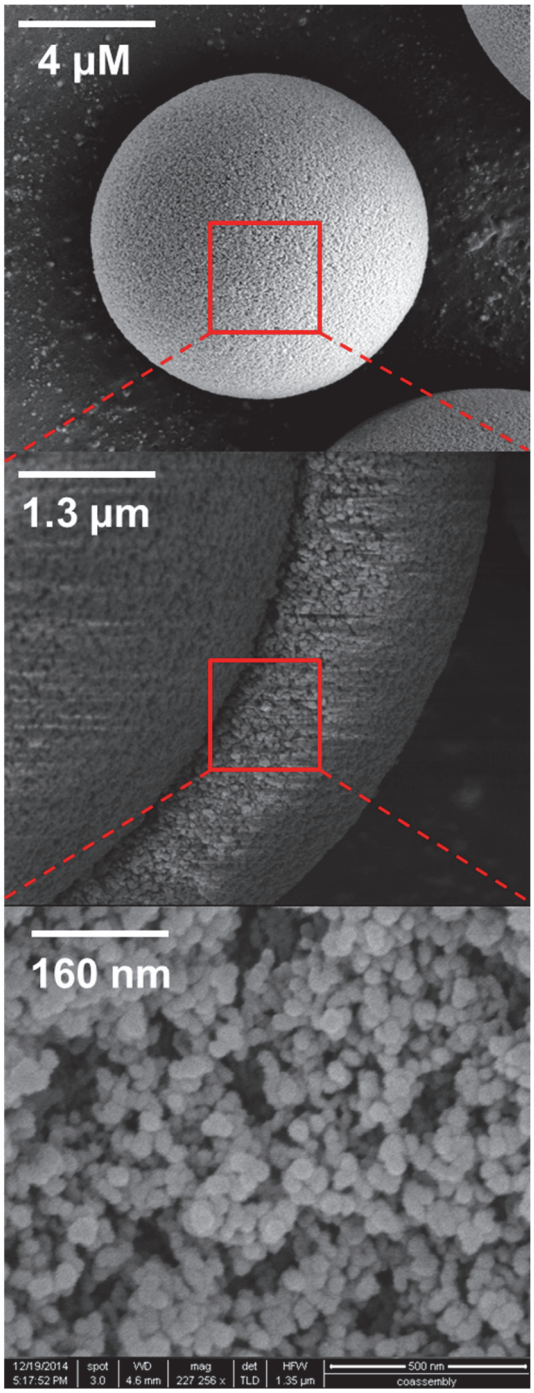

Figure 1.1: Scanning electron microscope image of porous silica particles at various magnification. (The author would like to acknowledge Danielle Montanari for collecting these images)

throughout the particles is immense (50-500 m^2/g), providing high molecular capacity and increased kinetic efficiency for interfacial processes through both increased surface-solution contact and molecular transport to the surface (the time for a molecule to traverse a typical 10 nm pore is ~5 ns).[3] The impact of the development of porous silica as a support for interfacial chemistry applications is immense. Porous silica supports are now used in a wide variety of processes across many disciplines from separations[4-6] and catalysis[7,8] in chemistry to drug delivery in medicine,[9,10] and as potential sorbents for environmental cleanup.[11,12] While implementation of porous silica in process applications has met the efficiency and capacity challenges, it has introduced another: Many of the analytical techniques employed to study planar interfaces cannot probe the "buried" interface within porous silica particles, and planar silica is not a good model of the interface within the highly-curved, interconnected pores in porous silica particles.

1.2 Optical Spectroscopy of Porous Silica Particles

Initially, to meet the challenge of measuring interfacial phenomena within porous silica particles, *ex-situ* optical detection was employed.[13,14] Adsorption was investigated in packed beds of silica particles, where chromatographic elution profiles were measured using chromatography using UV-visible absorption detection, providing insight into interfacial phenomena and transport in packed beds.[15-19] It was recognized that greater insights could be gained by measuring chemical phenomena *in-situ* in packed beds, or on-column, commonly using fluorescence spectroscopy.[20-22] Here, a fluorescent or fluorescently-tagged molecule is employed to monitor on-column chemistry such as kinetics of adsorption or desorption, partitioning, and isotherms. Through these

measurements, within-particle limitations to transport were hypothesized. However, bulk measurements only provide information on ensemble interactions thus, intra- and inter-particle dynamics must be inferred.

More recently, optical spectroscopy was adapted to single-particle investigations using confocal fluorescence microscopy to study interfacial phenomena leading to band-broadening in chromatography.[23] Fluorescence microscopy has continued to be applied within individual particles in single-molecule fluorescence imaging[24] and fluorescence correlation spectroscopy[25,26] to measure slow and fast molecular dynamics within individual particles. Although fluorescence spectroscopy offers the advantage of ultra-low detection limits and allows measurement of fast dynamics, investigations are limited to fluorescent or fluorescently labeled probes.

1.3 Raman Scattering

A label-free technique that is compatible with both silica and typical aqueous chromatographic mobile-phases is Raman spectroscopy. Raman scattering is a linear optical phenomenon where an incident photon interacts with outer-shell electrons in a molecule whose polarizability is modulated by molecular vibrations. Light is inelastically scattered at an energy that differs from the incident energy by the energy of the vibrationally excited state.[27-30] In a classical sense, Raman scattering is the modulation of light of frequency ω_o through interaction with an oscillating polarizability of frequency ω_k. The frequency and intensity of the change can be derived using the equation for the induced electric dipole (Eq. 1).

$$P = \alpha \cdot E \qquad \text{[Eq. 1]}$$

where P is the first order linear induced dipole, α is the polarizability tensor of the molecule, and E is the electric field vector of the incident radiation. The frequency-dependent induced dipole P is then obtained by introducing the frequency dependence of α and E. For α the frequency-dependence (assuming a fixed molecule, and no-rotational motion), is expressed by expanding each component of the polarizability tensor with respect to the normal coordinates of the vibration (Eq. 2).

$$\alpha = \alpha_o + \left(\frac{\partial \alpha}{\partial Q_k}\right) Q_k + \cdots \quad \text{[Eq. 2]}$$

where α_o is the value of the polarizability at the equilibrium configuration and Q_k are the normal coordinates of vibration associated with the vibrational frequency ω_k. Neglecting higher-order vibrations and representing the vibration as a simple harmonic oscillator, we obtain the following equation for the frequency dependent polarizability tensor:

$$\alpha = \alpha_o + \left(\frac{\partial \alpha}{\partial Q_k}\right) Q_k \cos \omega_k t \quad \text{[Eq. 3]}$$

where $\cos(\omega_k t + \delta_k)$ is the time-dependence of the normal-coordinate oscillations. Combining this with the equation for the frequency-dependent incident electric field (Eq. 4) we obtain the equation for the frequency-dependence of the induced dipole (Eq. 5).

$$E = E_o \cos \omega_o t \quad \text{[Eq. 4]}$$

$$P = \alpha_o E_o cos\omega_o t + \left(\frac{\partial \alpha}{\partial Q_k}\right) Q_k E_o \cos(\omega_o t) \cos(\omega_k t) \quad \text{[Eq. 5]}$$

By using the trigonometric identity for the multiplication of two cosines (Eq. 6) we obtain Eq. 7

$$cosAcosB = \frac{1}{2}[\cos(A + B) + \cos(A - B)] \quad \text{[Eq. 6]}$$

$$P = \alpha_o E_o cos\omega_o t + \left(\frac{\partial \alpha}{\partial Q_k}\right) Q_k E_o \cos(\omega_o + \omega_k) + \left(\frac{\partial \alpha}{\partial Q_k}\right) Q_k E_o \cos(\omega_o - \omega_k) \quad \text{[Eq.7]}$$

In Eq. 7, the first term corresponds to Rayleigh scattered light which leaves a molecule

with the same energy (frequency). The second and third terms correspond to anti-Stokes, and Stokes shifted Raman scattered light, respectively. Here the frequency and polarizability dependence of Raman scattering are clear. Raman scattered light lies $\pm\omega_k$ in frequency from the incident photon frequency (this is often depicted in a simplified energy-level diagram as shown in (Figure 1.2)) and the intensity of the scattered light is proportional to the change in polarizability across the normal coordinates of vibration of the induced dipole. The frequency and polarizability dependence of Raman scattering is easily observed in a Raman spectrum of Stokes scattered light from a solution of 50/50 v/v acetonitrile/toluene (Figure 1.3). Here, the vibrational frequency of the Raman active mode defines where the corresponding peak lies on the x-axis and the polarizability change defines the intensity of the scattered light.

Classical theory fails to correctly predict the relative intensities of Stokes and anti-Stokes scattering which are governed by the temperature-dependent Boltzmann distribution of occupied vibrational energy states.[30] Since anti-Stokes scattering occurs from excited vibrational states, the anti-Stokes-scattering intensity is weaker and additionally Raman bands in the anti-Stokes spectrum are temperature-sensitive. Stokes scattering, however, occurs from the ground-vibrational state, thus scattering is more intense, and the temperature sensitivity is minimal under typical laboratory conditions; thus, stokes scattering is more commonly measured.

1.4 Confocal Raman Microscopy

Despite the advantages of Raman spectroscopy, measuring Raman scattering from within an individual porous silica particle could be challenging. Raman scattering is a weak

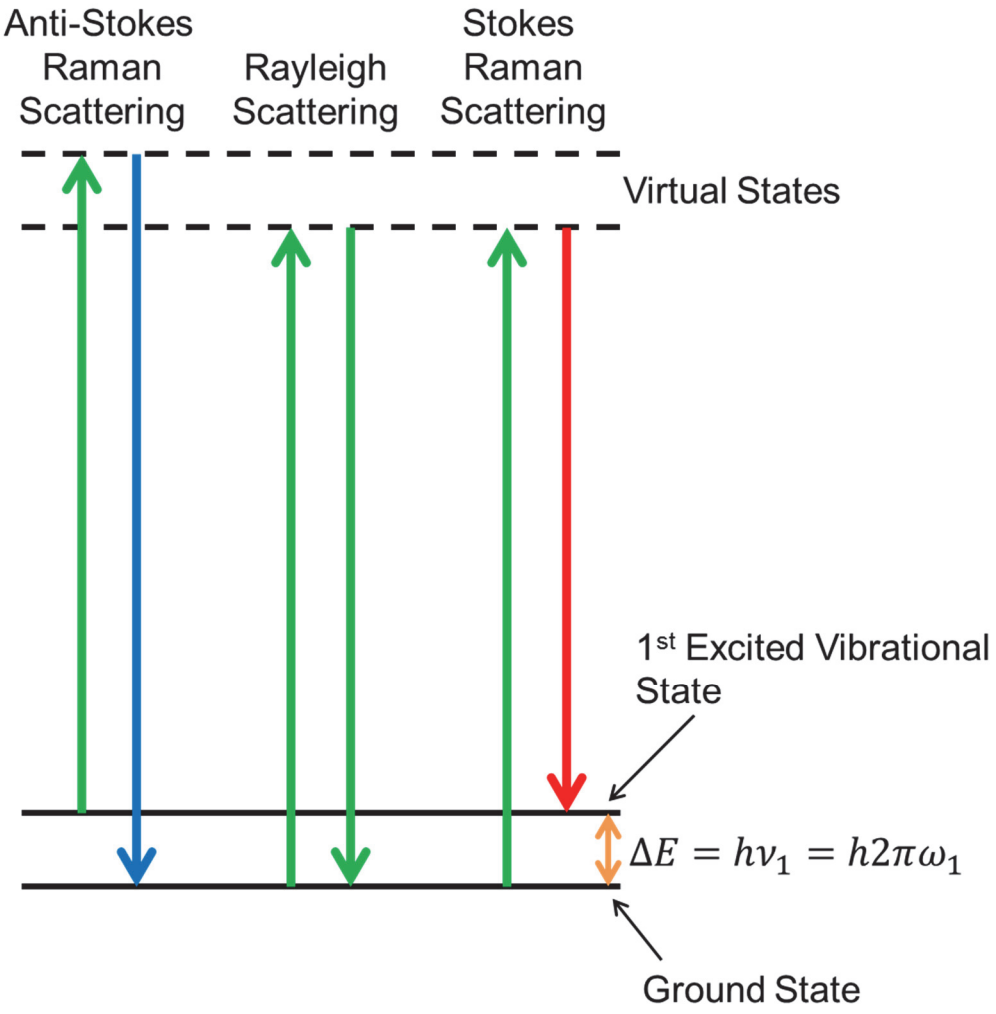

Figure 1.2: Simplified energy-level diagram showing Rayleigh, Stokes-Raman, and anti-Stokes Raman scattering.

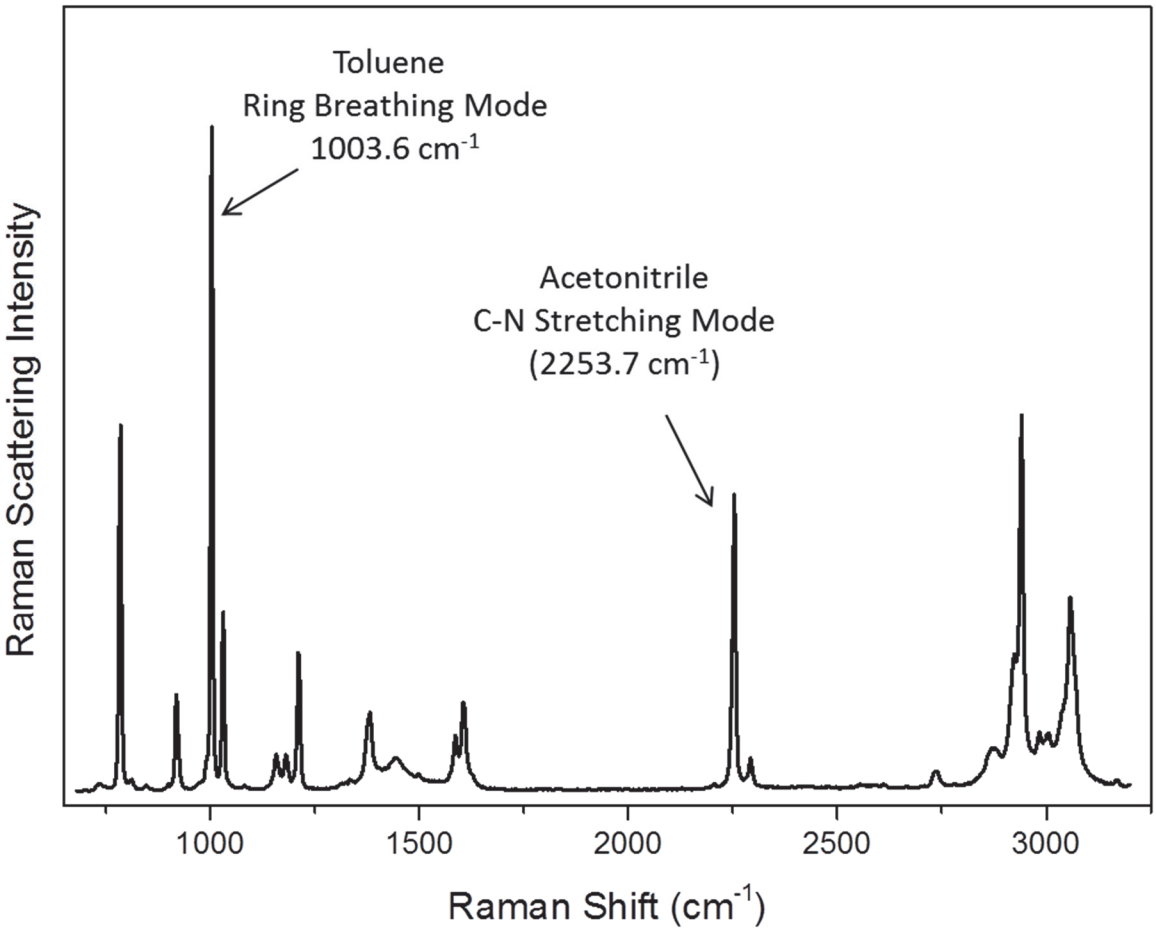

Figure 1.3: Raman spectrum of a 50/50 acetonitrile/toluene spectrum, the wavenumber shifts are proportional to the vibrational energy of the bond being probed, and the scattering intensity is proportional to the change in polarizability during the vibration.

effect (only ~1:10^7 of the incident photons is scattered),[27-30] thus the intensity of the incident radiation must be high enough within a single particle to measure scattering and scattered photons must be collected with high efficiency. Additionally, interference due to Raman scattering from the particle surroundings must be minimized so as not to overwhelm the Raman signal from molecules within the particle.

In this work, the challenges of measuring Raman scattering from within an individual porous silica particle are met using confocal Raman microscopy with a high numerical aperture (NA) objective. A diagram of the one of the two confocal microscopes used in this work is presented in Figure 1.4. Here a Kr^+ laser beam is passed through a laser-line filter, beam expanded, and directed into an inverted fluorescence microscope frame. The expanded beam is reflected from a dichroic mirror to slightly overfill the back aperture of a 100X, 1.4 NA, oil-immersion objective. The beam is focused by the objective to a ~600 nm diameter focal spot within an individual particle. Scattered light is collected through the same objective and passed through the dichroic mirror and an additional long-pass filter to remove Rayleigh scattered light. Raman scattered light is then focused onto the 50 μm entrance slit of a 1:1 imaging spectrograph, dispersed by a diffraction grating and focused onto a charge-couple device (CCD) camera.

By focusing the laser beam to a diffraction limited spot using a high NA objective, the photon flux at the focus is extremely high. At typical laser power of 50 mW using 647 nm laser light, the photon flux is ~3.6×10^{21} photons cm^2 s^{-1}. By collecting light using the same high NA objective, high collection efficiency is achieved with a collection half-angle of ~62 degrees. A confocal optical system (Figure 1.5) is used to avoid background scattering from the particle surroundings. Confocal microscopy relies on a pinhole aperture

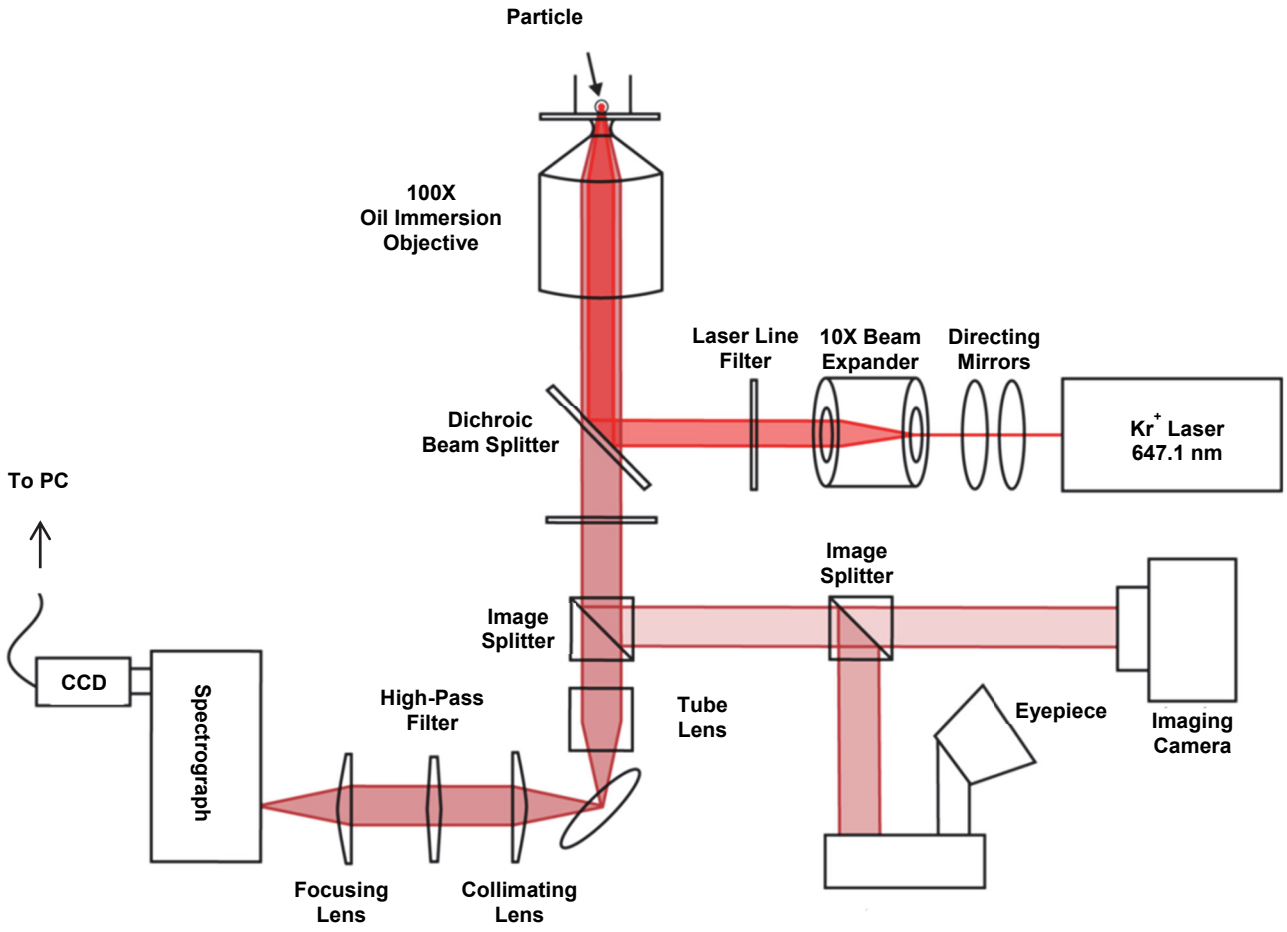

Figure 1.4: Diagram of one of the confocal Raman microscopes used in this work.

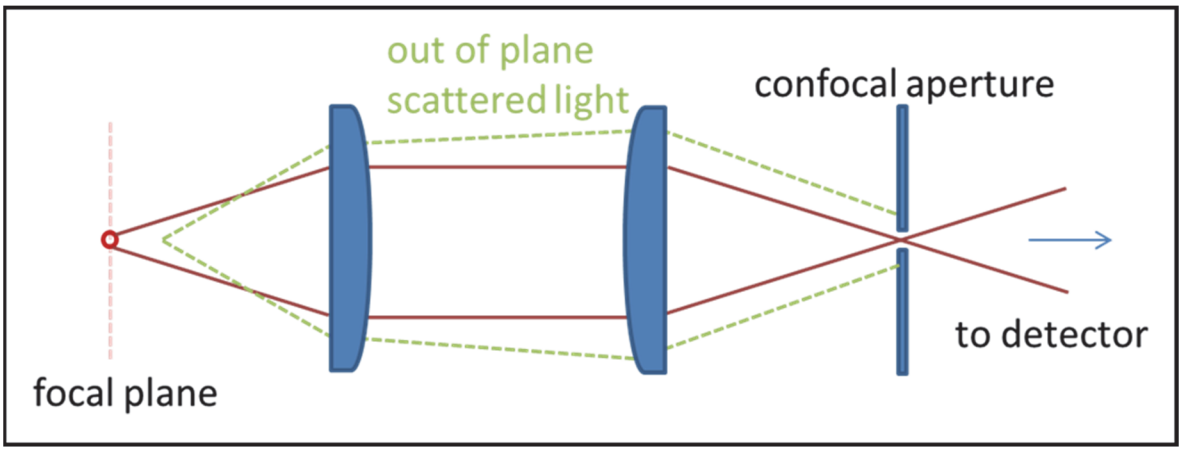

Figure 1.5: Diagram of confocal optics.

in the path of the collected light at a known focal plane which prevents out of plane light from reaching the detector[31] and limits the acquisition to a small (~1 fL) confocal volume. In the current work, no pinhole is used; the confocal aperture is defined by the entrance slit of the spectrograph in the horizontal dimension and by binning a small number of rows on the CCD camera in the vertical dimension (Figure 1.6).[32]

1.5 Confocal Raman Microscopy Investigations of Surface Chemistry within Individual Porous Silica Particles

Porous silica particles are commonly used in interfacial chemistry applications because of the ease with which the silica surface can be chemically modified using silane chemistry.[1,6] A typical approach is to react surface silanols with monomeric or polymeric silane-coupling molecules which carry the functional group needed on the surface for the specific application. Silane molecules for silica surface modification consist of a central silicon atom which is mono, di, or trifunctionalized with good leaving groups such as chloro, alkoxy, or acyloxy functional groups; the fourth bond to silicon is occupied by the functional group that is to be covalently attached to the silica support (Figure 1.7A).[6] The silane molecule can then react with the surface silanols via hydrolytic or anhydrous mechanisms (Figure 1.7B).

To optimize silica functionalization for specific applications both surface coverage and surface structure are important. To probe surface coverage, *ex-situ* techniques such as simple elemental analysis are often employed.[33,34] These *ex-situ* techniques are powerful for determining surface coverages but require large sample sizes and provide no structural information. To examine structure, spectroscopic techniques have been employed at planar

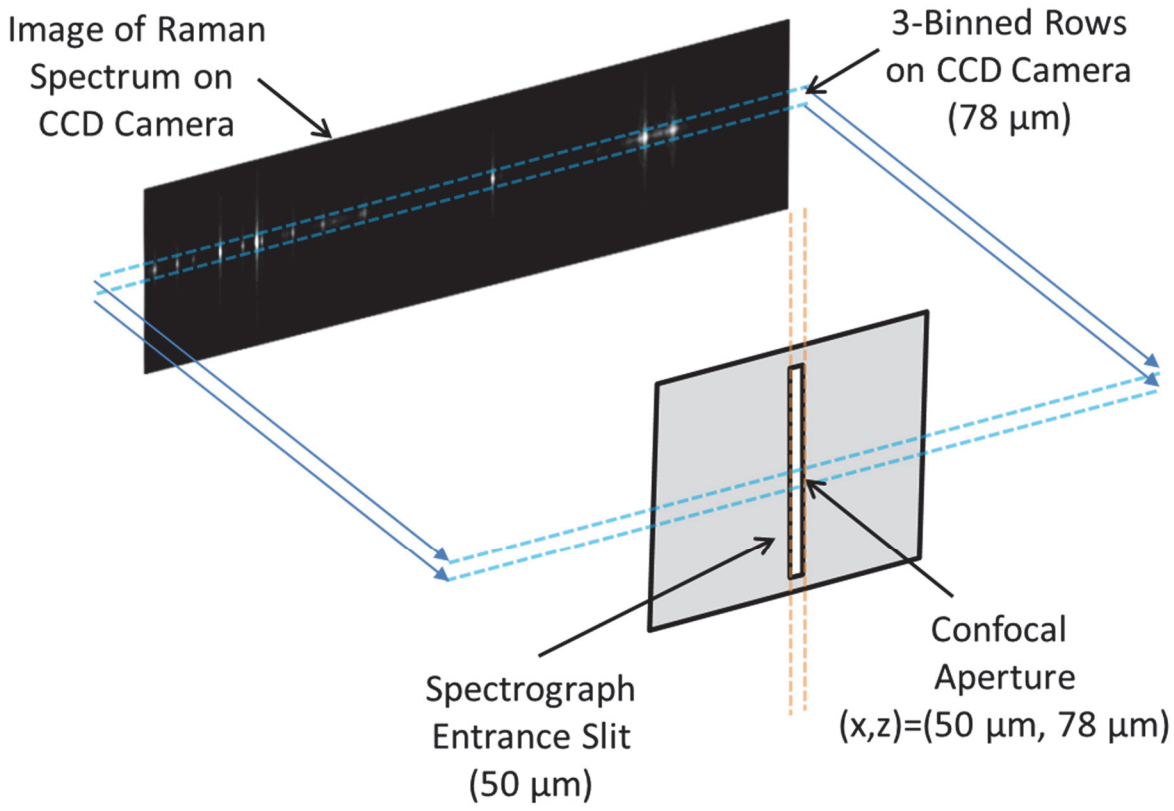

Figure 1.6: Schematic representation of using the spectrograph entrance slit and binning rows of pixels on the charge-couple device (CCD) camera to achieve confocal optics.

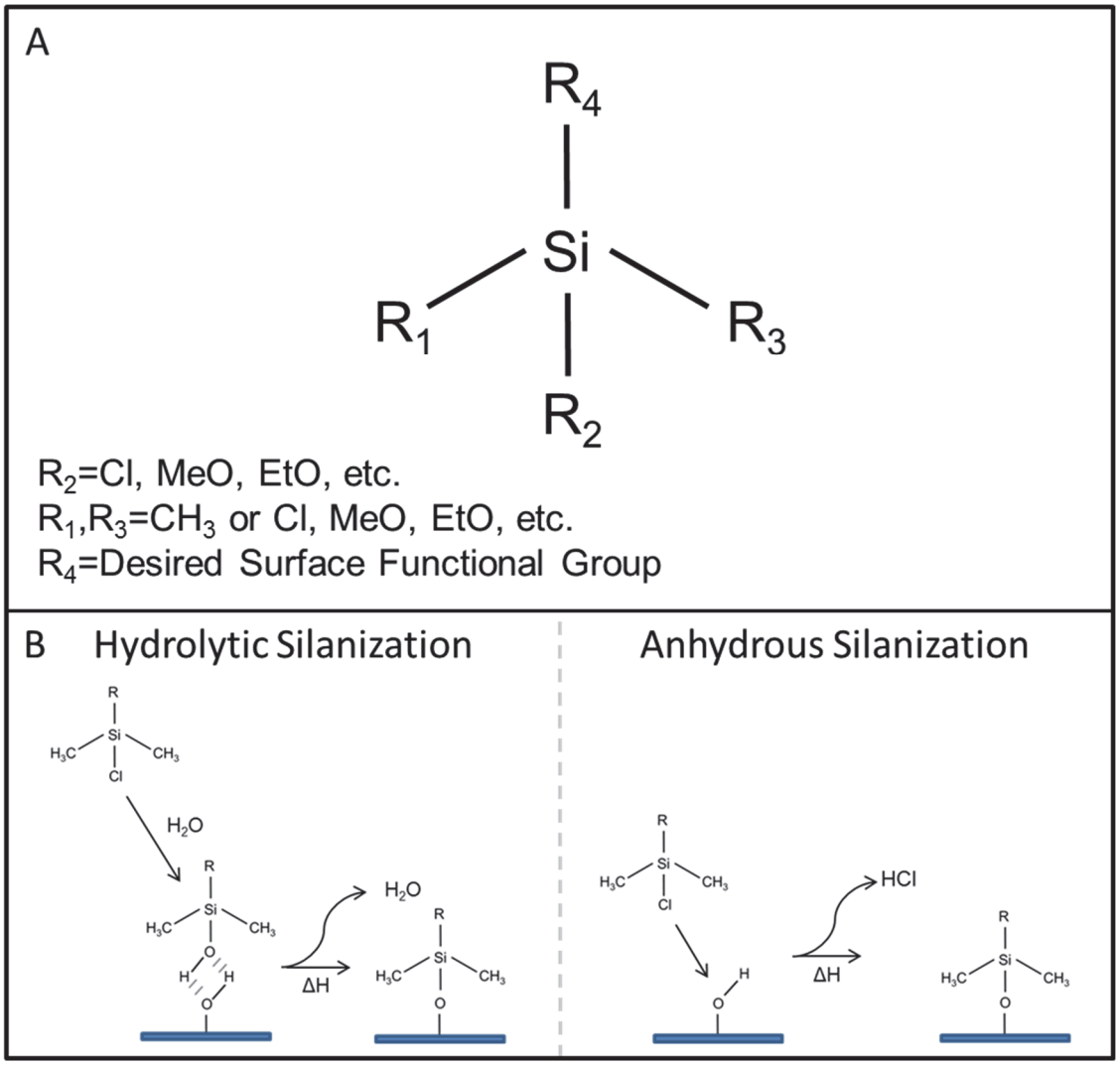

Figure 1.7: A. Silane molecule used for silica surface functionalization. B. The two typical methods of silanization.

interfaces.[35,36] Planar interfaces, however, fail to imitate the interconnected and highly-curved interior surfaces of chromatographic materials. To meet the challenge of investigating silica functionalization using silane chemistry, confocal Raman microscopy was first employed to monitor silane modification and subsequent solid-phase peptide synthesis steps in optically-trapped porous silica particles.[37]

Primary functionalization of the silica interface is typically done with a chemical process application in mind; optimization of this secondary interaction of solution-phase molecules with the functionalized surface (the chemical process) is the goal. An example is chromatography where silica surface functionalization is tailored to allow for optimal separation of chemically similar compounds.[38-40] Raman spectroscopy has been employed previously in chromatography to characterize the structure of covalently bound C_{18}-chains within octadecylsilane-modified chromatographic particles in packed-beds to investigate structure-function relationships in chromatographic separations.[41-46] In other chromatographically motivated work, *in-situ* confocal Raman microscopy within individual chromatographic particles was utilized to investigate interaction of *n*-alkane stationary phases with solution-phase organic modifiers,[47] pore-wetting hysteresis,[48] and surfactant-mediated ion-pair retention.[49]

In the current work, the use of Raman microscopy is extended to measuring partitioning of pyrene into surface bound C_{18},[50], measuring octanol-water partitioning of naphthoic acid in reverse-phase chromatographic particles,[51] and observing the formation and structure of within-particle hybrid-phospholipid bilayers. This evolution in applications represents a progression toward more biologically-relevant substrates for measuring small molecule lipophilicity.

1.6 Confocal Raman Microscopy to Investigate Small-molecule Lipophilicity within Individual Porous Silica Particles

Small molecule partitioning between aqueous and lipid-like phases is of importance in pharmaceutics, biology, and environmental chemistry. Until recently, measuring these partition coefficients was a macroscale process requiring large sample volumes, long equilibration times, and *ex-situ* quantification steps. The aim of this dissertation is the development of confocal Raman microscopy methods for the *in-situ* analysis of small-molecule partitioning into lipid-like phases within single chromatographic support particles. Here, the size of a single support particle (2μm - 10μm diameter) is well-matched to the size of the probe volume of a 100X confocal microscope (~0.6μm diameter). The large (~300m^2/g) surface area within the porous particle concentrates surface-associated populations within a small volume providing a sufficient 'concentration' within the particle to measure partitioning despite the small cross-sections for Raman scattering.

Chapter 2 introduces confocal Raman microscopy as a method for measuring solid-phase extraction (SPE) *in situ* within individual C_{18}-functionalized chromatographic silica particles. In this work, the volume of the collector phase (523 fL) for SPE is decreased by a factor of 10^{-7} compared to the smallest volume employed in previous SPE work. Quantitative measurement of partitioning of pyrene is achieved by using the surface bound-C_{18} chains as an internal standard. The organic modifier concentration in the aqueous phase is varied to investigate the driving force for adsorption, allowing control of pre-concentration into the stationary-phase. This control provides a means to easily expand the dynamic range of the measurement. At the highest volume fraction of water in the source-phase solution (95%), the ratio of the within-particle to solution concentration for pyrene

is 4.8×10^4, and a detection limit from the source phase of 10 nM is demonstrated for pyrene.

In Chapter 3, a more lipid-like phase is used to measure small molecule partitioning. Here, octanol-water partitioning of naphthoic acid in reverse-phase chromatographic particles is measured from octanol which is confined to the pore-structure within the particle. Octanol−water partitioning is one of the most widely used predictors of hydrophobicity and lipophilicity. Traditionally, octanol−water partition coefficients (K_{ow}) are measured using macroscale techniques such as shake-flasks and generator columns. These often require hours for equilibration and large (milliliter) quantities of sample solution. These challenges have led to development of smaller-scale methods for measuring K_{ow}. In this work, the receiver volume for octanol-water partitioning measurements is reduced by six-orders-of-magnitude from current methods, to the femtoliter scale, and the partitioning of naphthoic acid is measured in a single octanol-filled reversed-phase, octadecylsilane-modified chromatographic particle. By eliminating postequilibration phase separation steps, the fluid-handling challenges of working in such small volumes are circumvented. Partitioning is measured *in situ* using confocal Raman microscopy, which is capable of detecting and quantifying a wide variety of molecules. Due to the reduced analyte solution volume required to reach equilibrium in the small-volume collector, equilibration times are fast (less than a minute). The amount of analyte needed to carry out a measurement is less than 50 fmol, which is a useful attribute for drug screening applications. The pH-dependent octanol-water partitioning of naphthoic acid is measured, and the results are compared to both traditional shake-flask measurements and sorption onto C_{18}-modified silica without octanol present within the pores.

Chapter 4 reports on an investigation of within-particle hybrid bilayers, which are currently employed in measuring lipid-membrane partitioning of aqueous-phase small molecules. Hybrid bilayers are stable model membranes which are formed through non-covalent interaction between a phospholipid and an n-alkane-modified surface. Hybrid bilayers for chromatographic applications are generated by adsorption of phospholipids onto n-alkane monolayers covalently bound to porous silica support particles and have been utilized in small-molecule retention studies with promising results. Partition coefficients of many small-molecules and peptides, measured through retention, are in agreement with vesicle bilayer partitioning. However, the structure of the hybrid bilayer within the pore network of chromatographic silica remains uncharacterized. In this work the formation and temperature-dependent structure of hybrid-phospholipid bilayers on C_{18}-modified, porous-silica chromatographic particles is investigated through confocal Raman microscopy and self-modeling curve resolution (SMCR). The highly-porous silica provides a large surface area, where 1,2-dimyristoyl-*sn*-glycero-3-phosphocholine (DMPC) forms a stable monolayer with covalently-bound C_{18}-chains on the interior surface. DMPC hybrid-bilayer formation was monitored as a function of time from 15% isopropanol. DMPC surface coverage is quantified by carbon analysis. By monitoring acyl-chain conformation versus temperature, it was possible to observe the hybrid-bilayer main-phase transition, which is broadened and shifted to higher temperature compared to a DMPC vesicle in agreement with differential scanning calorimetry (DSC) measurements. To understand the nature of melting transitions of hybrid bilayers, Raman scattering from lipid acyl chains was resolved from surface C_{18}-chains by using deuterated DMPC. Raman and DSC measurements indicate hybrid bilayers within C_{18} chromatographic particles are

interdigitated and immobility of C_{18}-chains likely leads to the broadening and higher temperature of hybrid-bilayer phase transitions.

Appendices A and B are methods developed during the dissertation research. In Appendix A, spatial-filtering of a diode laser beam for confocal Raman microscopy is developed.[52] The goal of this work was the development of a simple, inexpensive alternative for gas-ion lasers for use in confocal Raman microscopy. In Appendix B, calorimetrically derived concentration vectors are applied in spectral data analysis to characterize structural changes in thermal phase transitions.[53] Optical-trapping confocal Raman microscopy is combined with differential scanning calorimetry to investigate the temperature-dependent structure of optically-trapped phospholipid vesicle membranes.

1.7 References

(1) Plueddemann, E. P. *Silane Coupling Agents*; Springer Science and Business Media: Berlin, Germany, 2013, pp 31-54.

(2) Iler, R. K. *The Chemistry of Silica : Solubility, Polymerization, Colloid and Surface Properties, and Biochemistry*; Wiley: New York, 1979, pp 462-599.

(3) Bryce, D. A.; Kitt, J. P.; Harris, J. M. *Langmuir*, **2016**, to be submitted for publication.

(4) Majors, R. E. *Anal. Chem.* **1972**, *44*, 1722-1726.

(5) Barnes, J. *High performance liquid chromatography*; Wiley, New York, 1992, pp 149-200.

(6) Hennion, M.-C. *J. Chromatogr. A* **1999**, *856*, 3-54.

(7) De Vos, D. E.; Dams, M.; Sels, B. F.; Jacobs, P. A. *Chem. Rev.* **2002**, *102*, 3615-3640.

(8) Takahashi, H.; Li, B.; Sasaki, T.; Miyazaki, C.; Kajino, T.; Inagaki, S. *Chem. Mat.* **2000**, *12*, 3301-3305.

(9) Chen, J.-F.; Ding, H.-M.; Wang, J.-X.; Shao, L. *Biomaterials* **2004**, *25*, 723-727.

(10) Slowing, I. I.; Trewyn, B. G.; Giri, S.; Lin, V. Y. *Adv. Funct. Mater.* **2007**, *17*, 1225-1236.

(11) Adebajo, M. O.; Frost, R. L.; Kloprogge, J. T.; Carmody, O.; Kokot, S. *J. Porous Mater.* **2003**, *10*, 159-170.

(12) Nooney, R. I.; Kalyanaraman, M.; Kennedy, G.; Maginn, E. J. *Langmuir* **2001**, *17*, 528-533.

(13) Vickrey, T. M. *Liquid chromatography detectors*; CRC Press: Boca Raton, FL, 1983, pp 23-86.

(14) Scott, R. P. W. *Liquid chromatography detectors*; Elsevier: Philidelphia, PA, 1986, pp 89-104.

(15) Miyabe, K.; Guiochon, G. *J. Chrom. A* **2010**, *1217*, 1713-1734.

(16) Miyabe, K.; Guiochon, G. *J. Sep. Sci.* **2003**, *26*, 155-173.

(17) Gritti, F.; Guiochon, G. *J. Chromatogr. A* **2012**, *1221*, 2-40

(18) Miyabe, K.; Guiochon, G. *Adv. Chromatogr.* **2000**, *40*, 1-113.

(19) Miyabe, K.; Guiochon, G. *Anal. Chem.* **1999**, *71*, 889-896.

(20) Carr, J. W.; Harris, J. M. *Anal. Chem.* **1988**, *60*, 698-702.

(21) Carr, J. W.; Harris, J. M. *Anal. Chem.* **1987**, *59*, 2546-2550.

(22) Carr, J. W.; Harris, J. M. *Anal. Chem.* **1986**, *58*, 626-631.

(23) Zhong, Z.; Geng, M. L. *Anal. Chem.* **2007**, *79*, 6709-6717.

(24) Cooper, J. T.; Peterson, E. M.; Harris, J. M. *Anal. Chem.* **2013**, *85*, 9363-9370.

(25) Cooper, J. T.; Harris, J. M. *Anal. Chem.* **2014**, *86*, 7618-7626.

(26) Cooper, J.; Harris, J. M. *Anal. Chem.* **2014**, *86*, 11766-11772.

(27) Hahn, D. W. *Raman Scattering Theory*, URL: http://plaza.ufl.edu/dwhahn/Raman%20Scattering%20Theory.pdf, (accessed November 20, 2015).

(28) Ferraro, J. R. *Introductory Raman Spectroscopy*; Academic Press: Cambridge,

MA, 2003; pp 1-91.

(29) Bernath, P. F. *Spectra of Atoms and Molecules*; Oxford University Press: Oxford, U. K., 2005; pp 293-320.

(30) Haken, H.; Wolf, H. C. *Molecular Physics and Elements of Quantum Chemistry: Introduction to Experiments and Theory*; Springer Science and Business Media: Berlin, Germany, 2013; pp 193-222.

(31) Wilson, T. *Confocal Microscopy,* Academic Press: London, U. K., 1990; p 426.

(32) Williams, K.; Pitt, G.; Batchelder, D.; Kip, B. *Appl. Spectrosc.* **1994**, *48*, 232-235.

(33) Berendsen, G. E.; Galan, L. D. *J. Liq. Chromatogr.* **1978**, *1*, 561-586.

(34) Sander, L. C.; Wise, S. A. *Anal. Chem.* **1984**, *56*, 504-510.

(35) Wirth, M. J.; Fatunmbi, H. O. *Anal. Chem.* **1992**, *64*, 2783-2786.

(36) Thompson, W. R.; Pemberton, J. E. *Anal. Chem.* **1994**, *66*, 3362-3370.

(37) Houlne, M. P.; Sjostrom, C. M.; Uibel, R. H.; Kleimeyer, J. A.; Harris, J. M. *Anal. Chem.* **2002**, *74*, 4311-4319.

(38) Sander, L.; Wise, S. *J. Chromatogr. A* **1993**, *656*, 335-351.

(39) Sander, L. C.; Pursch, M.; Wise, S. A. *Anal. Chem.* **1999**, *71*, 4821-4830.

(40) Sander, L. C.; Wise, S. A. *Anal. Chem.* **1995**, *67*, 3284-3292.

(41) Orendorff, C. J.; Ducey, M. W.; Pemberton, J. E.; Sander, L. C. *Anal. Chem.* **2003**, *75*, 3369.

(42) Orendorff, C. J.; Ducey, M. W.; Pemberton, J. E.; Sander, L. C. *Anal. Chem.* **2003**, *75*, 3360-3375.

(43) Ducey, M. W.; Orendorff, C. J.; Pemberton, J. E.; Sander, L. C. *Anal. Chem.* **2002**, *74*, 5576-5584.

(44) Lippa, K. A.; Sander, L. C.; Mountain, R. D. *Anal. Chem.* **2005**, *77*, 7862-7871.

(45) Ho, M.; Cai, M.; Pemberton, J. E. *Anal. Chem.* **1997**, *69*, 2613-2616.

(46) Ho, M.; Pemberton, J. E. *Anal. Chem.* **1998**, *70*, 4915-4920.

(47) Gasser-Ramirez, J. L.; Harris, J. M. *Anal. Chem.* **2009**, *81*, 2869-2876.

(48) Gasser-Ramirez, J. L.; Harris, J. M. *Anal. Chem.* **2009**, *81*, 7632-7638.

(49) Gasser-Ramirez, J. L.; Harris, J. M. *Anal. Chem.* **2010**, *82*, 5743-5750.

(50) Kitt, J. P.; Harris, J. M. *Anal. Chem.* **2014**, *86*, 1719-1725.

(51) Kitt, J. P.; Harris, J. M. *Anal. Chem.* **2015**, *87*, 5340-5347.

(52) Kitt, J. P.; Bryce, D. A.; Harris, J. M. *Appl. Spectrosc.* **2015**, *69*, 513-517.

(53) Kitt, J. P.; Harris, J. M. *Appl. Spectrosc.* **2016**, in press.

CHAPTER 2

CONFOCAL RAMAN MICROSCOPY FOR IN-SITU DETECTION OF SOLID-PHASE EXTRACTION OF PYRENE INTO SINGLE C_{18} SILICA PARTICLES

2.1 Introduction

Solid-phase extraction is a well-characterized method for the preconcentration of analytes prior to detection and quantification. In solid-phase extraction, an analyte is concentrated from solvent solution by adsorption onto a functionalized support material. Adsorption is governed by the affinity of the analyte for the solvent phase versus the extractor and can be controlled by varying the solvent composition or material composition.[1-3] Previous work in solid-phase extraction has involved the use of an extraction column on the macro-scale,[2] or a modified syringe containing an adsorbent coated fiber on the micro-scale.[1] In either case, the analyte containing solvent phase is equilibrated with a solid-phase adsorbent for which the analyte has high affinity. The adsorbed analyte is then removed from the solvent phase and rinsed or desorbed to allow

---

Adapted with permission from: Kitt, J.P.; Harris J.M.; Confocal Raman Microscopy for in Situ Measurement of Octanol–Water Partitioning within the Pores of Individual C_{18}-Functionalized Chromatographic Particles, Anal. Chem., 2015, 87 (10), 5340-5347, DOI: 10.1021/acs.analchem.5b00634.

ex-situ quantification, often using gas chromatography, mass spectrometry, or high-performance liquid chromatography.[1-3]

Recent advances in microfluidics, the development of lab-on-a-chip systems, and the need for detection in small biological samples, have led to a drive for reducing the spatial scale of analytical methods. The miniaturization of solid-phase extraction has been attempted in various ways, including monoliths of porous polymeric channels,[4] surface functionalized capillaries[5,6] and membranes,[7] and miniature packed beds.[8] Although all of these methods allow extraction of low-concentration analytes into small collection volumes, they have not led to detection in equivalently small sample volumes because generally the analyte is transferred or washed into a larger solution volume for detection. This problem indicates that further miniaturizing the collector will not be effective at reducing detection volumes unless the excess dilution of a wash-off step is eliminated.

In-situ detection within the collection phase provides a simple means of avoiding dilution from wash-off. In earlier work using *in-situ* detection within a collection phase, accumulation of polycyclic aromatic hydrocarbons (PAHs) onto a bed of C_{18}-functionalized silica particles packed into a 40-μL quartz tube, was monitored by detecting UV-excited fluorescence from PAH compounds concentrated in the C_{18} particles.[9] Accumulation of pyrene from a 50/50 methanol/water solution, combined with *in-situ* detection, produced a 250-fold higher concentration in the packed bed and a 200-fold lower detection limit compared to a fluorescence measurement of the source-phase solution. Accumulation from a solution of lower (5%) methanol concentration could have increased the preconcentration factor by nearly two more orders,[9] but the solution volume required to equilibrate the packed bed would have exceeded 100 mL, requiring hours to

pump through the minicolumn. Extraction of aromatic compounds (benzene, toluene, ethylbenzene, and xylenes) from water into millimeter-sized (5-50-μL) beads of polydimethylsiloxane (PDMS) polymer has been monitored by *in-situ* Raman spectroscopy detection within the PDMS.[10,11] These studies utilized extraction into beads equilibrated with 20- to 45-mL of aqueous source-phase solution, followed by isolation of the bead and within-bead analysis by Raman spectroscopy. Detection limits for aromatic hydrocarbons were 100- to 1500-fold lower in concentration depending on the compound,[10] factors that were comparable to the measured partitioning of these compounds into PDMS from aqueous solution.[11]

In the present work, we propose to reduce the volume of the collector phase for solid-phase extraction *by a factor of* 10^{-7} compared to the smallest volume employed in the studies above. The proposed collection phase is a single C_{18}-derivatized chromatographic silica particle, the interior volume of which can be probed *in situ* with submicrometer resolution and high collection efficiency using confocal Raman microscopy.[12] Confocal Raman microscopy has previously been employed to probe the surface chemistry of individual porous silica particles in an investigation of surface derivatization reactions.[13] More recent research focused on characterizing the interfacial solvation environment within reverse-phase (C_{18}-modified) chromatographic particles. These investigations included examination of interactions of the n-alkane stationary phase with organic modifiers,[14] pore-wetting hysteresis,[15] and surfactant-mediated ion-pair retention.[16] The current work extends the probing of individual chromatographic particles with femtoliter volume resolution by confocal Raman microscopy into the field of solid-phase extraction on the femtoliter volume scale. The use of an individual C_{18}-functionalized

chromatographic particle as a collector phase is demonstrated, the utility of Raman scattering from the surface-bound C_{18} chains as an internal standard is established, and control of the partitioning equilibrium and preconcentration factor is achieved by varying the organic modifier concentration.

2.2 Experimental Section

2.2.1 Reagents and Materials

Chromatography particles were obtained from Phenomenex [Luna C18(2), Torrence, CA]. The particles were spherical, monofunctional, C_{18} derivitized and capped with trimethychlorosilane. They have a mean diameter of 10 μm as reported by Phenomonex; their mean pore diameter is 90 ± 30 Å. Their specific surface area is 218 m^2/g, and the pore volume is 0.53 cm^3/g as determined from nitrogen Brunauer-Emmett-Teller (BET) measurements (Porous Materials, Inc, Ithaca, NY). The surface coverage by C_{18} chains of 3.6 $\mu mol/m^2$ was determined from elemental analysis (MHW Laboratories, Phoenix, AZ) and the specific surface area. The density of the skeletal portion of the C_{18}-silica particles (1.85 ± 0.02 g/cm^3) was determined by methanol displacement of a known mass of stationary phase. The overall particle density was determined from the skeletal density and porosity of the particles as reported by nitrogen BET measurements.

Methanol (Omnisolve, >99.9%) was obtained from EMD Millipore USA (Billerica, MA). Pyrene (Puriss., >99.0%), hexadecane (Reagent Plus, 99%), pentadecane, decane, hexane, pentane, and chloroform (all Chromasolv Plus, >99.9%) were obtained from Sigma-Aldrich (St. Louis, MO). Water used for these experiments was filtered using a

Barnstead GenPure UV system (ThermoFisher Scientific, Waltham, MA) and had a minimum resistivity of 18.0 MΩ·cm.

Microfluidic flow cells for *in-situ* Raman microscopy were constructed by drilling two 2.5-mm holes in a 25-mm diameter by 3-mm thick Pyrex glass top plate (VWR, Radnor, PA) and attaching 2.4-mm o.d. Luer adapters (Value Plastics, Inc., Fort Collins, CO) using Devcon 5-min epoxy (ITW Devcon, Danvers, MA). The top plate was stuck to a 22 mm × 22 mm No. 1 glass coverslip (Gold Seal, Erie Scientific Co., Portsmouth, NH) using 140-μm 3M double-stick tape (TapeCase Ltd., Elk Grove Village, IL) where a 2.5-mm by 11-mm channel has been cut into the tape allowing flow through a channel between the Luer adapters. All tubing used was 1.6-mm i.d. × 2.4-mm o.d. Viton elastomer (Cole-Parmer, Vernon Hills, IL). Microscopy well cells for measuring solution standards were constructed by attaching a 12-mm length of 10-mm i.d., 13-mm o.d. Pyrex glass tubing to a No. 1 glass coverslip using Devcon 5-min epoxy (ITW Devcon, Danvers, MA). Diagrams of both cell designs are presented in Figure 2.1.

2.2.2 Sample Preparation and Characterization

A microfluidic flow cell was used for studies of the preconcentration equilibria to ensure that a constant concentration of pyrene was available at the C_{18}-particle surface. C_{18} particles were pre-wetted by dispersion into methanol. Methanol-wetted particles were injected into the flow cell and allowed to settle; the flow cell was then placed in a 120˚C oven for 5 min to evaporate the methanol and allow particles to adhere to the glass coverslip surface. Particles were then re-wetted with methanol. To be sure the particles did not retain methanol during pyrene accumulation experiments, particles were pre-equilibrated with a

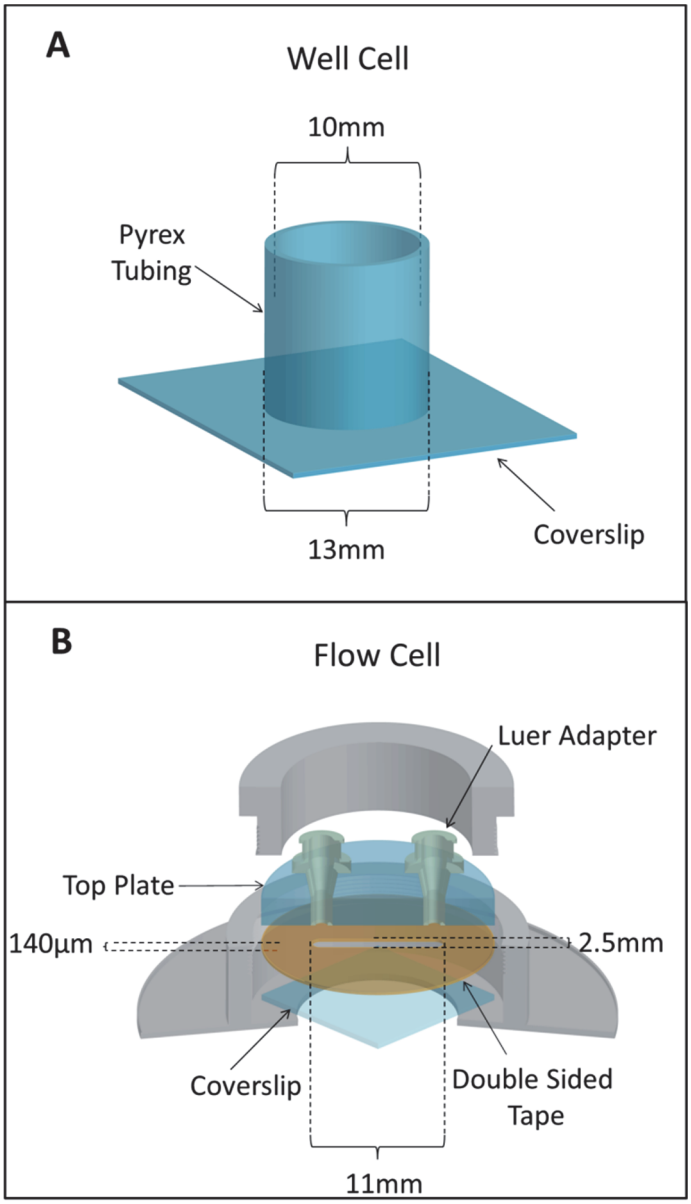

Figure 2.1: Raman microscopy cell designs. A. Well cell for measuring solution-phase standards. B. Flow cell for *in-situ* measurements of preconcentration into surface-attached C_{18} particles.

methanol-water blank solution matching the one to be used in the accumulation. Flow was maintained using a syringe pump (Harvard Pump 11 Plus, Harvard Apparatus, Holliston, MA) operating at 0.25 mL/min until the ratio of methanol-to-water Raman scattering within the particle matched that of the solution outside the particle. At this point, the pyrene-containing solution was introduced. The confocal volume was focused in the center of the particle and the interior composition was monitored spectroscopically until pyrene-derived peaks were no longer changing relative to those of the C_{18} chains, after which time, Raman spectra for quantitative analysis were acquired from the interior of several individual particles.

For determining the relative Raman scattering from pyrene compared to n-alkane chains for quantitative analysis, three pyrene-hexadecane standards were prepared in 50:50 v/v hexadecane/chloroform. An aliquot from each standard was placed in a simple microscopy well cell for spectroscopic measurement. Standards for determining the dependence of Raman scattering intensity versus the number of methylene groups were prepared with 0.5 M concentrations of five different linear hydrocarbons in chloroform. Three spectra each of these standards were measured and analyzed.

2.2.3 Confocal Raman Microscopy

A block diagram of the confocal Raman microscope used in this work has previously been published;[13,17] minor modifications to the microscope for this work are included in the following description. Briefly, the beam of a Kr^+ laser (Innova 90, Coherent Inc., Santa Clara, CA) operating at 647.1 nm and 50 mW of laser power is directed through a band-pass filter (LL01-647-12.5, Semrock, Lake Forest, IL). The beam was then passed

through a 4× beam expander (50-25-4X-647, Special Optics Inc., Wharton, NJ) mounted on the body of a Nikon TE 300 inverted fluorescence microscope (Nikon Inc., El Segundo, CA). The expanded beam was then directed through another band-pass filter (D647/10, Chroma Tech Inc., Bellows Falls, VT) and reflected by a dichroic beam splitter to slightly overfill the back of a 1.4-NA 100× oil-immersion microscope objective (CFL PLAN APO, Nikon Inc., El Segundo, CA). The laser beam was focused by the objective to a ~600nm diameter spot within a single particle. Raman scattering from the confocal volume was collected back through the objective. The Raman scattering was then transmitted back through the dichroic beam splitter, and passed through a high-pass filter (E660LP, Chroma Tech Inc., Bellows Falls, VT) and a holographic notch filter (Kaiser Optical Systems Inc., Ann Arbor, MI). The scattered light was then focused on a monochromator slit set to 50 μm (500 IS, Bruker Corp., Preston, Victoria, AUS) defining the horizontal dimension of the confocal aperture. The vertical aspect was defined[18] by limiting spectral acquisition to three rows of pixels (78 μm) on the charge-couple device (CCD) detector (DV420, Andor Technology USA, South Windsor, CT). Spectra were acquired using a diffraction grating with 300 lines/mm blazed at 750 nm with a resolution of 2 cm^{-1}.

For intraparticle spectroscopy, the laser was brought to focus at the coverslip-solution interface. A single particle was then centered over the focus spot by manipulating the microscope stage in the *x* and *y* dimensions. The microscope objective was then translated upward by 5 μm such that the laser was focused at the center of the spherical particle; Raman spectra from the center of the particle were acquired for 60 s. Raman spectra of standard solutions (hexadecane and pyrene and a series of linear hydrocarbons in chloroform) were acquired from ~300-μL aliquots of each standard in a covered

microscope well cell. The laser focus was brought to the coverslip-solution interface and then translated 5 μm into the solution; Raman spectra of the solutions were measured with 60-s exposures, and three spectra of each of the three standards were acquired and averaged. All spectra were corrected using a program executed in Matlab (MathWorks, Natick, MA) program, which subtracted a dark spectrum offset and ratioed the data to a white-light reference spectrum. The spectra were then background corrected by subtraction of a seventh-order polynomial fitted to non-peak-containing regions of the spectrum, and Gaussian shapes were fit to the Raman scattering band to determine their areas (Figure 2.2).

2.3 Results and Discussion

2.3.1 Collection of Raman Scattering from the Interior of Silica Particles

To optimize the collection of Raman scattering from the interior of a particle, the laser focus from the objective was brought to a focused spot at the coverslip-solution interface, and a C_{18}-silica particle was manipulated by *x* and *y* motion of the microscope stage to be centered above the spot. The objective is then translated 5-μm upwards to bring the laser focus and confocal volume into the center of the particle. In Figure 2.3, a bright-field illuminated image of a C_{18} particle adhered to a coverslip is shown, along with the laser spot, first focused at the coverslip-solution interface below the particle and then translated 5 μm upward into the center of the particle. This z-axis motion not only moved the laser focus into the particle center, but also localized the image plane of microscope camera and confocal aperture (spectrometer entrance slit and 3 binned rows on the CCD[18])

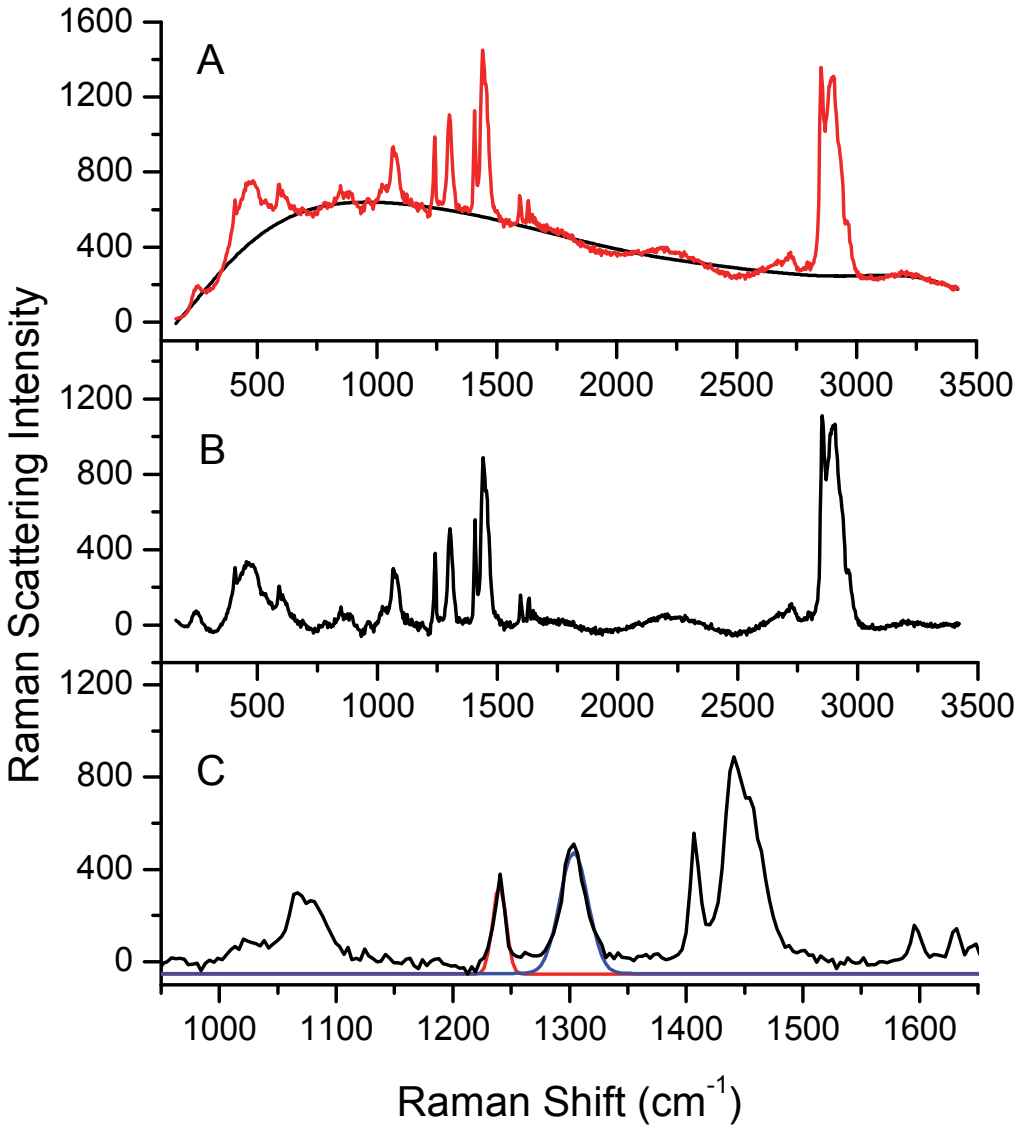

Figure 2.2: Raman spectra of pyrene within a C_{18} particle. A. Spectrum prior to polynomial baseline correction. B. Spectrum following baseline correction. C. Spectroscopic peaks fitted to Gaussian shapes. The peak at 1241cm^{-1} corresponds to the pyrene ring stretching mode. The peak at 1303cm^{-1} corresponds to the CH_2 twisting mode from the surface C_{18} chains.

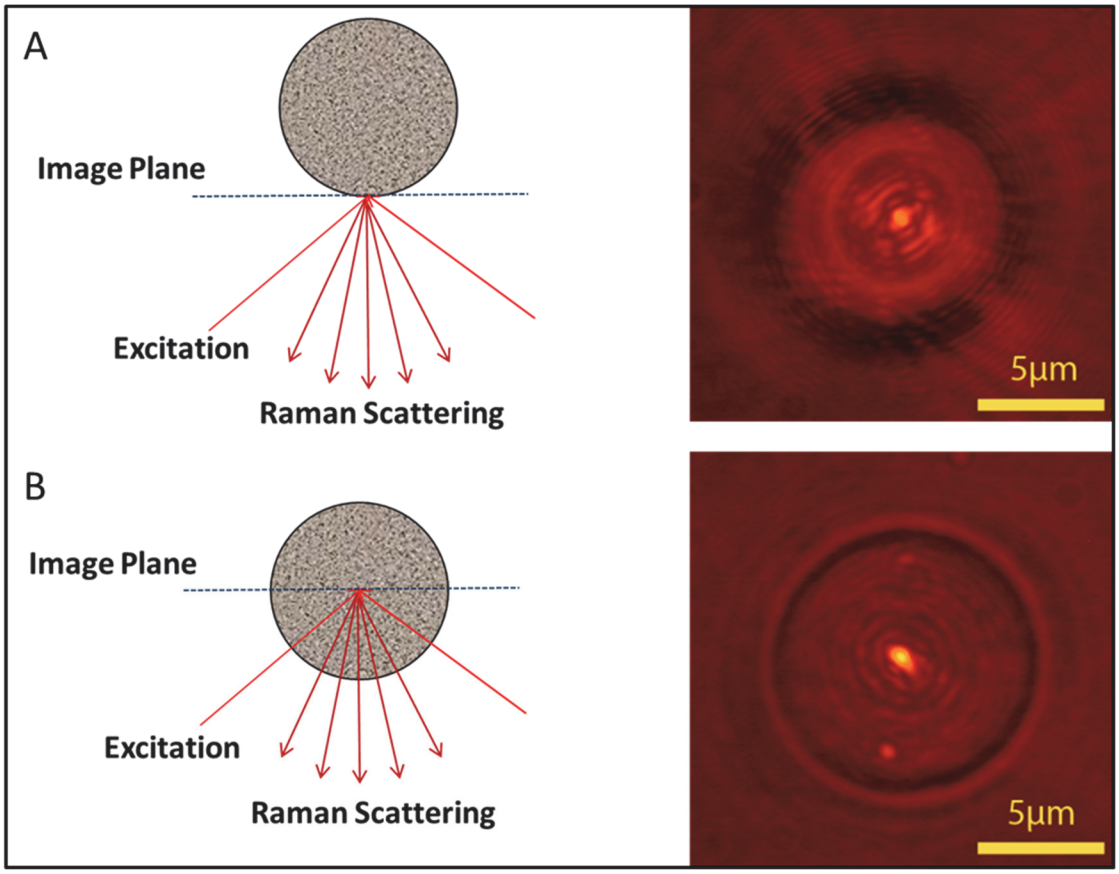

Figure 2.3. Centering of the confocal probe volume in an individual C_{18} particle. A. The laser spot brought to focus at the coverslip-solution interface below a particle. Note the edges of the particle are out of focus. B. The laser spot and image plane are raised 5 µm into the center of the particle. Note: The edges of the particle are brought into sharp focus, and the diffraction limited spot size of the focused laser beam is maintained.

at the same distance above the coverslip and produced a diffraction-limited spot (~600 nm diameter) from the laser excitation in the image of scattered light. Because the silica material is highly porous, one might anticipate significant loss of image fidelity due to scattering from the pores. Nevertheless, it is evident in Figure 2.3B that the integrity of the focused beam and its scattered radiation was well maintained at the center of the particle. This is not a surprising result, however, because the 10-nm silica pores were much smaller (1/60th) than the wavelength of the excitation light and the refractive index difference between the silica and methanol/water solutions was also small, <10%. This result assured that the Raman scattering was excited and collected from a small (< 1 fL) confocal volume at the center of the C_{18}-silica particle with no interference from the interparticle solution.

Measuring Raman scattering from the center of individual silica particles improves the quantitative reproducibility of detecting interfacial molecular populations preconcentrated onto the C_{18} surface. Unlike *in-situ* detection within a packed bed of silica particles,[9] intraparticle spectroscopy is not influenced by the reproducibility of particle packing density and depends only on the particle-to-particle reproducibility of the pore structure and surface coverage of C_{18} chains. Within a given manufacturing lot of C_{18}-silica particles, the particle-to-particle reproducibility of the accessible C_{18} surface is excellent. To illustrate this point, unscaled Raman spectra from the interior of four C_{18}-functionalized silica particles in methanol are plotted in Figure 2.4. Raman scattering at 1303 cm^{-1} is derived solely from the CH_2-twisting mode of the C_{18}-methylene chains[16,18] and acts as an effective indicator of surface functionalization homogeneity. The results show less than 5% particle-to-particle variability in the amount of C_{18} ligands detected within the confocal volume. The area of the CH-bending mode at 1454 cm^{-1} is dominated (> 70%) by methanol

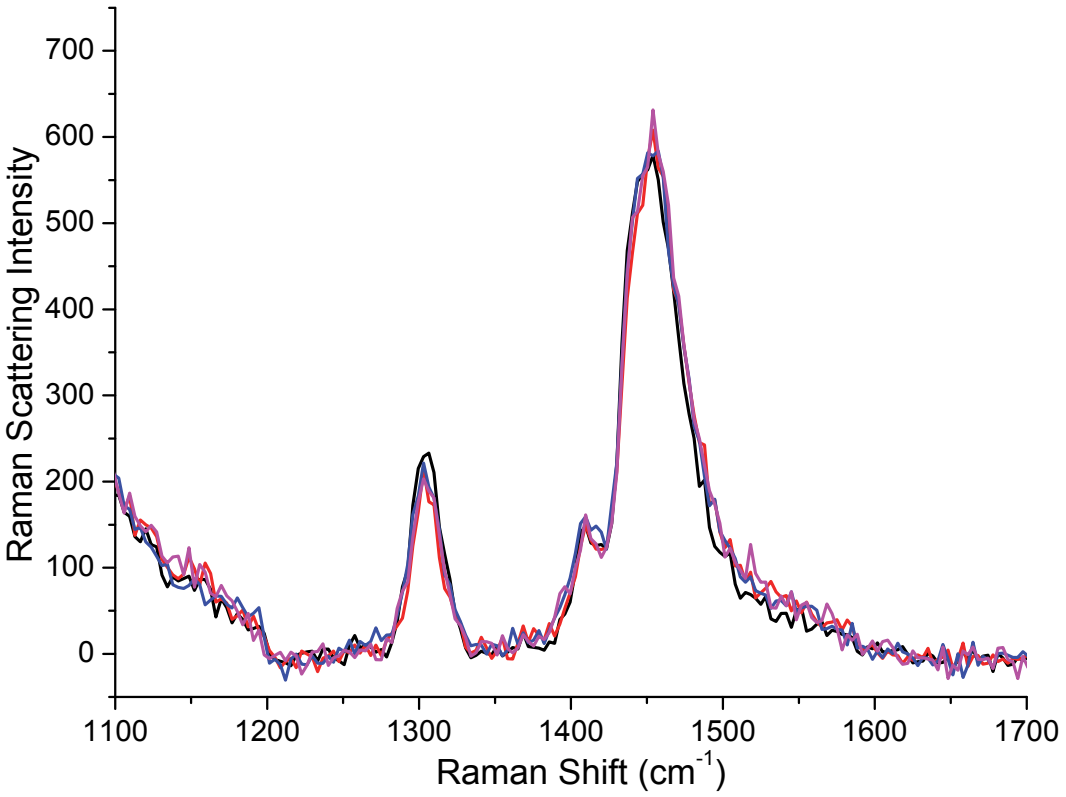

Figure 2.4. Raman scattering of the CH_2-twisting mode of the C_{18} chains at 1303 cm^{-1} and CH bending at 1454 cm^{-1}, the latter peak area is dominated by methanol in the pores. Spectra from four different particles were plotted with no scaling.

in the pores and shows equivalent (<5%) variability. These combined results demonstrate that the particle-to particle internal porosity and surface functionalization are very homogeneous, which should provide reliable and reproducible extractions when measured within individual particles.

2.3.2 Quantitative Solid Phase Extraction of Pyrene into Individual C_{18} Particles

To detect extraction of a model polycyclic aromatic hydrocarbon (pyrene) into an individual particle, Raman scattering was measured from within the particle following equilibration with a series of 80:20 (v/v) water/methanol solutions having pyrene concentrations that ranged from 0.025 to 15 μM. In the resulting spectra (Figure 2.5A), peaks corresponding to the pyrene ring breathing mode at 1241 cm^{-1} and the pyrene carbon-carbon stretching mode at 1404 cm^{-1} clearly grew in as the concentration of pyrene in the source phase was increased. The CH_2-twisting mode of the surface-bound hydrocarbon chains at 1303 cm^{-1} remained constant, demonstrating that the efficiency of collecting Raman scattering from the C_{18} particle is unchanged.

Quantification of pyrene within a single chromatographic particle was accomplished using the surface-bound C_{18} chains as an internal standard. It has been demonstrated previously that Raman scattering peak area from the CH_2-twisting mode of the n-alkane chains is insensitive to chain conformation.[16,19] Furthermore, the results presented above indicate that Raman scattering from the CH_2 twisting mode remained constant during analyte accumulation and from particle-to-particle (see above), demonstrating that it is a reasonable choice for use as an internal standard. Thus, from the

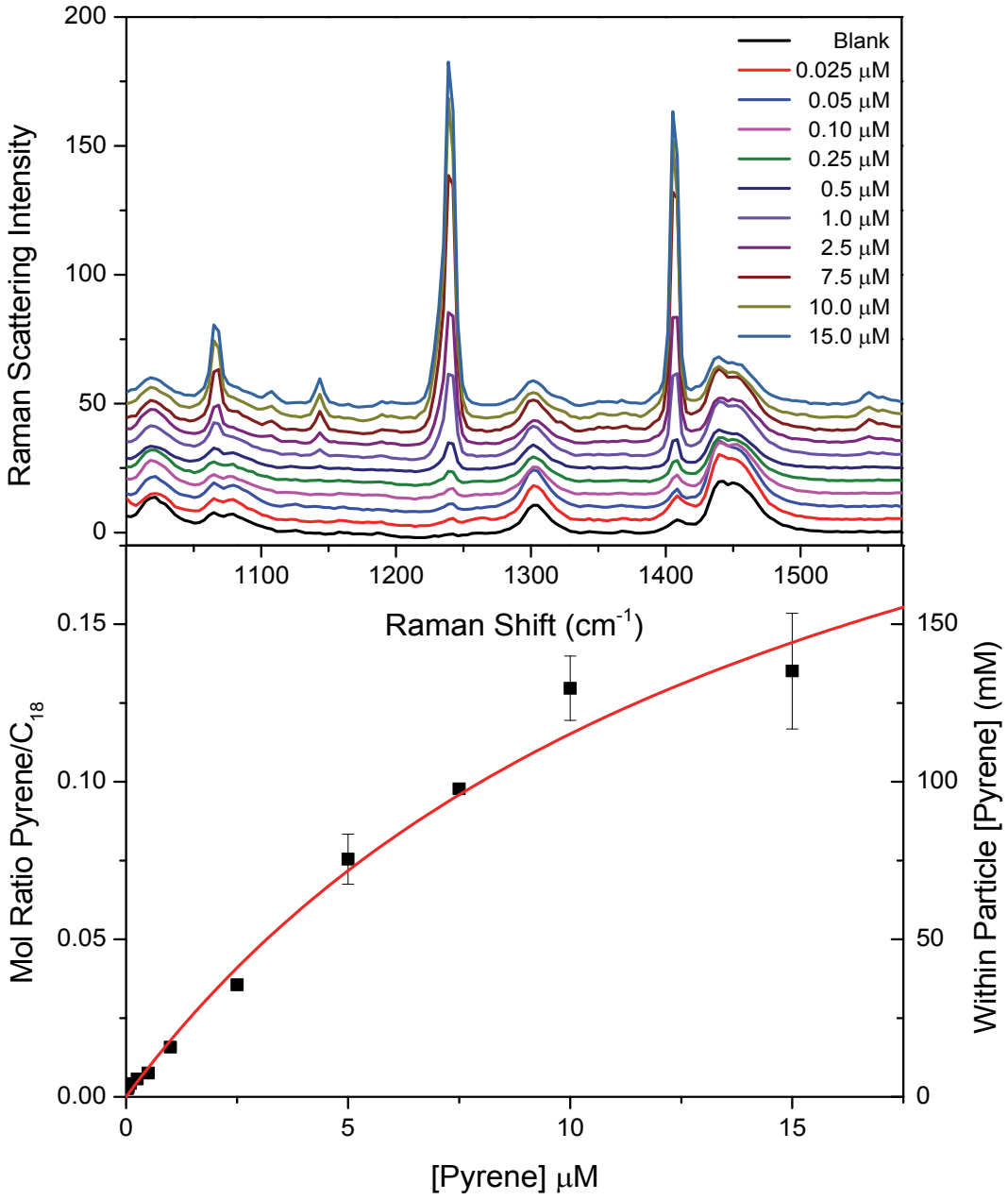

Figure 2.5. Spectroscopic isotherm for pyrene accumulation on a C_{18}-silica particle. A. Within-particle Raman spectra for concentrations of pyrene increasing from 250 nM to 15 μM in 80% H_2O/20% methanol source phase. B. Plot of the isotherm resulting from analysis of the Raman scattering data (see text).

ratio of the *in-situ* scattering from the analyte to that from the intraparticle C_{18} chains, it should be possible to determine the mole ratio of pyrene to C_{18}-chains within a porous silica particle.

To calibrate the Raman scattering response from pyrene relative to the scattering of an n-alkane, Raman spectra of standard solutions of hexadecane and pyrene in chloroform were acquired. Peak areas of the pyrene ring-breathing mode at 1241 cm^{-1} and CH_2-twisting mode of hexadecane were determined from least squares fits of the peaks to Gaussian functions and evaluation of the integrals of the functions to obtain their areas. The peak area of the CH_2-twisting mode of hexadecane was then ratioed to that of the pyrene ring-breathing mode and multiplied by the ratio of the molarities of pyrene to hexadecane in the standards to obtain the relative scattering efficiencies of hexadecane to pyrene. To correct for the number of CH_2 groups in C_{18} versus hexadecane, the peak area ratio is corrected by a factor of 17/14. This correction factor assumes that the CH_2 spectral response depends only on the number of CH_2 groups per chain; this assumption was tested by examining the chain-length dependence of the CH_2 scattering from a series of different-length linear hydrocarbons at the same solution concentration. The results (Figure 2.6) clearly demonstrate a linear relationship between scattering intensity from the CH_2-twisting mode and the number of methylene groups in a linear hydrocarbon.

The factor that then converts measured scattering intensities (band areas) of pyrene and C_{18} into pyrene/C_{18} mol ratios is defined from the relative peak areas and concentrations of the hexadecane and pyrene standards as

$$F = \frac{A_{hexadecane}}{A_{pyrene}} \frac{[pyrene]}{[hexadecane]} \frac{17\ CH_2}{14\ CH_2} \qquad \text{[Eq. 2.1]}$$

To determine the pyrene surface coverage within a particle, Raman scattering from

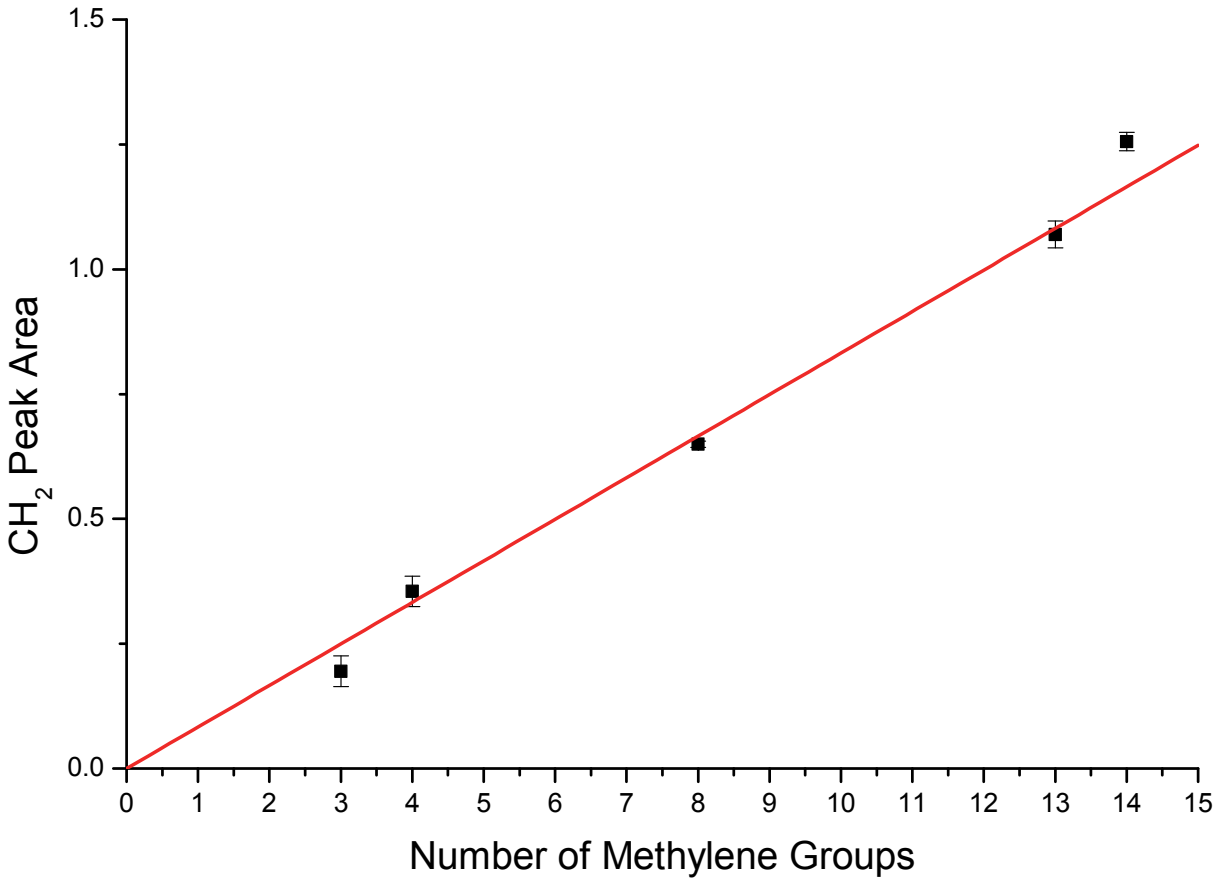

Figure 2.6: The normalized CH_2 peak area versus number of methylene groups in the linear hydrocarbon, together with a least-squares fit to a straight line with no intercept.

the pyrene ring-breathing mode and CH_2-twisting mode of the C_{18} chains were fit to Gaussian functions to determine the peak areas. The ratio of the areas of the pyrene peak and the C_{18} peak were then multiplied by the factor F (above) to determine the mole ratio of pyrene to C_{18} on the particle surface

$$\frac{mol_{pyrene}}{mol_{C18}} = \left(\frac{A_{pyrene}}{A_{C18}}\right) F \qquad \text{[Eq. 2.2]}$$

This quantitative information can be used to report the concentration of pyrene within the particle on the basis of the alkyl chain density, which is known from the elemental composition and specific surface area of the stationary phase.

2.3.3 Measurement of Intraparticle Accumulation

Isotherms

Establishing control over the partitioning equilibrium is an important goal in solid-phase extraction. For a source phase of constant solvent composition, the accumulation of analyte is expected to change linearly with the concentration of analyte in the source-phase solution. This linearity is critical for the application of an extraction step in quantifying analyte in solution. To test the range of linearity of pyrene accumulation, Raman scattering within individual C_{18} particles equilibrated in solutions with varying concentrations of pyrene as shown in Figure 2.5. Using the intensity of the CH_2-twisting mode from the C_{18} chains at 1303 cm^{-1} as an internal standard, the measured Raman scattering from pyrene can be converted to pyrene/C_{18} mole ratios for each solution concentration, as shown in Figure 2.5B. The data in Figure 2.5B are linear at low concentrations and then roll over as expected from a Langmuir isotherm

$$\Gamma = \Gamma_{max} \frac{K_L c}{(1 + K_L c)} \qquad \text{[Eq. 2.3]}$$

where the pyrene coverage, Γ, is given as a mole ratio relative to surface C_{18} chains; Γ_{max} is the maximum coverage that can be achieved; K_L is the Langmuir equilibrium constant, and c is the solution concentration. This model fits the data well (Figure 2.5B).

It was previously demonstrated that the concentration of pyrene preconcentrated onto a packed bed of C_{18}-silica stationary phase from a methanol/water solvent phase can be varied by changing the water-to-methanol volume ratio in the source phase.[9] This allows the degree of preconcentration to be controlled and used to expand the dynamic range of the method. To examine the influence of solvent composition on solid-phase extraction within single particles, a series of isotherms were measured (to the pyrene solution-phase solubility limit) of pyrene accumulation into a C_{18} particles at varying ratios of water and methanol in the source phase (Figure 2.7). These results demonstrated that the accumulation of pyrene in the C_{18}-stationary phase was significantly influenced by the volume fraction of water in the source phase. All of the isotherms in Figure 2.7 are fit to the Langmuir model (Eq. 2.3) where the maximum pyrene coverage (determined globally) is $\Gamma_{max} = 0.29 \pm 0.05$, as the mol ratio of pyrene to C_{18}-chains. This result shows that, within a Langmuir model, a sorption "site" on the hydrocarbon with sufficient volume to retain pyrene consists of ~3 C_{18} chains. This result provides some insight into the stationary phase structure needed for retention of a target compound. It should be noted, however, that the value of Γ_{max} estimated from the global fit may be driven upward by the 90% and 95% water isotherms where little roll-over has occurred; the final data points in the the 70% and 80% water isotherms (where more significant roll-over has occurred) may indicate a lower Γ_{max}. The resulting values of K_L are plotted on a logarithmic scale versus volume fraction of water in Figure 2.8. The fraction of water in the source phase has a strong effect on the

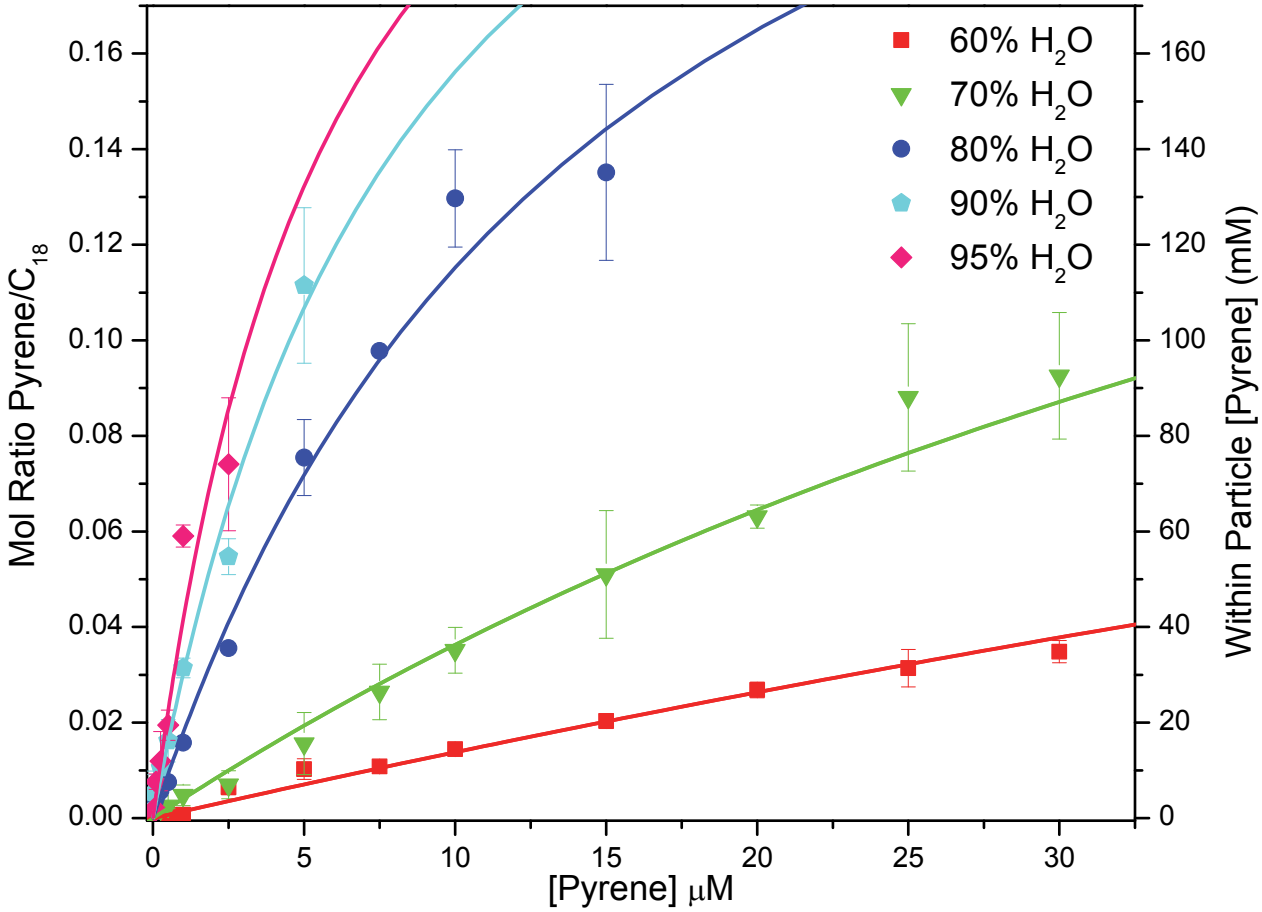

Figure 2.7. Raman spectroscopic isotherms for a series of water/methanol solutions. Isotherm measurements were carried out to the pyrene solution-phase solubility limit. The mole ratio of pyrene to C_{18} chains is plotted on the left axis, and the within-particle pyrene concentration is plotted on the right.

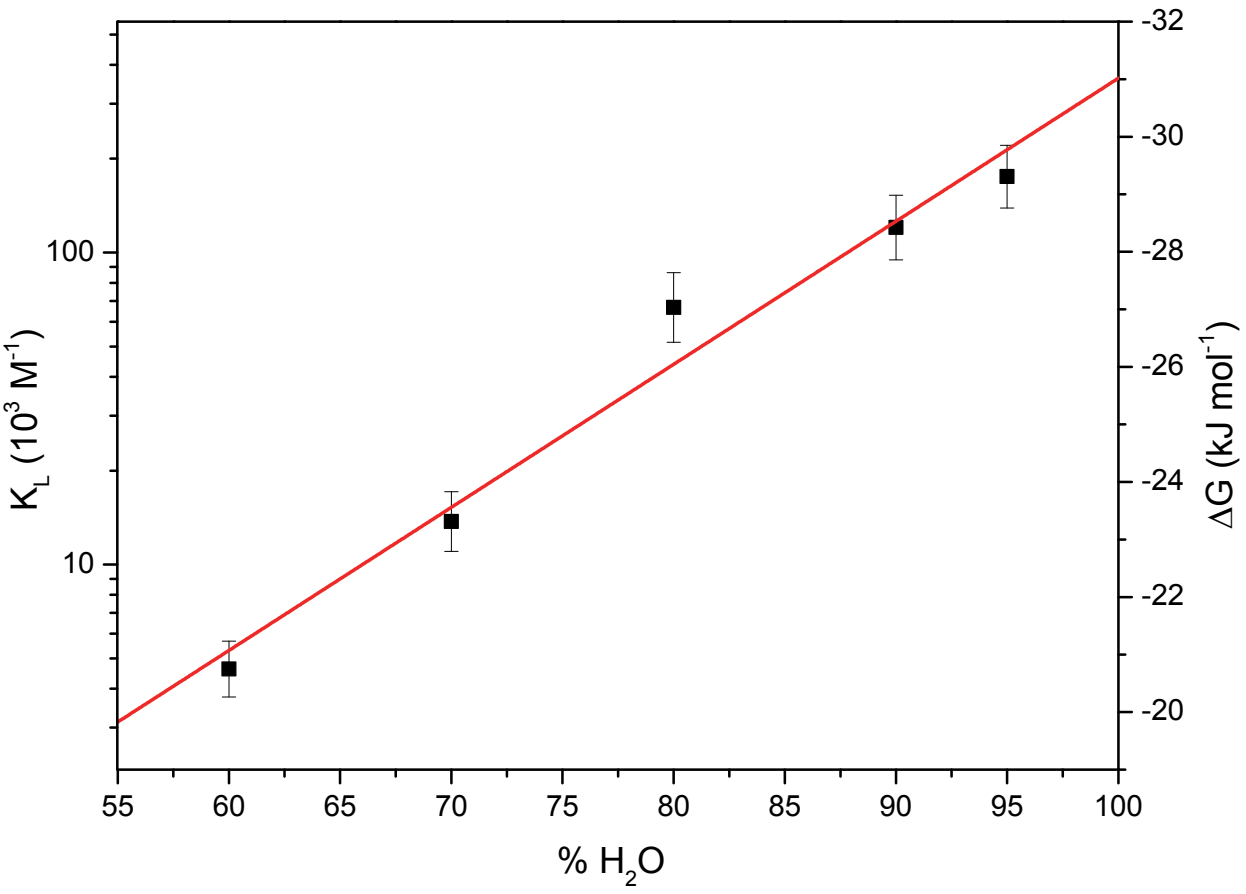

Figure 2.8. Langmuir constant, K_L, for the sorption of pyrene into C_{18} chains versus the volume fraction of water in a methanol/water source phase. The right-hand axis is the corresponding free energy of sorption from solution, with more negative values at the top.

sorption equilibrium constant, where a 30-fold increase in K_L is observed when the water fraction is increased from 60 to 95%.

The changes in the equilibrium constant can be related to the standard-state free energy change for transfer of a solute from solution to the stationary phase (ΔG^o),[20]

$$\Delta G^o = -RT \ln K_L \qquad \text{[Eq. 2.4]}$$

where a Langmuir definition of the standard state of an adsorbate[18] is half coverage, $\theta = \Gamma/\Gamma_{max} = 0.5$. Using Eq. 2.4 and the fitted values of K_L, ΔG^o for pyrene sorption to the C_{18} surface at each volume fraction of water can be determined. The variation of ΔG^o with volume fraction of water (Figure 2.8) shows a linear free energy relationship that suggests a hydrophobic driving force for sorption.[21,22] The lowering of the free energy by transferring the polycyclic aromatic hydrocarbon out of the aqueous solution and into the alkyl chains on the silica surface is driven by the PAH disrupting the hydrogen-bonding network of water in the aqueous source phase.[22] This disruption increases linearly with the probability of the solute encountering water-rich domains, which in turn varies linearly with the volume fraction of water in the source phase.[21] For applications of this technology to preconcentration and within-particle solute detection, thermodynamic control over the sorption equilibrium extends the dynamic range of the methodology, where higher-concentration samples that would saturate the surface (Figure 2.7) could be analyzed within a linear-response range by lowering the volume fraction of water in the source phase through the addition of methanol or other organic modifier.

2.3.4 Preconcentration Factors, Detection Limits, and Source Volume Requirements

Solid-phase extraction should preconcentrate an analyte from a significant volume of source phase into a much smaller volume, so that the concentration in the receiver phase is much greater than the source phase. To examine the above preconcentration equilibrium results in a way that reflects the concentration within the C_{18}-silica particle, pyrene surface coverages can be converted to within-particle pyrene concentrations. These can be determined from the mole ratio of pyrene to C_{18} chains, determined above, and used to report the preconcentration factors for pyrene within the particle. This is accomplished by determining the mass of a single particle from its volume and density (solvent displacement) and using the surface area (nitrogen BET) and C_{18} surface coverage (by the percentage of carbon from microanalysis) to determine the molarity of C_{18} chains (0.93M) in the particle. The mol ratio of pyrene to C_{18} chains determined above is then multiplied by the molarity of C_{18} chains within the particle to give the molar concentration of pyrene within a particle. The results of this conversion are plotted on the right-hand y axis in Figures 2.5B and 2.7. Preconcentration factors based on these results ranged from 1.4 (± 0.3) × 10^3 from a low-water fraction (60%) source phase to a maximum of 4.8 (± 0.8) × 10^4 from 95% water. The extraction factor from high-water conditions provides a significant improvement in detection capability for PAH compounds by Raman scattering. Based on the blank reproducibility and the preconcentration factor at the highest water conditions, we estimate the limit of detection (at 95% confidence[23]) for pyrene to be 10 nM in the source phase, which produces a 4.8 mM concentration within the particle. This prediction was tested, and pyrene detection of pyrene from a 10 nM source phase is

demonstrated in Figure 2.9.

Although large extraction factors can lead to significantly lower detection limits as shown above, the source-phase volumes required to achieve such a high preconcentration factor represent a major kinetic challenge to reach equilibrium. For example, for extraction into a ~10-μL collector phase as previously employed for *in-situ* Raman detection,[9-11] the source-phase volume required to reach a 48,000 preconcentration factor would be 480 mL. While this volume of sample solution might be available, the real measurement challenge arises from the kinetic limitations of molecular transport needed to bring analyte molecules from a large sample volume into equilibrium with a small collection volume. The most efficient means of addressing the transport problem is to flow the sample solution past the collector phase. However, flow rates must be sufficiently slow to allow incremental volumes of the sample solution to equilibrate during their contact with the collector. Even if equilibrium can be reached with each 10-μL incremental volume of source phase within 1 s (this would require diffusion distances less than 20 μm), the time required to equilibrate the receiver phase with the entire 480-mL sample volume would exceed 13 h. To overcome this problem, a single-particle receiver phase provides a significant (~10^{-7}-fold) reduction in the source-phase volume required to supply the molecules needed to achieve large preconcentration factors compared to previous *in-situ* Raman spectroscopy measurements. The single 10-μm-diameter spherical particle used in this work has a particle volume of only 520 fL. For a preconcentration factor of 4.8×10^4, the analyte solution volume needed to supply the needed pyrene to reach equilibrium was only 25 nL, and the time required for the particle interior to reach an equilibrium concentration of pyrene was less than 2 min. The source-phase volume required to reach equilibrium is proportional to the collector-

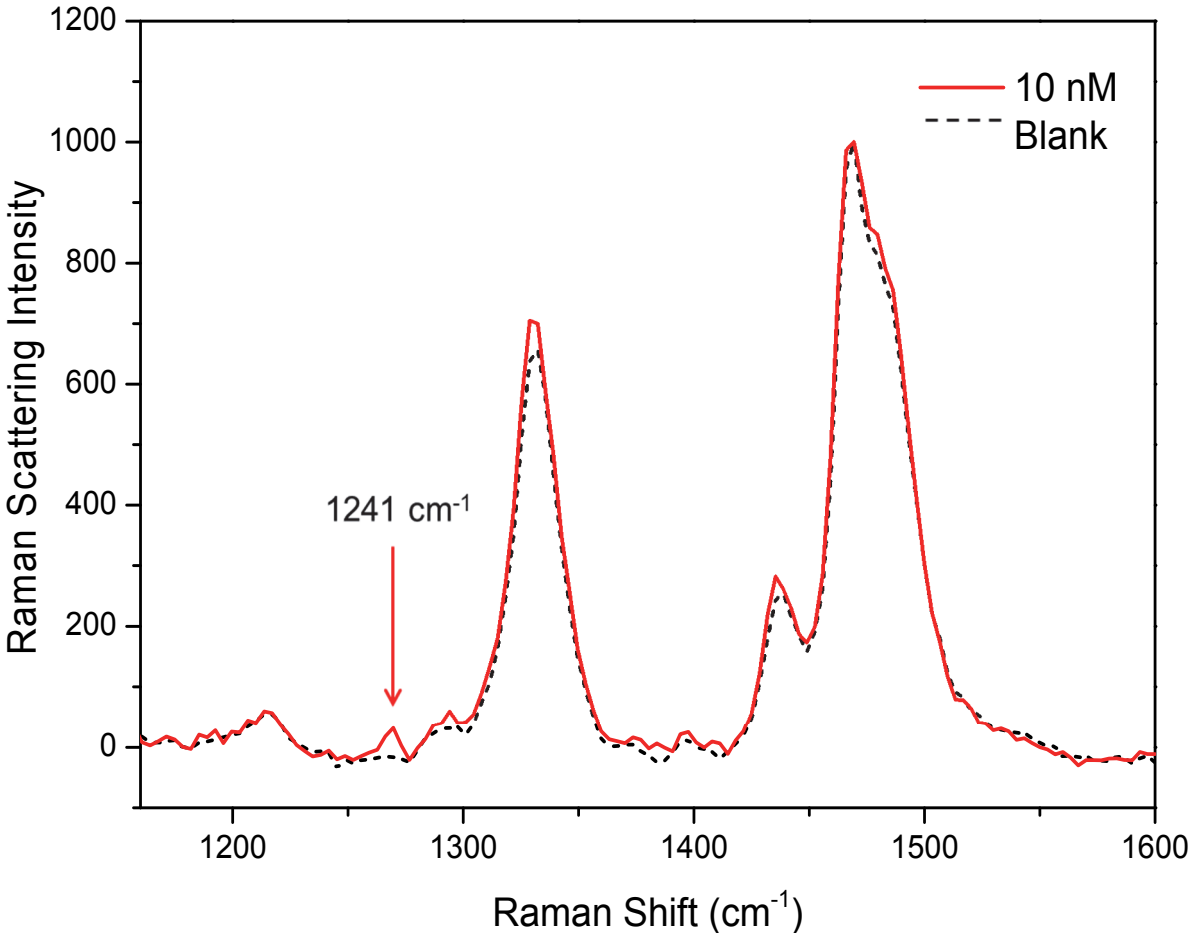

Figure 2.9. Detection of pyrene within a C_{18} particle preconcentrated from a 10-nm solution (240-s integration).

phase volume, which varies as the cube of the particle diameter. Thus, a 300-fold reduction in the solution volume requirements could easily be achieved with commercially available 1.5-μm-diameter C_{18} chromatographic particles, where *no loss of detection sensitivity* would be expected because the entire confocal probe volume would still reside within a particle of this size.

2.4 Conclusions

In this work, *in-situ* detection of the solid-phase extraction of pyrene into single C_{18}-silica particles is demonstrated using confocal Raman microscopy, which avoids analyte dilution due to a wash-off step. Raman scattering from the C_{18}-chains on the interior surface of the porous particle serve as an internal standard for quantitative determination of surface coverage of pyrene and the corresponding within-particle pyrene concentration. This methodology was used to measure isotherms for transfer of pyrene into the C_{18} stationary phase from solutions of different water/methanol composition, demonstrating a convenient means of controlling the preconcentration equilibrium which expands the dynamic range of the detection method. At the highest volume fraction of water in the source-phase solution (95%), the ratio of the within-particle to solution concentration for pyrene was 4.8×10^4, and detection limit of 10-nM pyrene from the source-phase was demonstrated.

2.5 References

(1) Pawliszyn, J. *Solid Phase Microextraction Theory and Practice*; Wiley-VCH: New York, 1997.

(2) *Solid-Phase Extraction Principles, Techniques, and Applications*; Simpson, N. J.

K., Ed.; Marcel Dekker, Inc.: New York, 2000.

(3) Fritz, J. S. *Analytical Solid-Phase Extraction*; John Wiley & Sons, Inc.: New York, 1999.

(4) Nge, P. N.; Pagaduan, J. V.; Yu, M.; Woolley, A. T. *J. Chromatogr. A* **2012**, *1261*, 129.

(5) Kutter, J. P.; Jacobson, S. C.; Ramsey, J. M. *J. Microcolumn Sep.* **2000**, *12*, 93.

(6) He, B.; Tait, N.; Regnier, F. *Anal. Chem.* **1998**, *70*, 3790.

(7) Kawaguchi, T.; Shankaran, D. R.; Kim, S. J.; Matsumoto, K.; Toko, K.; Miura, N. *Sens. Actuators B* **2008**, *133*, 467.

(8) Tian, H.; Huhmer, A. F. R.; Landers, J. P. *Anal. Biochem.* **2000**, *283*, 175.

(9) Carr, J. W.; Harris, J. M. *Anal. Chem.* **1988**, *60*, 698.

(10) Wittkamp, B. L.; Tilotta, D. C. *Anal. Chem.* **1995**, *67*, 600.

(11) Nwaneshiudu, I. C.; Yu, Q.; Schwartz, D. T. *Appl. Spectrosc.* **2012**, *66*, 1487.

(12) Cherney, D. P.; Harris, J. M. *Annu. Rev. Anal. Chem.* **2010**, *3*, 277.

(13) Houlne, M. P.; Sjostrom, C. M.; Uibel, R. H.; Kleimeyer, J. A.; Harris, J. M. *Anal. Chem.* **2002**, *74*, 4311.

(14) Gasser-Ramirez, J. L.; Harris, J. M. *Anal. Chem.* **2009**, *81*, 2869.

(15) Gasser-Ramirez, J. L.; Harris, J. M. *Anal. Chem.* **2009**, *81*, 7632.

(16) Gasser-Ramirez, J. L.; Harris, J. M. *Anal. Chem.* **2010**, *82*, 5743.

(17) Bridges, T. E.; Houlne, M. P.; Harris, J. M. *Anal. Chem.* **2003**, *76*, 576.

(18) Williams, K. P. J.; Pitt, G. D.; Batchelder, D. N.; Kip, B. J. *Appl. Spectrosc.***1994**, *48*, 232.

(19) Lin-Vien, D.; Cothrup, N.B.; Fateley, W. G.; Grasselli, J. G. *The Handbook of Infrared and Raman Characteristic Frequencies of Organic Molecules*; Academic Press: San Diego, CA, 1991.

(20) Vailaya, A.; Horváth, C. *Ind. Eng. Chem. Res.* **1996**, *35*, 2964.

(21) Horváth, C.; Melander, W.; Molnár, I. *J. of Chromatogr. A* **1976**, *125*, 129.

(22) Tanford, C. *The Hydrophobic Effect: Formation of Micelles and Biological Membranes, 2nd ed.*; Wiley: New York, 1980.

(23) Currie, L. A. *Anal. Chem.* **1968**, *40*, 586.

CHAPTER 3

CONFOCAL RAMAN MICROSCOPY FOR IN-SITU DETECTION OF OCTANOL-WATER PARTITIONING WITHIN THE PORES OF A SINGLE CHROMATOGRAPHIC SILICA PARTICLE

3.1 Introduction

The octanol-water partition coefficient (K_{ow}), defined as the ratio of the concentration of a molecule in an octanol-phase to its concentration in an aqueous-phase in a two part octanol-water extraction,[1] is a widely used predictor of lipophilicity. K_{ow} is commonly used to predict potential pharmacological activity[2] or toxicity[3] of a compound in medicinal chemistry research, as well as fate, transport, and ecotoxicity of a compound in the environment.[4] There are numerous methods available for determining K_{ow}; however, the most common conventional techniques are slow-stirring[5] and shake-flask[6] methods. Here an analyte is allowed to equilibrate across the boundary between octanol and water phases, where the sample is stirred or shaken to increase the rate of transport between the two phases. Each phase is then analyzed to determine K_{ow}. While these methods are simple,

---

Reprinted (adapted) with permission from: Kitt, J.P.; Harris J.M.; Confocal Raman Microscopy for in Situ Measurement of Octanol–Water Partitioning within the Pores of Individual C18-Functionalized Chromatographic Particles, *Analytical Chemistry*, **2015**, 87 (10), 5340-5347, DOI: 10.1021/acs.analchem.5b00634.

they require large (milliliter) quantities of analyte solution and are slow, often requiring hours to reach equilibrium. For screening new drug candidates, the large sample quantities needed for this measurement are costly to produce and screening of many structures is time consuming.

To address the need for a rapid, small volume method of determining octanol-water partition coefficients, recent research has adapted microfluidic sample handling to the measurement of K_{ow}. Experiments are generally of two types, slug flow[7-9] or side-by-side flow[10]. In slug flow, droplets of octanol and aqueous solution are transported in contact with one another through a microfluidic channel. Equilibration between aqueous and octanol phases occurs quickly due to a high surface-area-to-volume ratio and constant mixing of the interface as the droplets flow through the channel.[9] Side-by-side flow experiments maintain a parallel flow profile between water and octanol in a microfluidic channel with analyte equilibration occurring as the two-phases traverse the channel. These experiments have lowered the octanol-volume requirements to the nanoliter scale and allow determination of K_{ow} in minutes. Further reduction in octanol-water partition volumes has been challenged by detection and fluid manipulation in small volumes. In side-by-side flow channels, equilibrium occurs at a distance down the channel where the two-phases have remained in contact for a sufficient time for diffusion and partitioning to equilibrate the analyte concentrations in the two phases. The analyte concentrations in each of the phases as well as the distance to reach equilibrium have been determined using fluorescence measurements.[10] To expand the scope of measurements beyond fluorescent compounds, slug-flow studies have been carried out with UV-vis absorption detection.[7,9] UV-vis monitoring limits further miniaturization, however, due to the path length requirements for

sensitive detection, necessitating sample volumes of hundreds of nanoliters or more.[7]

Another approach to measuring octanol-water partitioning is through the use of reversed-phase liquid chromatography.[1,11,12] This method allows smaller source-phase sample volumes (typically microliter) and experiments generally require less than an hour. In this case, however, K_{ow} is inferred from retention data by comparison to the behavior of similar compounds, where K_{ow} has been measured by traditional extraction methods.[1,11] This empirical determination of K_{ow} is not always straightforward, however; chromatographic retention depends on competing interactions between an analyte and the stationary phase and mobile phase.[12,13] This interpretation is further complicated for charged molecules where retention of the analyte at the interface between the stationary- and mobile-phases is driven by a lowering of the surface tension between the two phases,[14] which is not present in bulk octanol-water partitioning. In addition, small differences in structure of solutes, such as planarity,[15] in otherwise similar molecules can result in drastic changes in the affinity of a molecule for a bonded stationary-phase, which can further complicate the prediction of octanol-water partitioning from chromatographic retention data.[1,12]

Chromatographic support materials can be used to measure octanol-water partitioning, while avoiding interfacial interactions governing reversed-phase retention, through the use of a generator column.[16-18] Here, a packed chromatography column is filled with octanol containing the dissolved analyte. The bulk octanol between the particles is then displaced by flowing water through the column while intraparticle octanol remains confined within the pores of the particles. Octanol-saturated water is then flowed at a sufficiently slow rate to allow equilibration with analyte in the intraparticle octanol phase,

and the analyte that elutes is collected by solid-phase extraction. The analyte that was washed from octanol column is then quantified *ex-situ* (usually by gas chromatography (GC) or high-pressure liquid chromatography (HPLC)) and used to determine K_{ow}. The generator column method is procedurally similar to HPLC or GC (carrying out a measurement is simple) while advantageously measuring K_{ow} directly. However, generator columns are similarly challenged by large sample requirements and long measurement times. Measuring K_{ow} of charged compounds also remains a challenge due to limited solubility in octanol leading to depletion of the analyte from the generator column.

In the present work, we employ the concept developed in generator column measurements to measure partitioning of an analyte into an octanol phase confined in the pores of *individual* C_{18}-chromatographic silica particles. The overwhelming challenge of displacing and manipulating the 100-fL volume of octanol trapped in a single particle is avoided by determining the concentration of octanol-partitioned analyte *inside the particle* using confocal Raman microscopy. This approach reduces the volume of the octanol receiver phase by more than a factor of 10^6 compared to microfluidic techniques, and decreases the amount of analyte required to make an octanol-water partition measurement to less than 3 pmol. Confocal Raman microscopy has been previously utilized to probe the interior chemistry of chromatographic silica particles, including studies of the functionalization of the silica surface,[19] the interfacial solvation environment of C_{18}-stationary phases,[20,21] the mechanism of surfactant-mediated ion-pair retention,[22] and femtoliter-scale solid-phase extraction of PAH compounds.[23] In the present work, within-particle confocal Raman microscopy is extended to liquid-liquid (octanol-water) partitioning. Collection of Raman scattering from analytes within octanol-filled pores of

C_{18} silica particles is demonstrated, where quantitative determination of the octanol-water partition coefficient is achieved by using the Raman scattering signal from the n-octanol and surface-bound C_{18} alkyl chains as an internal standard. The method is tested for measurements of the pH-dependent octoanol-water partitioning of naphthoic acid, and results are compared to traditional shake-flask measurements and to sorption onto C_{18}-modified silica without octanol present within the pores.

3.2 Experimental Section

3.2.1 Reagents and Materials

Spherical chromatographic silica particles were obtained from YMC America (YMC-Pack ODS-A, Allentown, PA). The particles were monofunctional, C_{18} derivitized and end-capped with trimethychlorosilane. The particle specific surface area was 93 m^2/g. Particles had a mean diameter of 10 μm, a pore diameter of 319 Å, and pore volume of 0.80 mL/g as reported by YMC America. Carbon content (6.9%) and specific surface area were reported by YMC America and used to determine the C_{18} surface coverage of 3.4 $\mu mol/m^2$. The density of the silica skeletal structure (1.85 ± 0.02 g/cm^3) used for pore volume calculation was determined by methanol displacement of a known mass of silica particles. The volume occupied by the C_{18} phase of 0.17 mL/g was determined by measuring methanol-water displacement before and after removing the C_{18}-phase by oxidation in a muffle furnace at 800°C. This value was also used to determine the pore volume of the bare silica, 0.97 mL/g.

Octanol (Reagent, 99%) was obtained from MP Biomedicals, LLC (Solon, OH). Methanol (Photrex, ≥99.8%) and hydrochloric acid (Macron, 36.5-38%) were obtained

from Avantor (Center Valley, PA). 1-Naphthoic acid (Aldrich, 96%) and sodium hydroxide (Aldrich, ≥98%) were obtained from Sigma Aldrich (St. Louis, MO). Water used for this experiment was filtered using a Barnstead GenPure UV filtration system (ThermoFisher Scientific, Waltham, MA) and had a minimum resistivity of 18.0 MΩ·cm.

A microfluidic flow cell was constructed for *in-situ* Raman microscopy. A diagram of the cell has been published previously;[23] briefly, two 4-mm diameter holes were drilled 11 mm apart in a 5-mm thick, Pyrex glass cover plate (VWR, Radnor, PA) to which two 2.4 mm i.d. Luer adapters (Value Plastics, Inc., Fort Collins, CO) were connected with Devcon 5-min epoxy (ITW Devcon, Danvers, MA). A glass coverslip (Gold Seal, Erie Scientific Co., Portsmouth, NH) was attached to the coverplate using 3M, 140-µm thick double sided tape (TapeCase Ltd., Elk Grove Village, IL), where a 2.5 mm wide × 11 mm long channel was cut between the holes in the cover plate creating a 3.9 µL flow channel. Tubing used in flow experiments was 1.6 mm o.d. × 2.4 mm i.d. Viton elastomer (Cole-Parmer, Vernon Hills, IL). A microscopy well cell was constructed for measuring naphthoic acid/octanol standards in solution. The cell consisted of a 12 mm length of 10 mm i.d. glass tubing fixed to a glass coverslip (Gold Seal, Erie Scientific Co., Portsmouth, NH) using 5-min epoxy (ITW Devcon, Danvers, MA).

3.2.2 Confocal Raman Microscopy

A detailed description of the confocal Raman microscope used in this work has been described previously.[24] Briefly, a 638-nm diode laser beam (Innovative Photonic Solutions No. 10638SH0035B-TH-L) is directed into a spatial filter (Thorlabs, KT310) where the beam is focused through a 5-µm pinhole and then collimated using a pair of

antireflective, aspheric lenses (Thorlabs, C560TME-A). The collimated beam is then passed into a filter cube carrying an excitation filter (Semrock, FF01-640/14) and dichroic beam-splitter (Semrock, Di02-R635) which reflects the beam into a 100X, 1.4 N.A. oil immersion objective (Nikon, Plan APO VC) mounted on an inverted fluorescence microscope frame (Nikon Eclipse TE-200), slightly overfilling the back aperture. Scattered light is collected using the same objective and passed back through the dichroic beam-splitter. The light leaving the microscope is collected and collimated before passing through a final, high-pass filter (Semrock, BLP01-635R). The filtered, Raman scattered light is then focused onto the entrance slit of a Chromex 250IS spectrograph which is set to 50 μm, defining the confocal aperture in the horizontal-dimension.[25] Spectra are dispersed using a diffraction grating with 600 lines/mm blazed at 750-nm and collected on a charge couple device (CCD) detector (Andor, iDus DU401A) where the vertical dimension of the confocal aperture is defined by limiting acquisition to 3-pixel rows (78 μm).[25]

To collect Raman scattering from the interior pores of single chromatographic particles, the laser beam was brought to focus at the coverslip-solution interface where a visible reflection of the focused spot is produced. The microscope stage was translated in the *x* and *y* dimensions, until the focused spot was positioned directly below the center of an isolated particle on the coverslip surface. The microscope objective was then translated upward 5 μm in the *z* dimension, centering the confocal volume inside the particle. Raman spectra were collected using 60-s acquisitions. Raman spectra of the octanol-naphthoic acid standards were collected from ~0.5 mL aliquots in a microscopy well cell. The laser was brought to focus at the coverslip-solution interface and then translated 5-μm into solution.

A spectrum was acquired with 60-s exposure time from each of three standards. The ratio of the areas of the naphthoic acid ring-breathing mode and the octanol CH_2-twisting mode were averaged for the three samples to provide relative intensities for quantitative analysis. All spectra were baseline corrected using a custom Matlab (Mathworks, Natik, MA) program which fits the baseline portions of the spectrum to a seventh-order polynomial. Following correction, Raman scattering bands were fit with Gaussian shapes to determine peak areas.

3.2.3 Sample Preparation and Characterization

Naphthoic acid samples were prepared in 0.5 mM citrate buffer adjusted to final pH by addition of small amounts of sodium hydroxide or hydrochloric acid. Mutually saturated solvents were used in all experiments to avoid changes in solvent composition. For measuring octanol-water partitioning, the pores of C_{18}-chromatographic particles were filled with octanol by dispersing particles into octanol; the dispersion was centrifuged to collect particles, the supernatant removed, and particles suspended in octanol saturated water by sonicating for a short (~10 s) time. Octanol-filled particles in water were injected into a microfluidic flow cell and allowed to settle and adhere to the glass surface for ~2 h. A syringe pump (Harvard Pump 11 Plus, Harvard Apparatus, Holliston, MA) was used to flow octanol-saturated water into the flow cell at a rate of 0.5 mL/min for ~5 min while monitoring the flow cell using bright-field microscopy to confirm particles adhered to the surface. Following identification of stationary particles, naphthoic acid samples were introduced at a flow rate of 0.5 mL/min to supply a constant concentration of naphthoic acid to the particle. The CH_2-twisting mode at 1303 cm^{-1} from C_{18} and octanol n-alkyl

chains as well as the octanol C-O stretch at 963 cm^{-1} were monitored throughout the experiment to ensure constant presence of octanol in the pores. Accumulation of naphthoic acid was monitored by measuring the increase in Raman scattering from the naphthoic acid ring-breathing mode at 1382 cm^{-1} using sequential 15 s acquisitions; equilibrium was confirmed when Raman scattering remained constant across subsequent acquisitions. At this point, Raman spectra were collected from the interior of three different particles for quantitative analysis.

For measurements of partitioning onto the C_{18} surface, C_{18}-silica particles were first wetted by dispersing in methanol. Methanol/particle solution was injected into a flow cell and particles were allowed to settle before the cell was placed in a 120℃ oven for 5 min allowing methanol to evaporate which causes the particles to adhere to the glass surface. Particles were rewetted with methanol and rinsed with water prior to introduction of a naphthoic acid sample into the cell. A syringe pump (Harvard Pump 11 Plus, Harvard Apparatus, Holliston, MA) was then used to flow water into the cell at a rate of 0.5 mL/min while monitoring Raman scattering from the particle interior until no methanol Raman bands were observed in the spectrum. At this point, a naphthoic acid sample was introduced. Accumulation of naphthoic acid was monitored by measuring the increase in Raman scattering from the naphthoic acid ring-breathing mode at 1382 cm^{-1} using consecutive 15 s acquisitions, where equilibrium was confirmed when the Raman scattering intensity was no longer changing. Raman spectra for quantitative analysis were then collected from the interior of three different particles.

In order to compare the results to traditional measurements of octanol-water partitioning, the distribution of naphthoic acid between bulk octanol and water phases was

determined using a traditional shake-flask approach.[6] Stock solutions of 50 mM and 5 mM naphthoic acid were prepared in water-saturated octanol for pH 2.0 and pH 6.0 measurements, respectively. Aliquots (1 mL) of the stock solution were transferred to scintillation vials and 19 mL of octanol-saturated 10 mM citrate buffer at pH 2 or pH 6 were added. Vials were shaken until turbid and mixed overnight (~15 h) to ensure equilibrium concentrations of naphthoic acid in each phase. Equilibrated samples were centrifuged to separate phases and the absorbance of the water phase measured. UV-vis spectra of naphthoic acid standards were measured using a Hitachi U-3310 spectrophotometer at pH 2 and pH 6 to determine the naphthoic acid absorption maxima and a calibration curve was prepared at each pH (Figure 3.1). Naphthoic acid concentrations in the aqueous phases were determined by comparing the measured absorbances to the calibration curves; the concentration in the octanol phase was determined by the difference.

3.3 Results and Discussion

3.3.1 Confining Octanol within the Pores of C_{18} Functionalized Silica Particles

In this work, the goal is to measure the partitioning of analytes from aqueous solution into an octanol phase that is confined within the porous network of a chromatographic silica particle. To this end, maintaining the octanol within the pores of the particle is essential to the measurement. Octanol confinement within *bare silica* particles has been demonstrated previously in generator-column experiments; however, longer-term exposure of the octanol to an aqueous mobile phase caused octanol to leach

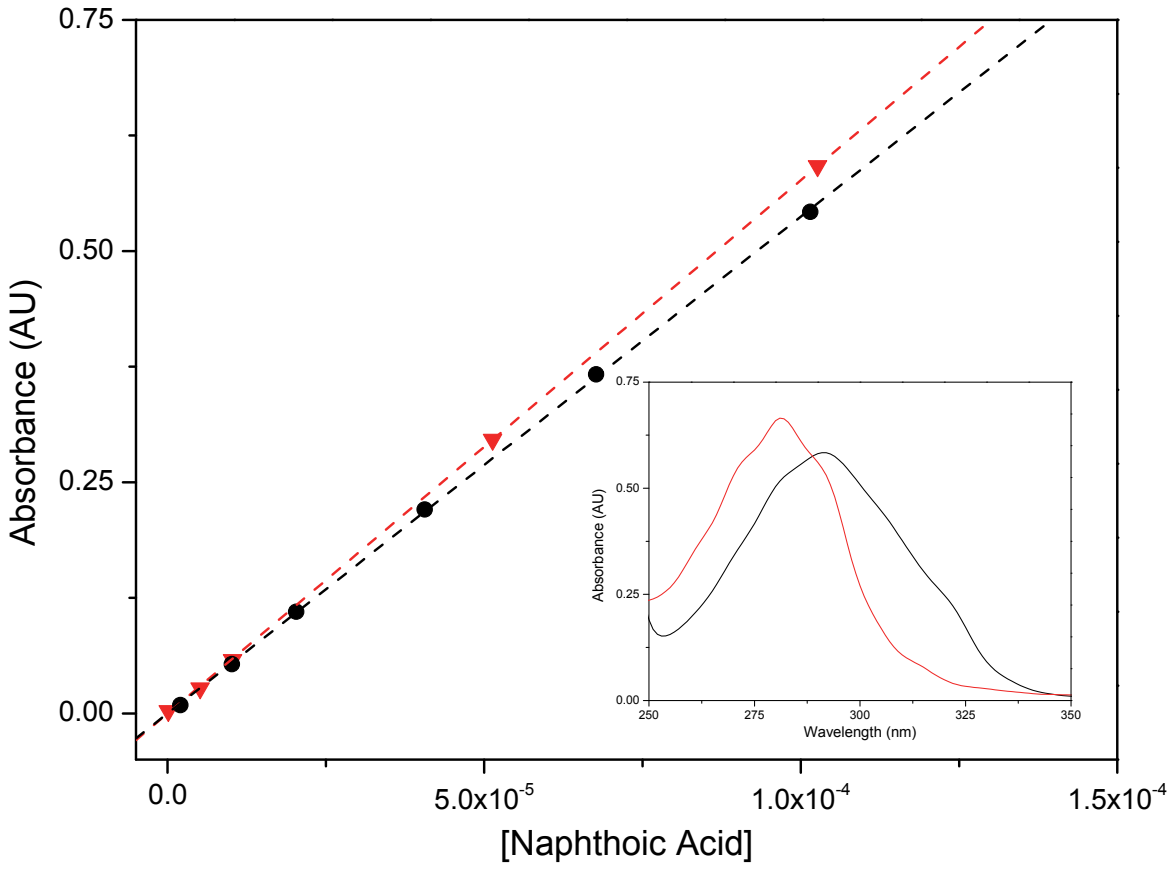

Figure 3.1. UV-vis calibration curves for protonated (black) and deprotonated (red) naphthoic acid in citrate buffer (pH 2.0 and pH 6.0, respectively). Inset: UV-Vis absorbance spectra of protonated (black) and deprotonated (red) naphthoic acid. Extinction coefficients are 5,371±9 $M \cdot cm^{-1}$ and 5,770±10 $M \cdot cm^{-1}$ for protonated and deprotonated forms at absorbance maxima of λ=291 nm and λ=281 nm, respectively.

out of the particles.[17,26] To address this issue, the pores of bare silica particles were filled with octanol, and then the flow was switched to octanol-saturated water while monitoring Raman scattering from within the particle. Within several minutes of switching the flow water, octanol leached from the particle interior despite the water being octanol-saturated. To solve this problem, hydrophobic (octadecylsilane) functionalized silica was tested for octanol confinement. Hydrophobic surfaces have been used previously to control fluid flow of "wetting" versus "nonwetting" solvents in microfluidic circuits[9,27] and has specifically been used to separate octanol from water in 50-μm channels.[9] A larger (32-nm diameter) pore, C_{18}-functionalized silica was chosen so that the octanol-filled pore volume would dominate the solvation environment. When these particles were exposed to octanol and the solution switched to octanol-saturated water, octanol was retained indefinitely within the pores.

To demonstrate this result, a Raman spectrum from the interior of a C_{18}-silica particle in contact with water is compared with an octanol-filled particle after exposure to octanol-saturated water (Figure 3.2). Upon filling with octanol, the C-C stretching modes at 1064 cm^{-1} and 1077 cm^{-1}, the CH_2-twisting mode at 1303 cm^{-1}, and the C-H bending mode at 1438 cm^{-1} and C-H stretching modes in the 2800 cm^{-1} to 3000 cm^{-1} region all increase relative to the empty particle, due to the incorporation of the C_8 acyl chain from octanol. In addition, the octanol C-O stretch at 963 cm^{-1} appears, further indicating that the pores have been filled with octanol. Retention of octanol is confirmed by the Raman scattering from octanol remaining constant as experiments are conducted over hours.

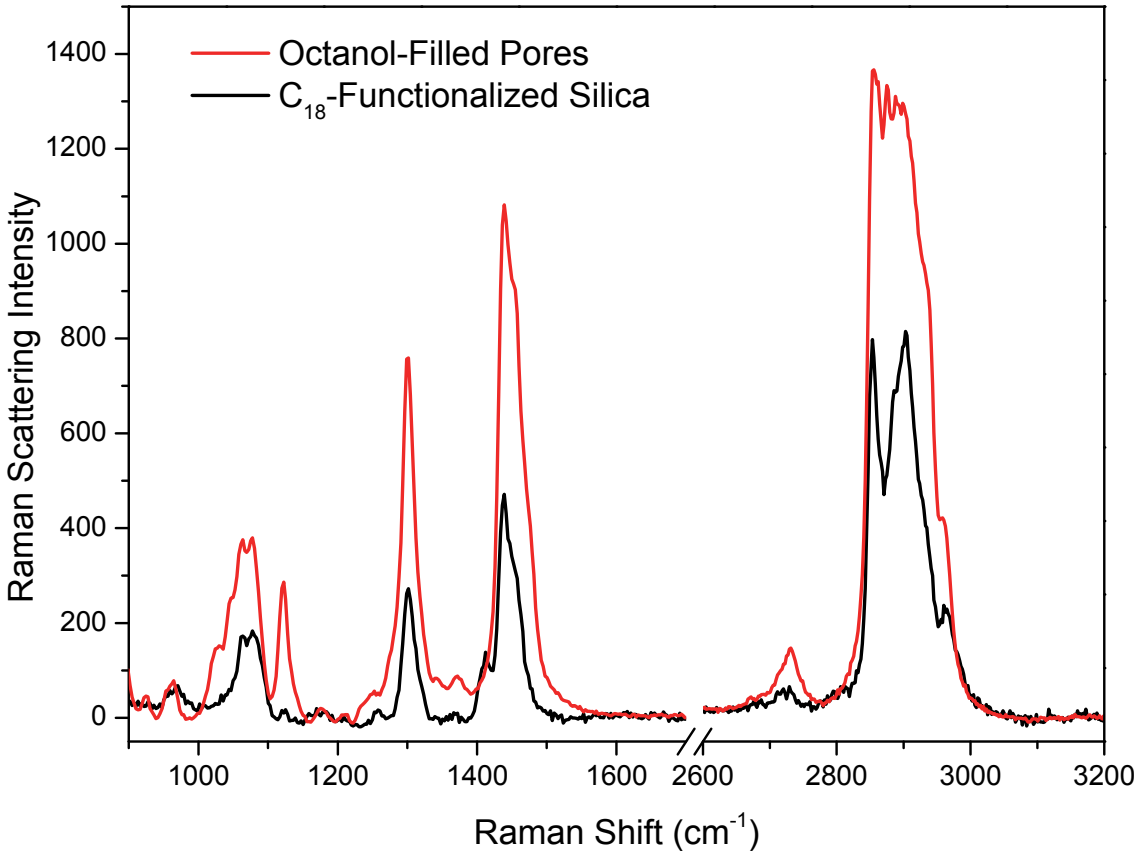

Figure 3.2. Raman spectra from the interior of a single C_{18} particle before (black) and after (red) filling with octanol.

3.3.2 Quantitative Measurement of Octanol-water Partitioning from within Octanol Filled C_{18} Silica

The octanol-water partition coefficient is defined as the ratio of the concentration of a molecule, *M*, dissolved in octanol relative to its concentration in water in a two-phase partition equilibrium:

$$K_{ow} = \frac{[M_{oct}]}{[M_{H_2O}]} \qquad \text{[Eq 3.1]}$$

Because the magnitude of K_{ow} varies widely from one molecular structure to another, this partition coefficient is often expressed logarithmically as log K_{ow}. As an example compound to test the proposed methodology, the partitioning of naphthoic acid into octanol confined within the pores of a single C_{18}-derivitized chromatographic particle was measured by collecting Raman scattering from within the particle interior after equilibration; see Figure 3.3. Quantification of naphthoic acid was achieved also measuring Raman scattering from the n-alkyl chains of octanol and surface-bound C_{18} as an internal standard. It has been previously demonstrated that the area of the CH_2-twisting mode (1303 cm^{-1}) from n-alkyl chains responds linearly to the concentration of methylene groups, with a slope that is independent of chain length.[23] Thus by comparing the scattering from the naphthoic acid ring-breathing mode (1382 cm^{-1}) to scattering from the CH_2--twisting mode in a free-solution sample of known hydrocarbon concentration, it is possible to generate a response factor that allows the concentration of naphthoic acid to be quantified within the octanol-filled pores of the particle.

Calibration of the naphthoic acid response was achieved by measuring Raman scattering from naphthoic acid/octanol standards in methanol (Figure 3.4). A response factor was determined from the peak areas, *A*, of the naphthoic acid ring-breathing mode

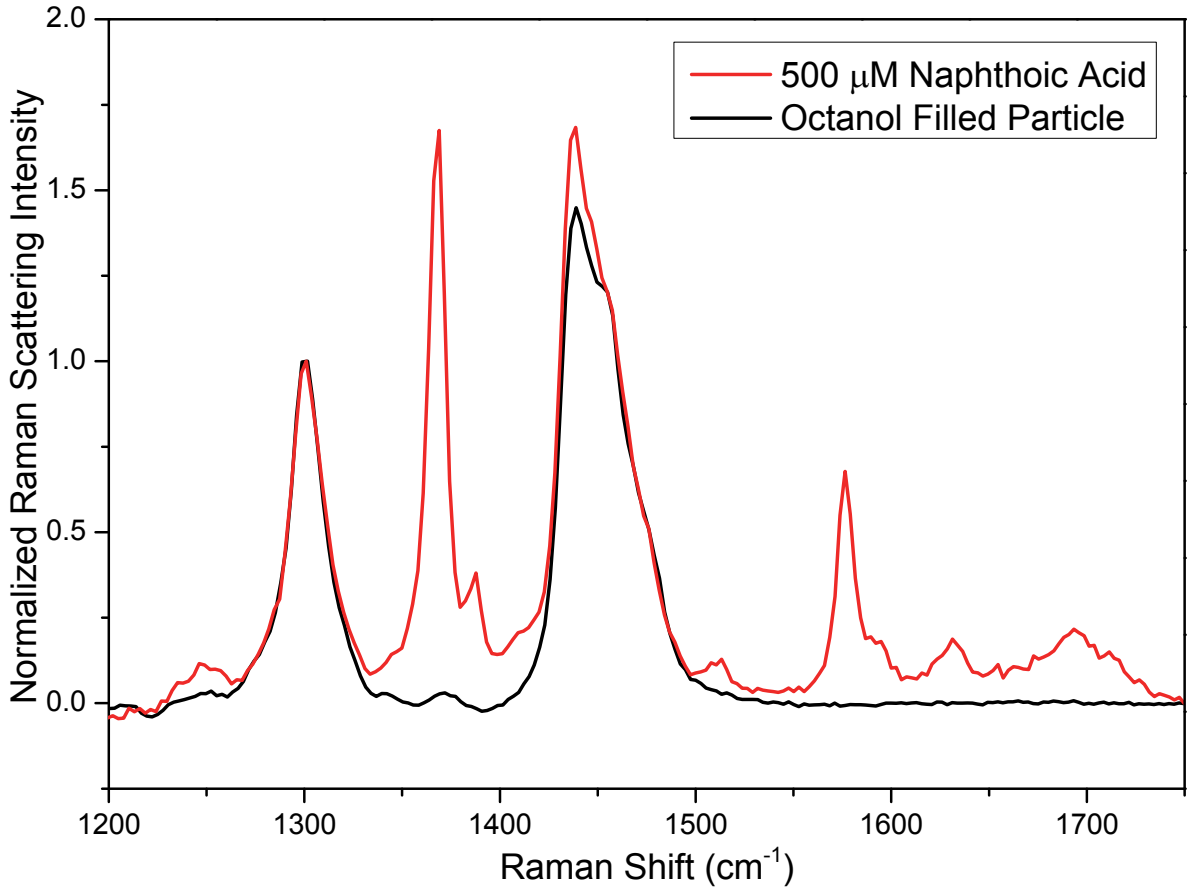

Figure 3.3. Normalized Raman spectra from the interior of a single octanol-filled chromatographic particle after equilibration with 500 μM naphthoic acid in pH 2 buffer.

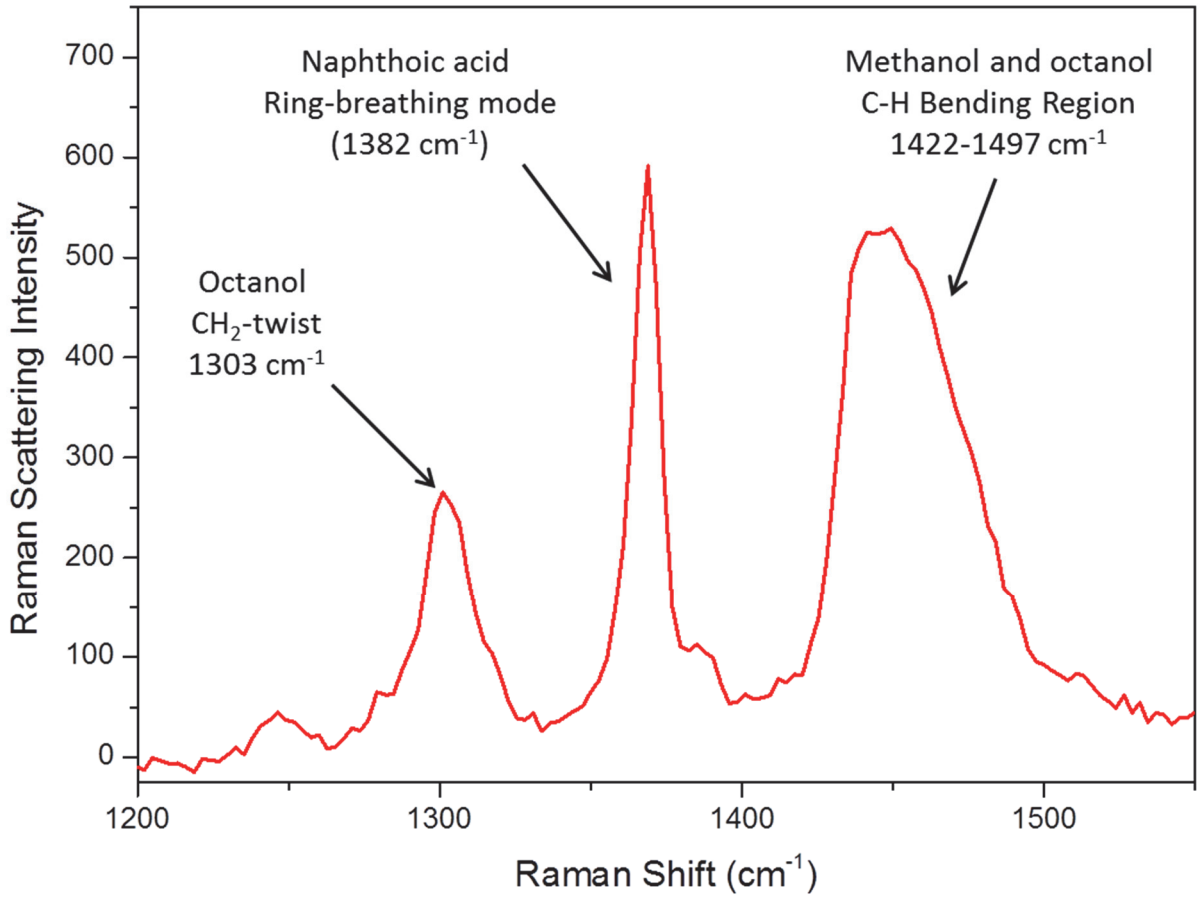

Figure 3.4. Raman spectrum of a standard solution of octanol and naphthoic acid in methanol, used to calibrate their relative scattering: 3.16 M octanol, 250 mM napthoic acid.

and of the octanol CH_2-twisting mode (Eq. 3.2), ratioed to the molar concentrations (in brackets) of naphthoic acid and octanol, and the corresponding concentration of CH_2 groups, in the solution:

$$F = \frac{A_{CH2}[Naphthoic\ Acid]}{A_{Naphthoic}([octanol]\times 7CH_2)} = \frac{A_{CH2}[Naphthoic\ Acid]}{A_{Naphthoic}[CH_2]} \quad \text{[Eq. 3.2]}$$

Determining the naphthoic acid concentration within the pores of the particle was then accomplished by multiplying the measured Raman scattering from naphthoic acid relative to the CH_2 scattering by the response factor and by concentration of CH_2 in the pores. The total concentration of CH_2 groups in the pores derives from the concentration of octanol (from the density of octanol times the pore volume of the C_{18}-derivatized silica divided by the pore volume of the bare silica, [octanol] = 5.22 M) and the concentration of C_{18} chains in the pores (from carbon analysis of the stationary phase and the pore volume of the bare silica, [C_{18}] = 0.33 M):

$$[Naphthoic\ Acid] = F\frac{A_{Naphthoic}[CH_2]}{A_{CH_2}} = F\frac{A_{Naphthoic}([octanol]\times 7_{CH_2}+[C_{18}]\times 17_{CH_2})}{A_{CH_2}} \quad \text{[Eq.3.3]}$$

Dividing the within-pore concentration of naphthoic acid in octanol by its source-phase (aqueous) concentration gives the partition coefficient. From the results in Figure 3.3, the octanol-water partition coefficient of naphthoic acid at pH 2.0 (98% protonated based on its pK_a of 3.7)[28] is K_{ow} = 840 ± 40 or log K_{ow} = 2.9 ± 0.1. The uncertainty derives from the reproducibility of measurements made in several different particles (Figure 3.5). Raman spectra of naphthoic acid measured from the interior of several octanol-filled particles show ±10% amplitude variability day-to-day. This coincides with similar uncertainties in the values of octanol-water partition coefficents computed using the peak-fitting techniques described in the experimental section. Although this level of reproducibility is acceptable for many applications, particularly when considering the advantages of small-

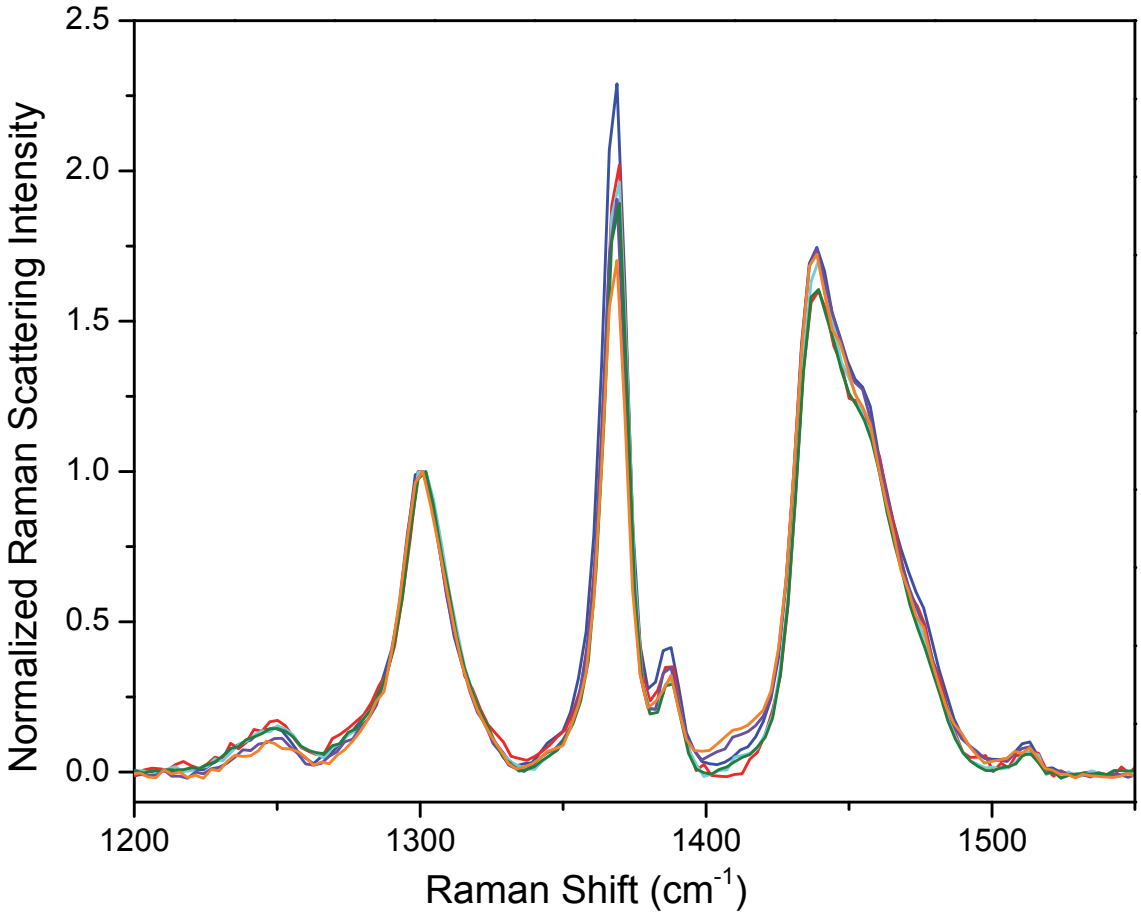

Figure 3.5. Raman spectra of 500 μM (solution concentration) naphthoic acid at pH 2.0 measured from the interior of 6-individual octanol-filled particles. Spectra are normalized to the CH_2-twisting mode (1303 cm^{-1}) to account for day-to-day fluctuations in laser intensity and microscope alignment.

scale partitioning and detection, variability in the measurement remains larger than results obtained using a traditional shake-flask followed by UV-Vis detection. To this end, efforts are being made to address this challenge, primarily in the redesign of a flow cell to efficiently deliver analyte to a single-particle collector.

Solvation of the naphthoic acid within the wide (32-nm) pore chromatographic silica should be dominated by octanol, having a mole fraction in the pores of 94% compared to 6% C_{18} alkyl chains. However, the longer C_{18} alkyl chains represent 13% of the methylene groups within the pores. To test whether the C_{18} chains significantly change the solvation of naphthoic acid in the pores compared to a bulk octanol phase, the partitioning of naphthoic acid between octanol and water at pH = 2 was measured using a traditional EPA shake-flask approach[6] with UV-Vis detection. The resulting log partition coefficient, log K_{ow} = 3.04±0.06 is indistinguishable[29] from the Raman microscopy result, log K_{ow} = 2.9 ± 0.1. These results indicate that the C_{18} chains within the pores do not produce a significantly different solvation environment for naphthoic acid compared to bulk octanol.

3.3.3 Measuring pH Dependent Octanol-water Distribution of Naphthoic Acid

For acidic or basic compounds, the protonation state of the molecule plays a major role in governing octanol-water partitioning. The changes in molecular charge, as protons are added or removed from the molecule, leads to pH dependent distribution of the molecule between the two phases. To provide a measure of lipophilicity of an acidic or basic compound near its pKa, where both protonated and deprotonated forms of the molecule can exist, the distribution coefficient D or its log expresses the ratio of sum of

concentrations of protonated and deprotonated forms in octanol, relative to the sum of their concentrations in water:

$$D = \frac{[HA_o]+[A-_o]}{[HA_w]+[A^-_w]} \quad \text{[Eq. 3.4]}$$

The pH-dependent distribution of a compound can be modeled by combining simple acid-base equilibrium (Eq. 3.5) with the definition of the distribution coefficient (Eq. 3.4):

$$K_a = \frac{[A^-_w][H^+_w]}{[HA_w]} \quad \text{[Eq. 3.5]}$$

$$D = \frac{K_{ow}^{HA} + K_{ow}^{A-}\left(10^{(pH-pKa)}\right)}{\left(1+10^{(pH-pKa)}\right)} \quad \text{[Eq. 3.6]}$$

where K_{ow}^{HA} and K_{ow}^{A-} are the octanol-water partition coefficients of the protonated and deprotonated forms of the compound.

To test the measurement of a pH-dependent octanol-water distribution, Raman scattering from naphthoic-acid partitioned into the octanol-filled pores was measured as a function of pH at intervals of 0.5-pH units around the pK_a of naphthoic acid (Figure 3.6A). Raman spectra show the intensity of the naphthoic acid ring-breathing mode decreasing as the pH of the surrounding aqueous solution is increased, while scattering from the CH_2-twisting modes of octanol and C_{18} chains remains constant. This is the expected result, as the deprotonated naphthoate anion should be less soluble than neutral naphthoic acid in the nonpolar octanol phase. Converting the Raman scattering intensity from the ring-breathing mode of naphthoic acid and naphthoate to the within-pore concentrations (see above) yields distribution coefficient data (Figure 3.6B), which can be fit to Eq. 3.6. The pH dependence of the distribution coefficient is well fit by the model allowing determination of the partition coefficients of both naphthoic acid and naphthoate, and the pK_a of the proton transfer reaction. The log partition coefficients of the two species thus

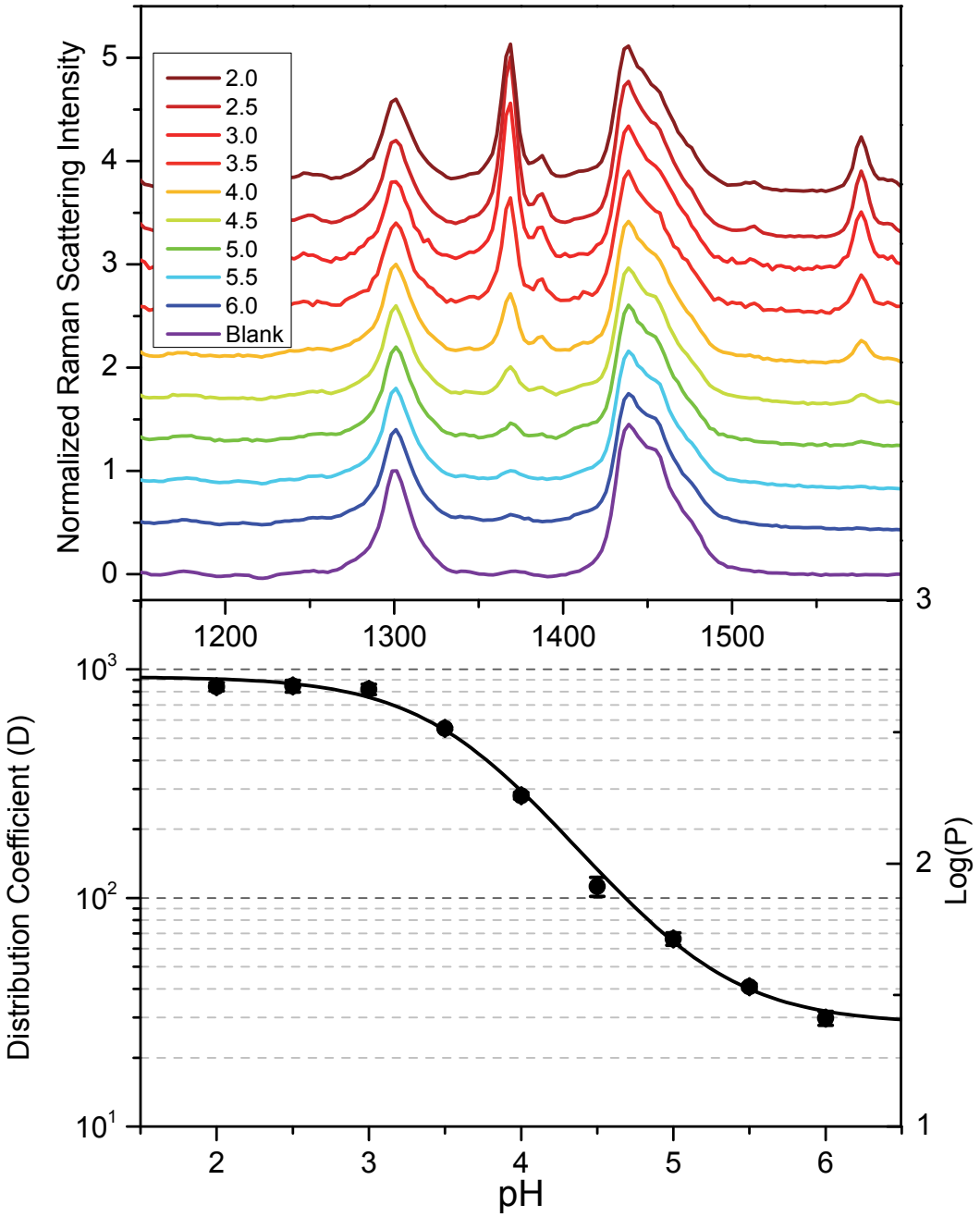

Figure 3.6. A. Normalized Raman scattering collected from the interior of a single octanol-filled chromatographic particles equilibration with 500 µM naphthoic acid in aqueous solution with pH ranging from 2 to 6. Note the naphthoic acid ring-breathing mode at 1382 cm^{-1}. B. Distribution coefficient as a function of pH measured from within a single particle.

determined are log K_{ow}^{HA} = 2.9 ± 0.1 and log $K_{ow}^{A^-}$ 1.5 ± 0.2 and are in agreement with shake-flask results, 3.04 ± 0.06 and 1.505 ± 0.009; the fitted value of the pK_a =3.6 ± 0.1 is within its uncertainty of the literature value, pK_a = 3.69.[28]

3.3.4 Comparing Octanol-water Partitioning to Sorption to a C_{18} Surface

Retention of a compound on a reversed-phase chromatographic column is often used to predict octanol-water partitioning.[1,11] It is relevant, therefore, to examine how sorption of naphthoic acid at the C_{18}-water interface compares to its distribution into octanol-filled pores in the same C_{18} stationary phase material. When naphthoic acid is deprotonated, the molecule becomes surfactant-like, with a charged carboxylate group and hydrophobic naphthalene ring. A surfactant can lower the surface tension of a C_{18}-water interface, driving its accumulation at the surface.[30-33] It is anticipated that sorption of naphthoate ions at a C_{18}-water interface would differ significantly from its partitioning from water into octanol. To test this hypothesis, Raman scattering from naphthoic-acid accumulating at the C_{18} interface from aqueous solution was measured across the same pH range as octanol-water partitioning, and the results compared in Figure 3.6 to partitioning into octanol. Quantification of naphthoic acid in the C_{18} chains was based on scattering from the ring-breathing mode relative to scattering from the CH_2-twisting mode of the surface-bound C_{18} chains (Eq. 3.7).

$$[Naphthoic\ Acid] = F\frac{A_{Naphthoic}([C_{18}]\times 17_{CH_2})}{A_{CH_2}} \qquad \text{[Eq. 3.7]}$$

The concentration of the C_{18} chains in the interphase, [C_{18}] = 1.88 M, was determined by dividing the moles of C_{18} (from carbon analysis) by the volume of the C_{18}-phase

determined from the difference in volume displacements between the C_{18}-derivitized silica, and the same silica where the C_{18} phase was removed by oxidation in a furnace (see the Experimental Section). To ensure that the interfacial population of naphthoate did not saturate the C_{18} surface, an accumulation isotherm was measured over a range of naphthoic acid concentrations; 50-μM source-phase was used for pH values at or below pH 3.5 to ensure results remained within the linear response region of the isotherm (Figure 3.7). Beyond pH 3.5 naphthoic acid concentrations were increased 10-fold to maintain sensitivity for detection; at pH values greater than 3.5, sorption of naphthoic acid is greatly decreased and surface concentrations remain within the linear isotherm region at the higher solution concentration.

In agreement with the expectations, the results in Figure 3.8 show that naphthoate anion is indeed surface-active and accumulates at the C_{18}-water interface at a 2.0-fold greater concentration than in octanol. It is interesting to note that an even greater discrepancy exists with naphthoic acid at the low-pH limit, where naphthoic acid accumulates in the C_{18} phase at a 5.2-fold greater concentration than it partitions into octanol. This is likely due to a combination of both interfacial activity of naphthoic acid and strong hydrophobic interactions where naphthoic acid can avoid contact with water in the less polar C_{18} phase compared to ocatanol. These results demonstrate the difficulty in predicting partition coefficients based on reversed-phase chromatographic retention, where a single correction factor would not accurately predict partitioning across the pH range of an acid-base equilibrium. The results further support the concept of measuring accumulation of solutes into octanol-filled pores in a reversed-phase chromatographic support material as a realistic model for octanol-water partitioning.

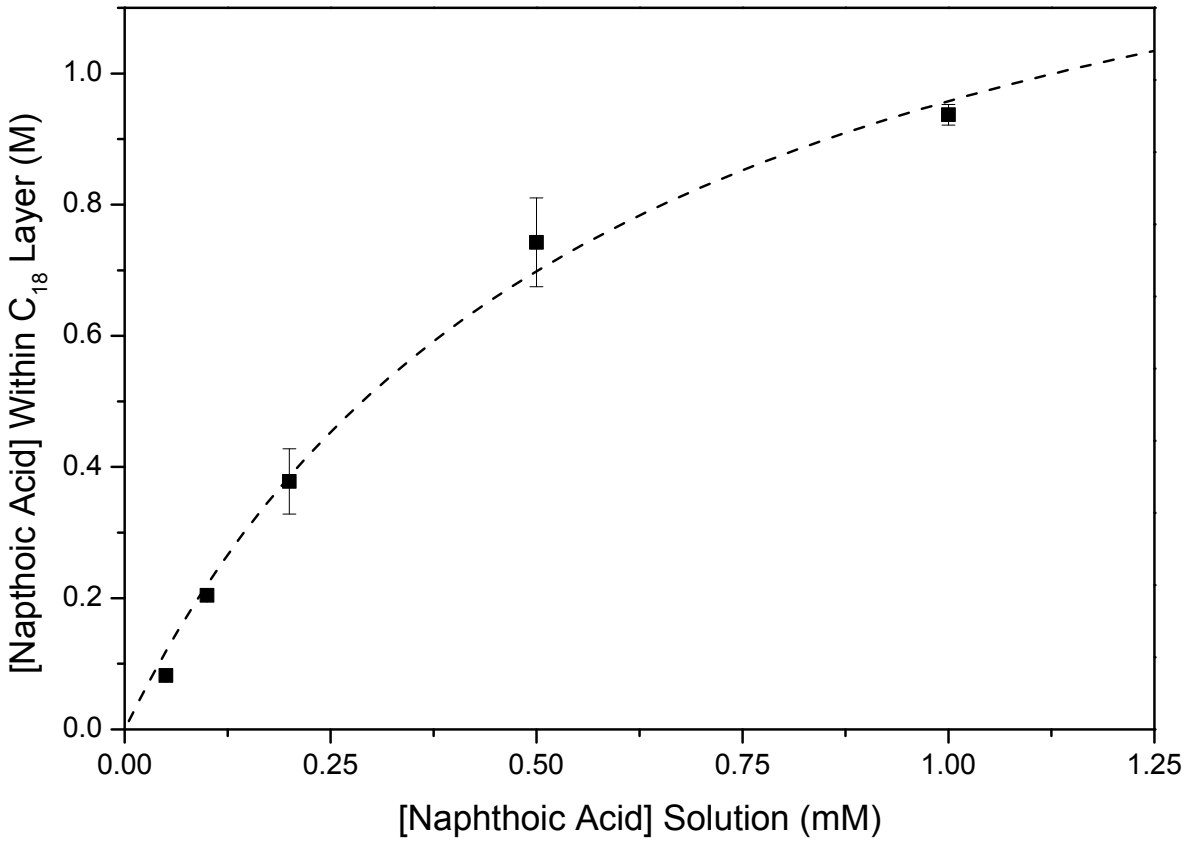

Figure 3.7. Adsorption isotherm for naphthoic acid accumulating on a C_{18} surface from pH 2.0 aqueous buffer.

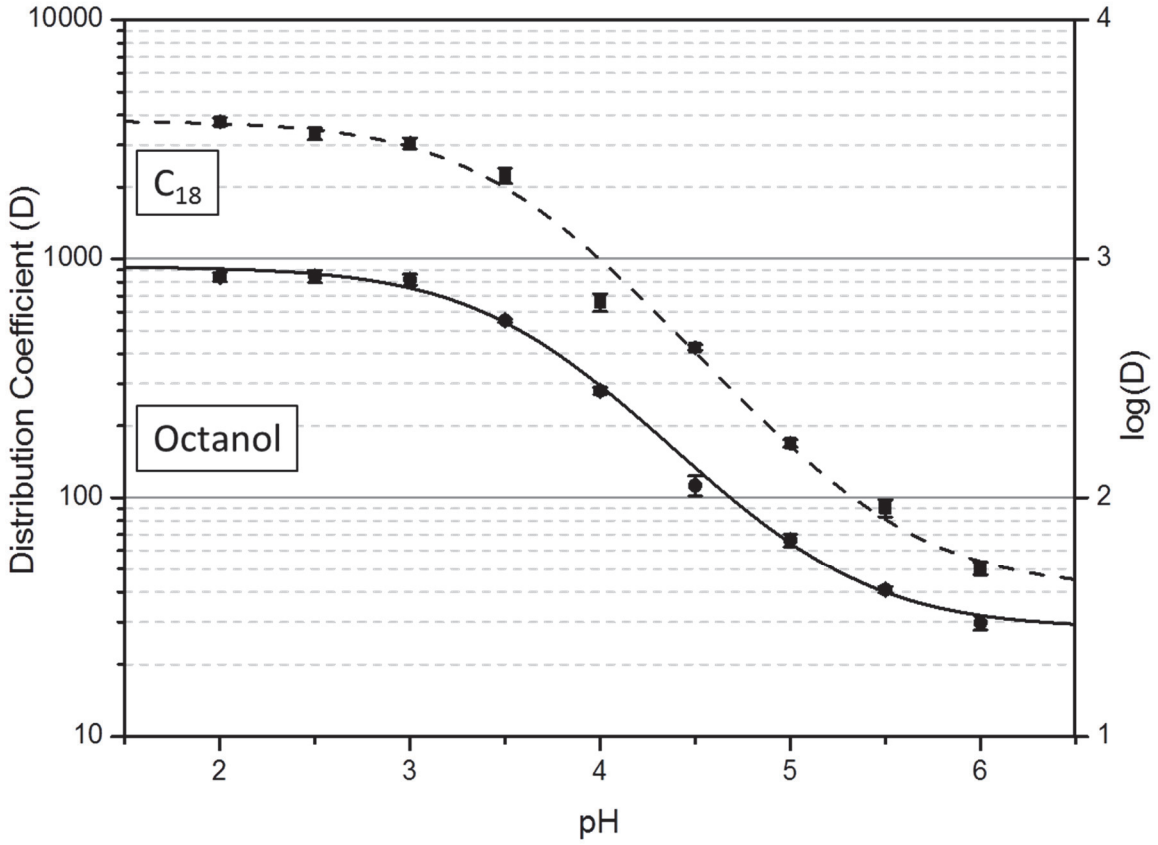

Figure 3.8. Distribution of naphthoic acid into octanol (round dots, solid lines) and C_{18} (squares, dashed line) from aqueous solution versus pH. The greater distribution coefficient of naphthoic acid into C_{18} chains as compared to octanol ranges from a factor of 5.2 at low pH to a factor of 2.0 at high pH.

3.3.5 Sample Size and Throughput

One goal of this work was decreasing the amount of sample required to measure octanol-water partition coefficients. This could be especially important for characterizing new drug candidates or small quantities of potential environmental threats. From the concentration of naphthoic acid in the octanol/C_{18}-filled pores in the low pH limit (0.42 M) and the pore volume of a single 10-μm diameter particle (0.34 pL), it is possible to determine the amount or analyte required to satisfy the single-particle collector, 0.14 pmol. The source phase would need to supply a ~20-fold excess of this amount to avoid depletion of the analyte concentration or 2.8 pmol. The volume of a 500 μM solution required to supply this amount analyte is 5.6 nL, which is a ~20-fold decrease compared to microfluidic approaches.[7-10] The sample amount and source phase volume required for this measurement scales linearly the octanol volume, which is proportional to the particle volume. While 10-μm particles are convenient for handling, the quality of the laser beam focus, which has a radial size ($1/e^2$) of w = 0.59 μm,[24] allows detection within particles as small as 2-μm diameter with no loss in sensitivity, where the probe volume can reside entirely within a particle of this size.[34] This is apparent in the quality of the laser focus produced in the center of a 2-μm particle (Figure 3.9, inset). Since particle volume varies with the cube of the particle diameter, a 125-fold reduction in the required sample volume can be achieved with a 2-μm diameter particle with no sensitivity loss. The amount of naphthoic acid needed to equilibrate this particle (with a 20-fold molar excess) is 22 fmol corresponding to 45 pL of a 500-μM source-phase solution.

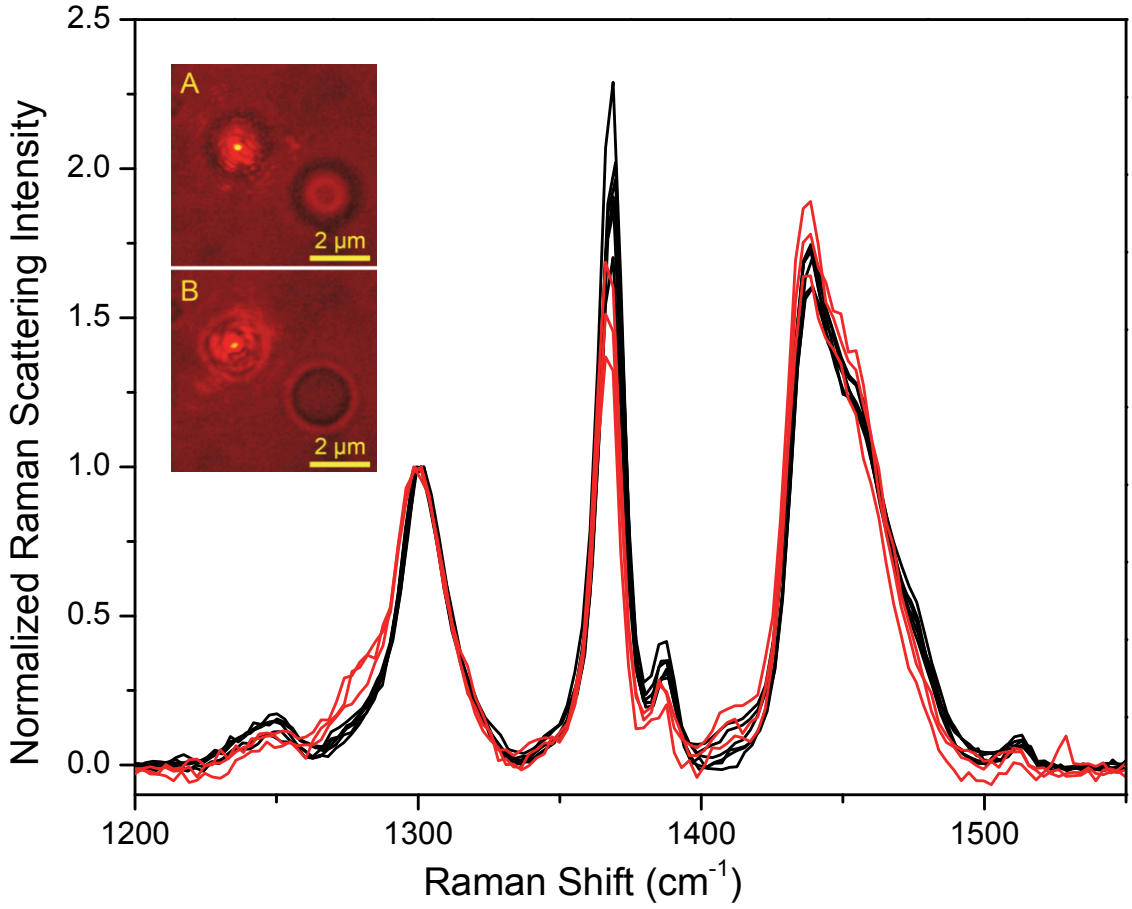

Figure 3.9. Raman spectra of 500 µM (solution concentration) naphthoic acid at pH 2.0 measured from the interior of 6-individual 10-µm octanol-filled particles (Black) and 3 individual 2-µm particles (Red). Spectra are normalized to the CH_2-twisting mode (1303 cm^{-1}) to account for day-to-day fluctuations in laser intensity and microscope alignment. Inset: A. Image of the focused laser spot reflected at the coverslip solution interface directly below a 2-µm particle. B. Image of the focused laser spot translated 1 µm in the z-dimension to the center.

3.3.6 Measuring Raman Scattering from the Interior of Individual 2-µm Silica Particles

Following the procedure outlined above for measuring Raman scattering from the interior of individual 10-µm particles, Raman scattering was collected from the interior of individual 2-µm C_{18} silica particles selected from a population of nominal '3-µm' particles, YMC ODS-A, YMC America. These are nearly equivalent to the 10-µm particles, being monofunctional, C_{18}-derivitized, and endcapped with trimethylchlorosilane. The particles have a mean diameter of 2.8 µm and an average pore-diameter of 12.5 nm. Raman spectra collected from the interior of 2-µm particles (red) exhibit comparable signal-to-noise to spectra from 10-µm particles (black), indicating no loss of sensitivity; see Figure 3.9. This result confirms that the confocal probe volume remains within a 2-µm particle. Also shown in Figure 3.9 (inset) are photos taken through the microscope eyepiece of the laser-spot focused at the coverslip-solution interface just below a 2-µm particle (A) and translated 1 µm in the z-dimension to the center of the particle (B). Here, no distortion is observed in the focused laser spot when the beam is brought to the center of particle, as might be expected from the structured porous silica. This is due to the small size of the silica features (~λ/50) which are well below the Mie scattering limit and the nearly-matching refractive index solvents which lower the dielectric contrast of the silica-solvent interface.[23] The quality of the focus indicates that the confocal imaging of the scattered radiation will confine detection to within the particle interior.

There are some differences in the 2-µm particle results compared to the 10-µm particle results, as shown in Figure 3.9. The naphthoic acid-to-CH_2 twist peak ratios have changed from 1.07±0.08 in 10-µm particles to 0.75±0.07 in 3-µm particles, indicating a

lower within-pore naphthoic acid concentration. We hypothesize that the mol-fraction of C_{18}-chains compared to octanol within the smaller-pore-diameter silica (from 0.059 in large pore silica to ~0.156 in small pore silica, based on a cylindrical pore model) has led to a more significant influence of the C_{18} chains, lowering the partition coefficient compared to octanol. Additionally Raman scattering from the CH_2-twisting mode of octanol and C_{18} acyl chains in the smaller-particle silica has produced a broader peak with a small shoulder, attributable to increased disorder in the acyl-chain structure within the pores.[35] This result is not unexpected; surface density of C_{18}-chains in small-particle pore silica is lower by nearly 30%: 2.48 μmol/m^2 compared to 3.43 μmol/m^2 for the 10-μm silica should lead to differences in chain interactions and conformations. The greater surface curvature of the smaller 12.5-nm pores of the smaller particles versus the 31.9-nm pores of the 10-μm particle silica should also contribute to changes in C_{18}-acyl chain conformations.

Traditional methods of measuring octanol-water partition coefficients are tedious and slow. With both generator column and shake-flask methods, equilibration times range from tens of minutes to hours. This is because the large volumes of source and receiver phases, where the achievement of equilibrium is slow due to molecular transport over large distances. In the present work, equilibration is fast as a consequence of the efficiency of diffusive transport over small distances that characterize the receiver and source phases. The time required for accumulation of 500 μM naphthoic acid (pH 2.0) into a 10-μm octanol-filled particle is ~40 s (see Figure 3.10) which within 30% of the diffusion-limited transport time expected from a hemispherical volume containing the 840-fold excess of molecules required to reach equilibrium. Because quantification by confocal-Raman

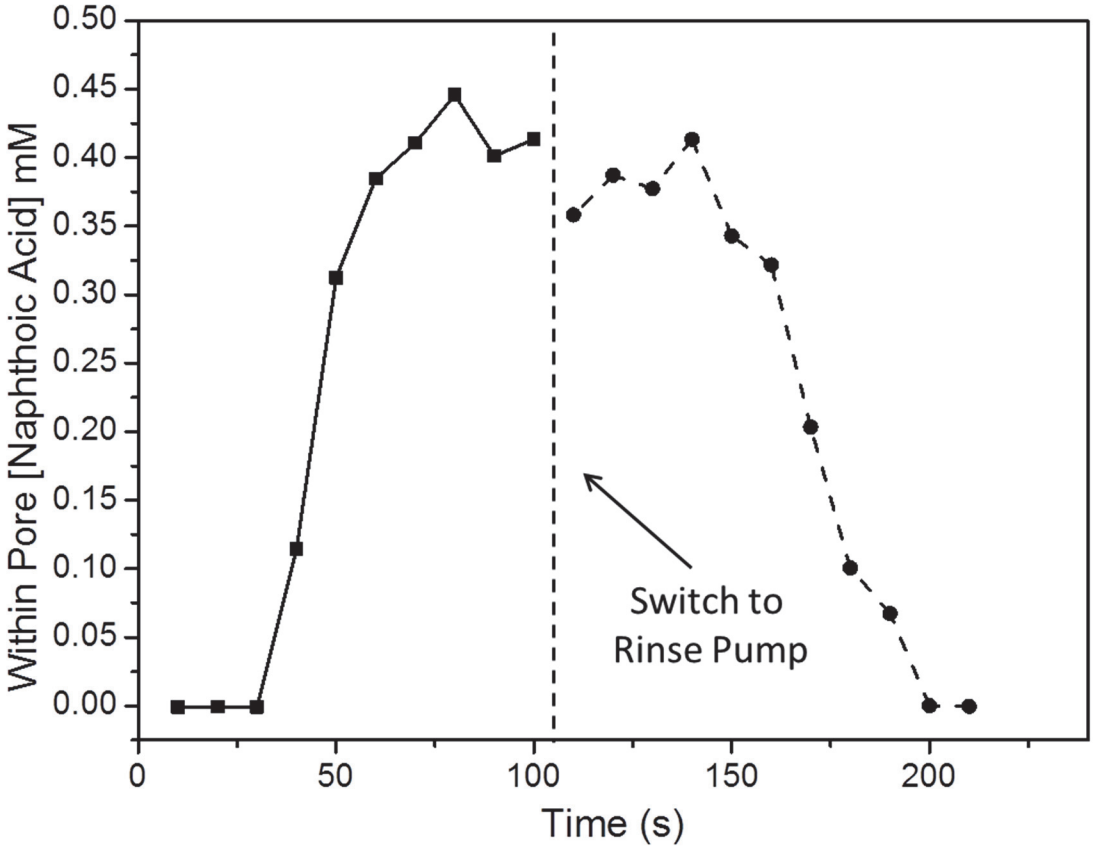

Figure 3.10. Time-dependent accumulation and release of naphthoic acid from octanol measured in a single particle, demonstrating the reversibility and potential reuse of octanol-filled particles in screening applications.

detection is *in situ* within the receiver phase, separation of the two phases and *ex-situ* measurement are avoided, which means that the measurement can be achieved within this partitioning equilibration time.

Octanol-water partitioning is commonly used in screening applications to determine the therapeutic potential of drug candidates or the environmental risk of toxic compounds. Using traditional methods, screening is costly in both time and reagents. In-situ within a single chromatographic particle eliminates the need for large quantities of sample and reagents. With C_{18}-functionalized particles and octanol-saturated water, the within-particle octanol phase remains confined to the particle pores. Because of the small collection volume, transport out of the octanol phase is fast, as shown in Figure 3.10. This means that multiple partitioning measurements could be made using a single particle by exchanging the analyte-containing source phase with buffer which quickly prepares the particle for evaluation of a new sample. This approach to the measurement should lead to greater reproducibility, which is presently ±10% particle-to-particle (Figure 3.5). While this level of reproducibility is acceptable for many sample-limited applications, the variability is presently greater than results obtained using traditional shake-flask methods. The precision of the within-particle measurement should benefit from improvements in sample handling to deliver analyte to a single-particle collector.

3.4 References

(1) Sangster, J. *J. Phys. Chem. Ref. Data* **1989**, *18*, 1111-1229.

(2) Leeson, P. D.; Springthorpe, B. *Nat. Rev. Drug Discov.* **2007**, *6*, 881-890.

(3) Edwards, M. P.; Price, D. A. In *Annual Reports in Medicinal Chemistry*; Macor, J. E., Ed.; Academic Press: San Diego, CA, 2010; Vol. 45, pp 380-391.

(4) Calabrese, E. J.; Baldwin, L. A. *Performing Ecological Risk Assessments*; Lewis Publishers: Chelsea, MI, 1993.

(5) Ellington, J. J.; Floyd, T. L. *Measuring Octanol/Water Partition Coefficients by the "Slow-Stirring" Method*; United States Environmental Protection Agency, U.S. Government Printing Office: Washington DC, 1995.

(6) *Partition Coefficient (n-octanol/water), Shake Flask Method, Product Properties Test Guidelines OPPTS 830.7550*; United States Environmental Protection Agency, U.S. Government Printing Office: Washington DC, 1996.

(7) Carlsson, K.; Karlberg, B. *Anal. Chim. Acta* **2000**, *423*, 137-144.

(8) van der Linden, H. J.; Jellema, L. C.; Holwerda, M.; Verpoorte, E. *Anal. Bioanal. Chem.* **2006**, *385*, 1376-1383.

(9) Lopez-Martinez, M. J.; Mulder, P. P. M. F. A.; Born, P.; Verpoorte, E. Fast Determination of Distripution Coefficients in a Poly(Dimethylsiloxane) Chip. In *15th International Conference on Miniaturized Systems for Chemistry and Life Sciences*; Landers, J. P., Ed.; Chemical and Biological Microsystems Society: Seattle, WA, October 2-6, 2011; p 768.

(10) Stephan, K.; Saab, J.; Mokbel, I.; Goutaudier, C.; Ferrigno, R. *Fluid Phase Equilib.* **2014**, 380, 116-120.

(11) Johann, C.; Garidel, P.; Mennicke, L.; Blume, A. *Biophys. J.* **1996**, *71*, 3215-3228.

(12) Poole, S. K.; Poole, C. F. *J. Chromatogr. B* **2003**, *797*, 3-19.

(13) Snyder, L. R.; Kirkland, J. J.; Dolan, J. W. *Introduction to Modern Liquid Chromatography*, 3rd ed.; Wiley: Hoboken, NJ, 2009.

(14) Cecchi, T. *Crit. Rev. Anal. Chem.* **2008**, *38*, 161-213.

(15) Sander, L. C.; Wise, S. A. *J. Chromatogr. A* **1993**, *656*, 335-351.

(16) Tewari, Y. B.; Miller, M. M.; Wasik, S. P.; Martire, D. E. *J. Chem. Eng. Data* **1982**, *27*, 451-454.

(17) DeVoe, H.; Miller, M. M.; Wasik, S. P. *J. Res. of the Natl. Bur. of Stand. (U. S.)* **1980**, *86*, 361-366.

(18) *Partition Coefficient (n-octanol/water), Generator Column Method* Product Properties Test Guidelines OPPTS 830.7560, United States Environmental Protection Agency, U.S. Government Printing Office: Washington DC, 1996.

(19) Houlne, M. P.; Sjostrom, C. M.; Uibel, R. H.; Kleimeyer, J. A.; Harris, J. M. *Anal. Chem.* **2002**, *74*, 4311-4319.

(20) Gasser-Ramirez, J. L.; Harris, J. M. *Anal. Chem.* **2009**, *81*, 7632-7638.

(21) Gasser-Ramirez, J. L.; Harris, J. M. *Anal. Chem.* **2009**, *81*, 2869-2876.

(22) Gasser-Ramirez, J. L.; Harris, J. M. *Anal. Chem.* **2010**, *82*, 5743-5750.

(23) Kitt, J. P.; Harris, J. M. *Anal. Chem.* **2014**, *86*, 1719-1725.

(24) Kitt, J. P.; Bryce, D. A.; Harris, J. M. *Appl. Spectrosc.* **2015**, *69*, 513-517.

(25) Williams, K. P. J.; Pitt, G. D.; Batchelder, D. N.; Kip, B. J. *Appl. Spectrosc.* **1994**, *48*, 232-235.

(26) Woodburn, K. B.; Doucette, W. J.; Andren, A. W. *Environ. Sci. Technol.* **1984**, *18*, 457-459.

(27) Castell, O. K.; Allender, C. J.; Barrow, D. A. *Lab Chip* **2009**, *9*, 388-396.

(28) Sturtevant, J. M. *Proc. Natl. Acad. Sci.* **1982**, *79*, 3963-3967.

(29) Student. *Biometrika* **1908**, *6*, 1-25.

(30) Horvath, C.; Melander, W.; Molnar, I.; Molnar, P. *Anal. Chem.* **1977**, *48*, 2295-2305.

(31) Bidlingmeyer, B. A.; Deming, S. N.; Price Jr., W. P.; Sachok, B.; Petrusek, M. *J. Chromatogr.* **1979**, *186*, 419-434.

(32) Deelder, R. S.; Van Den Berg, J. H. M. *J. Chromatogr.* **1981**, *218*, 327-339.

(33) Cantwell, F. F. *J. Pharm. Biomed. Anal.* **1984**, *2*, 153-164.

(34) Bridges, T. E.; Houlne, M. P.; Harris, J. M. *Anal. Chem.* **2004**, *76*, 576-584.

(35) Gaber, B. P.; Yager, P.; Peticolas, W. L. *Biophys. J.* **1978**, *21*, 161-176.

CHAPTER 4

CONFOCAL RAMAN MICROSCOPY CHARACTERIZATION OF HYBRID SUPPORTED PHOSPHOLIPID BILAYERS WITHIN INDIVIDUAL C_{18}-FUNCTIONALIZED CHROMATOGRAPHIC PARTICLES

4.1 Introduction

Measuring interactions between aqueous-phase molecules and phospholipid membranes is critical for predicting and understanding drug efficacy in pharmaceutical screening and for estimating toxicity and lifetimes of dangerous small molecules in the membrane.[1-7] A stable model membrane for these types of studies has been developed, comprised of an upper leaflet of amphiphilic lipid molecules which forms a stable monolayer with a lower-leaflet of close-packed, hydrophobic n-alkyl chains that are covalently bound to a solid support. These model membranes, termed hybrid supported phospholipid bilayers (HSBs), were originally generated by adsorption of phospholipids to self-assembled n-alkane-thiol monolayers on gold and silver substrates[8,9] and used for electrochemical,[10-12] infrared reflection,[10] surface-enhanced Raman,[12,13] and surface-plasmon resonance measurements.[14,15] More recently, this concept has been adapted to produce hybrid-bilayers in C_{18}-modified porous silica for use in chromatographic studies[16-18] where retention of many small-molecules and membrane-active peptides on the hybrid

bilayer was found to be comparable to their relative affinities for phospholipid vesicle membranes. Although chromatographic studies have produced promising results for these studies, the structure of the hybrid bilayer within the pore network of chromatographic silica remains uncharacterized. The techniques typically employed to investigate planar hybrid-bilayers cannot be applied in porous silica networks either because the internal surface is inaccessible to the probe, as in atomic force microscopy or because the probing techniques are incompatible with the water-filled pores as in infrared spectroscopy.

Spectroscopic probing of hybrid bilayers using Raman spectroscopy can provide insight into their formation, structure, and functioning;[19-22] additionally Raman spectroscopy is compatible with both silica and water. Raman scattering is a weak effect, however, detection of which is challenged by the sensitivity needed to observe a small number of lipid molecules in the bilayer of a vesicle or a planar supported bilayer. The sensitivity challenge of Raman spectroscopy has been overcome previously, however, by measuring Raman scattering from within porous silica particles using confocal Raman microscopy.[23-27] Here the confocal probe volume is confined to the interior of an individual chromatographic particle, where the Raman signal is dominated by the large surface area provided by the highly porous support. Within-particle spectroscopy provides a solution to both the sensitivity challenge of Raman spectroscopy and allows *in-situ* probing of the hybrid bilayer within the pore network. The ability to measure Raman scattering from within porous silica initially seems counterintuitive as one anticipates large significant loss of excitation and collection efficiency due to Mie scattering. However, the ~30 nm size of the pores in xerogel silica[28] lie well below the Mie scattering limit of the 647.1 nm excitation source;[29] this, combined with the nearly-matching refractive indices of the silica

support and aqueous environment, allows a well-defined submicrometer confocal probe volume to be maintained at the center of the particle and high quality Raman spectra to be collected from within a single particle.[23-26]

Confocal Raman microscopy has been utilized previously to probe *in-situ* the chemistry within individual chromatographic silica particles, including studies of functionalization of the silica surface,[27] the interfacial solvation environment of C_{18}-stationary phases,[24,25] the mechanism of surfactant-mediated ion-pair retention,[23] femtoliter-scale solid-phase extraction of PAH compounds,[26] and partitioning from water into octanol confined to the pores of an individual chromatographic particle.[30] In this work, we propose extending within-particle confocal Raman spectroscopy to investigate the structure of hybrid-supported phospholipid bilayers deposited on the interior surfaces of chromatographic C_{18}-silica particles.

Raman spectroscopy is well-suited to the study of lipid bilayer structure.[20-22,31] Acyl-chain disorder can be monitored by measuring relative Raman scattering intensities from well-known structural markers in the acyl chain C-C stretching (1030-1150 cm^{-1}), C-H bending (1400-1500 cm^{-1}), CH_2 twisting (1260-1340 cm^{-1}), and C-H stretching (2800-3100 cm^{-1}) regions of the spectrum.[19,31] Although it is common to measure changes in indicator bands at specific wavenumber values to elucidate structural changes,[22,32,33] this approach allows the investigation of only isolated intensity changes or peak shifts. Additionally, subtle spectral changes and changes in overlapping peaks are not easily resolved. A broader approach to spectral analysis that allows resolution of correlated spectral changes as a function of varying experimental conditions (e.g., time, temperature, composition…) is self-modeling curve resolution (SMCR).[34] SMCR is a multivariate

statistical method that resolves correlated spectral changes by eigenvector decomposition of the spectral data. SMCR has been used previously to detect temperature-dependent spectral changes from lipid membranes of individual optically-trapped vesicles.[20]

In this work, within-particle confocal Raman and self-modeling curve resolution are employed to investigate the formation, and temperature-dependent structure of hybrid supported phospholipid bilayers deposited on the interior surfaces of individual C_{18}-chromatographic silica particles. More specifically, 10-μm diameter C_{18}-functionalized silica particles deposited in a microscope flow cell are equilibrated with a flowing solution of 1,2-dimyristoyl-sn-glycero-3-phosphocholine (DMPC) in aqueous 15% isopropanol. Spectral changes associated with phospholipid adsorption and acyl-chain structure are monitored as a function of time and the spectra analyzed using self-modeling curve resolution. Samples of the same chromatographic particles, equilibrated *ex-situ* under equivalent conditions, are used for carbon analysis to determine phospholipid surface coverage, for differential scanning calorimetry (DSC) to measure endotherms of hybrid-bilayer melting transitions and for temperature-controlled Raman microscopy experiments to examine the temperature-dependent structure of the bilayer acyl chains. The DSC endotherm of the DMPC hybrid-bilayer phase transition is contrasted with the endotherm of a sample of DMPC vesicles, where the within-particle hybrid-bilayer phase transition is shifted to higher temperature and is much broader than the DMPC vesicle transition. Raman spectra from within individual particles are measured as a function of temperature across the hybrid-bilayer phase transition and component Raman spectra and corresponding composition vectors computed using self-modeling curve resolution of the temperature dependent data agree with calorimetric endotherms.

The source of the temperature shift and broadening of the within-particle hybrid-bilayer phase transition was investigated by using deuterated DMPC (DMPC-D54) to resolve the phospholipid Raman bands from those arising from the C_{18}. DSC and Raman experiments were carried out with particles containing deuterated-phospholipid hybrid bilayers. DSC thermograms of deuterated DMPC hybrid bilayers were similarly shifted and broadened compared with DDMPC vesicles. Self-modeling curve resolution spectral analysis is used to examine the deuterated hybrid-bilayer phase transition and the source of the temperature shift and broadening of the phase transition.

4.2 Experimental Section

4.2.1 Reagents and Materials

Chromatographic silica particles were obtained from YMC America (YMC-Pack ODS-A, YMC America Inc., Allentown, PA). The particles were spherical, C_{18}-derivitized, monofunctional, and encapped with trimethychlorosilane. The particles had a mean diameter of 10 μm, mean pore diameter of 31.9 nm, specific surface area of 93 m^2/g, and pore volume of 0.80 mL/g as reported by the manufacturer. Elemental analysis of carbon content (MHW Laboratories, Phoenix, AZ) and the particle specific surface area were used to determine the C_{18} surface coverage of 3.7±0.3 $\mu mol/m^2$.

Isopropanol (>99.9%) was obtained from Thermo Fisher Scientific (Waltham, MA). Chloroform (Omnisolv) was obtained from EMD Millipore (Billerica, MA). Deuterium Oxide (>99.9%), was obtained from Sigma-Aldrich (St. Louis, MO). Phospholipids used in this study (1,2-dimyristoyl-sn-glycero-3-phosphocholine (DMPC) and 1,2-dimyristoyl-d54-sn-glycero-3-phosphocholine (DMPC-D54)) were obtained from

Avanti Polar Lipids (Alabaster, AL). Phospholipids were diluted into chloroform and stored at -15 ^{o}C until use. Water used for this experiment was filtered using a Barnstead GenPure UV filtration system (ThermoFisher Scientific, Waltham, MA) and had a minimum resistivity of 18.0 MΩ·cm.

Temperature controlled experiments were conducted in a brass microscopy sample cell. The cell consisted of a cylindrical 3 mm o.d., 2 mm i.d. brass tube which transitions to a 5 cm wide base. The 2 mm inner diameter of the opening at the top of the tube was tapered to 0.5 mm at the base to prevent formation of a temperature gradient across the fluid in the measurement portion of the cell. A 22 mm × 22 mm glass coverslip was attached to the base of the cell using 140 μm thick double stick tape with a 0.25 mm radius hole cut in the center to allow fluid in the sample cell to contact the glass coverslip. The brass microscopy cell was covered by a jacketed copper block and mounted on a silver stage (Technical Video Ltd., Port Townsend, WA). The block is cooled by flowing chilled 50/50 water/ethylene glycol solution through the copper jacket and Peltier stacks on the silver stage using a magnetic drive pump (Micropump Inc., Vancouver, WA). Cell temperature is adjusted using a proportional-integral-derivative (PID) controller to modulate the current supplied to the pair of Peltier on the silver stage. Sample temperature was measured using a thermocouple inserted into the base of the sample cell. A diagram of the temperature control apparatus and well cell has been described previously.[35]

Microfluidic flow cells for Raman microscopy were constructed by drilling two 2.5-mm holes in a 3-mm-thick, 25-mm-diameter circular Pyrex glass top plate (VWR, Radnor, PA) and attaching 2.4-mm-o.d. Luer adapters (Value Plastics, Inc., Fort Collins, CO) using Devcon 5-min epoxy (ITW Devcon, Danvers, MA). The top plate was attached

to a 22 mm × 22 mm No. 1 glass coverslip (Gold Seal, Erie Scientific Co., Portsmouth, NH) using 140-μm thick 3M double-stick tape (TapeCase Ltd., Elk Grove Village, IL) where a 2.5-mm × 11-mm channel was cut between the inlet and outlet ports, allowing flow through a channel between the Luer adapters. All tubing used was 1.6-mm i.d. × 2.4-mm o.d. Viton elastomer (Cole-Parmer, Vernon Hills, IL). Microscopy cells for measuring standards in solution were constructed by gluing a 12-mm length of 10-mm i.d., 13mm o.d. Pyrex glass tubing to a No. 1 fused silica coverslip using Devcon 5-min epoxy (ITW Devcon, Danvers, MA). Diagrams of both cells have been published previously.[26]

4.2.2 Sample Preparation and Characterization

For phase-transition studies, hybrid-supported bilayers were prepared on the interior surfaces of porous C_{18} particles by adsorption of DMPC or DMPC-D54 from 15% v/v isopropanol/water. This was accomplished by adding 10 mg of C_{18}-derivitized silica to 2 mL of 5 mg/mL DMPC or DMPC-D54 in 15% isopropanol/water and stirring overnight ~15 h. Particles were rinsed three times by centrifugation and then resuspended in 18 MΩ water to ensure no phospholipid remained in the exterior solution. For Raman spectroscopy experiments, a 100 μL aliquot of the final 0.5 mg/mL solution of suspended particles was transferred to the measurement cell and allowed to settle to the coverslip surface. The initial temperature of the cell was set at 15 ^{o}C and then increased at 1 ^{o}C intervals to the final temperature (50 ^{o}C for DMPC and 45 ^{o}C for DMPC-D54). At each temperature, Raman scattering was collected from within three individual particles with 30 s integration times.

To determine C_{18} and phospholipid surface coverages, bare C_{18} and hybrid supported bilayer coated particles were sent for elemental analysis (M.H.W. Laboratories,

Phoenix, AZ). These particles were prepared as described above with the addition of the following steps. Subsequent to rinsing, particles were dried under a stream of nitrogen, placed in an oven at 120 ^{o}C for 15 min, and finally dried under vacuum (120 mTorr) on a warm block (~80 ^{o}C) for 1 h to ensure removal of any remaining water.

4.2.3 Temperature-controlled, Within-particle and Optical-trapping, Confocal Raman Microscopy

A detailed description of the confocal Raman microscope used in this work has been published previously.[26,27] Briefly, the beam from a Kr^{+} laser (Innova 90, Coherent Inc., Santa Clara, CA) operating at 647.1 nm is passed through a band-pass filter, beam expanded and reflected off a dichroic mirror to slightly overfill the back aperture of a 1.4-NA 100X oil immersion objective mounted on an inverted fluorescence microscope frame. Laser radiation is focused by the objective to a ~600 nm-diameter spot. For porous-particle experiments the focused spot is translated to the center of an individual particle. For phospholipid vesicle experiments, polarizability contrast between the lipid bilayer and water allows optical trapping of a single vesicle at the laser focus.[36,37] The scattered light is collected back through the objective and passed through the dichroic mirror. The image is then collimated, directed through a high pass filter, and Raman scattered light is focused on the monochromator slit set to 50 μm, defining the horizontal aspect of the confocal aperture and collected on a CCD device where the vertical dimension of the aperture is defined by binning three rows of pixels (78 μm).[38] To conduct within-particle spectroscopy, the focused laser spot is brought to the coverslip-solution interface where a visible reflected spot is formed. The microscope stage is then translated in the *x* and *y*

dimensions to center a single particle above the reflected spot. The microscope objective is then translated 5-μm upward in the *z* dimension to center the confocal probe volume within the particle.

4.2.4 Spectral Data Analysis

All Raman spectra were baseline-corrected using an algorithm that subtracts a 5-order polynomial fitted to non peak-containing regions of the spectrum executed in Matlab (MathWorks, Natick, MA). Prior to analysis, spectra were offset to eliminate negative values along the baseline and for within-particle experiments normalized to the phospholipid headgroup CN stretching mode (715 cm^{-1}) which is insensitive to bilayer acyl-chain structure.[39] Self-modeling curve resolution of Raman spectra of phospholipid bilayers has been described previously.[20] A brief overview is presented in the Results and Discussion.

4.3 Results and Discussion

4.3.1 Measuring Raman Scattering from a Hybrid Bilayer Adsorbed to the Pore Walls within an Individual C_{18}-Silica Particle

Hybrid bilayers have been previously prepared within C_{18}-functionalized silica particles (on column) for chromatographic determination of small molecule-lipid bilayer partition coefficients in high-performance liquid chromatography.[16-18] Formation of bilayers in chromatography is typically assumed based on lipid-breakthrough curves and confirmed by solvent wash-off and *ex-situ* quantification.[16] Through these results, and

subsequent small-molecule partitioning measurements, which result in similar partition coefficients to those measured in lipid-vesicles, formation of a hybrid bilayer within the porous particles is posited. While retention of lipid suggests hybrid-bilayer formation, little is known about adsorption or structure of lipid molecules within the tightly-curved pore walls in chromatographic silica.

To investigate this question, we measure Raman scattering from phospholipid molecules adsorbed at the C_{18} interface within individual chromatographic silica particles using confocal Raman microscopy. DMPC-filled particles prepared *ex-situ* by equilibration of C_{18}-silica particles with 1,2-dimyristoyl-*sn*-glycero-3-phosphocholine (DMPC) in 15% v/v isopropanol/water[16] were transferred to a microscopy cell, where the particles were allowed to settle on the coverslip surface. Raman spectra from the interior of individual 10-μm particles were collected by manipulating the focused laser spot and confocal collection volume to the center of the particle. A representative spectrum of a bare C_{18}-silica particle and of a particle that has been equilibrated with DMPC (23 ℃) are presented in Figure 4.1. Here, adsorption of phospholipid is confirmed by appearance of phospholipid Raman bands. Specifically, Raman scattering from the C-N stretching mode of the phospholipid head group (715 cm^{-1}) is observed along with an increased CH_2-twisting mode (1296 cm^{-1}).[26,39]

If the adsorbed phospholipid is indeed a hybrid bilayer it should be localized to the pore walls within the silica particle maintaining an open network of the aqueous solution throughout the particle. Thus, it is anticipated that, after bilayer formation, the interior solution can be exchanged and the bilayer should remain intact. To test this, following lipid sorption, the solution was switched from pure water, to 50% aqueous D_2O (Figure 4.2A).

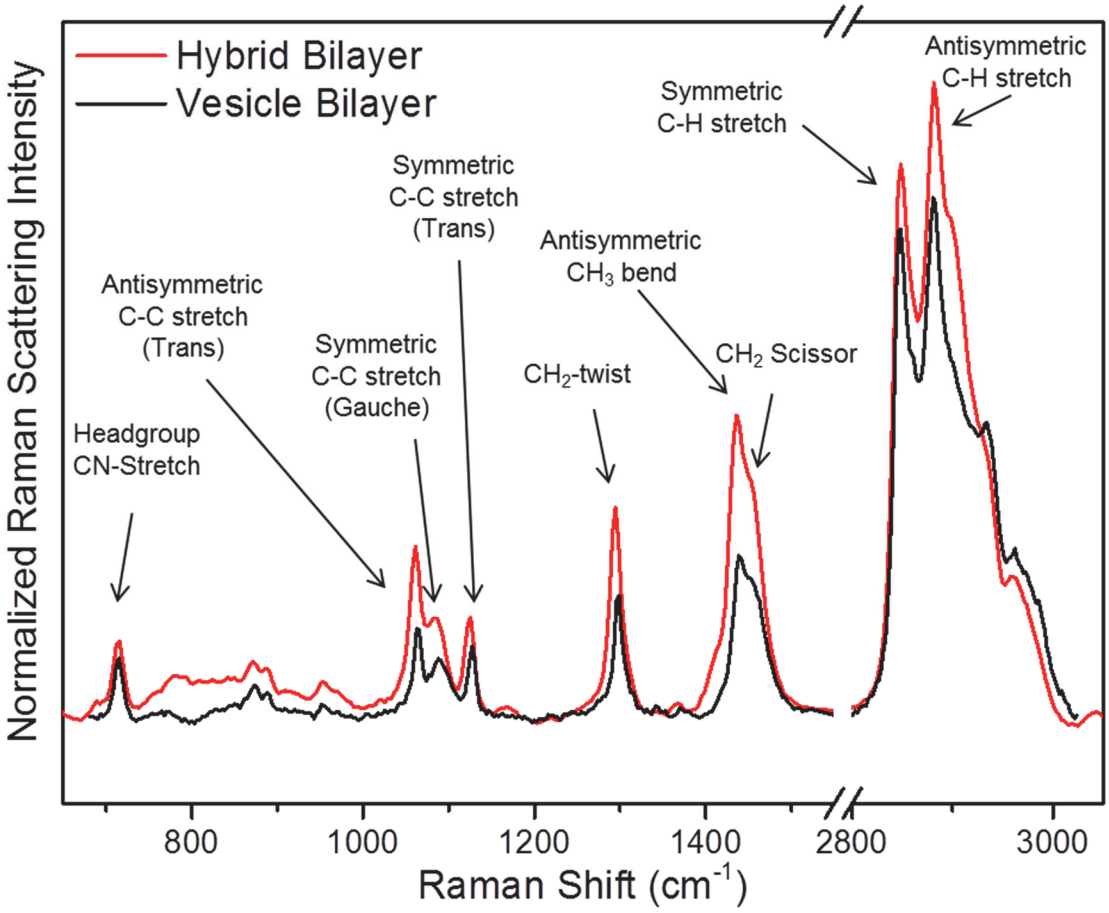

Figure 4.1: Raman spectrum of a DMPC hybrid bilayer within an individual C_{18}-silica particle (Red) compared with the Raman spectrum of an individual optically-trapped vesicle (Black). Both spectra were collected at 23℃.

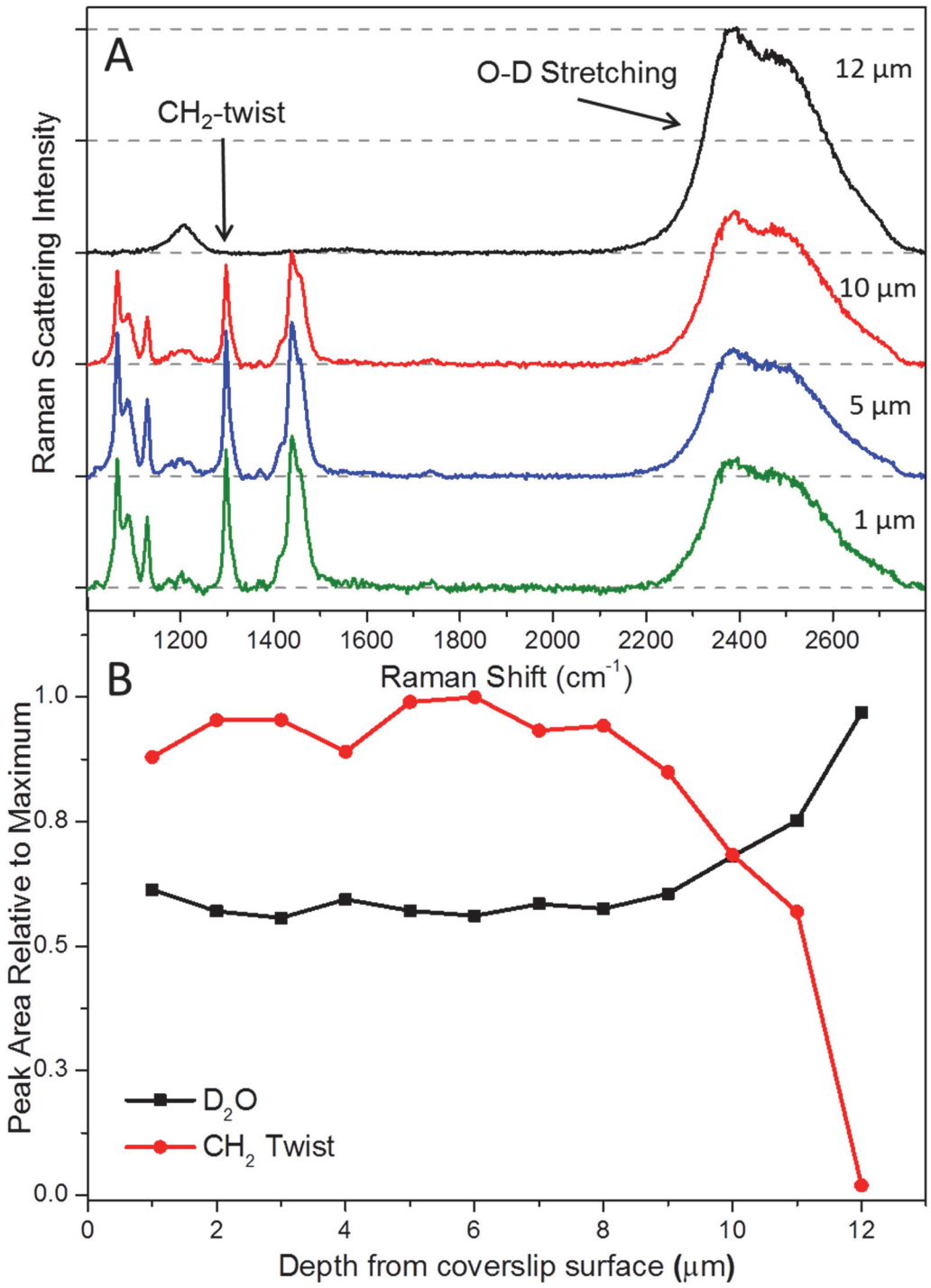

Figure 4.2: Depth profile of a hybrid-bilayer particle. A. four representative Raman spectra from the depth profile of an individual C_{18}-silica particle containing a hybrid bilayer. Spectra were collected as a function of distance from the coverslip–solution interface. B. The peak areas of the CH_2-twisting mode and D_2O O-D stretching modes relative to the maximum area measured during the depth-profile experiment.

Appearance of D_2O Raman bands from 2200-2800 cm^{-1} indicates interior solution exchange, while the constant lipid spectral bands indicate the lipid layer within the particle is maintained. To examine the homogeneity of the within-particle hybrid bilayer and ensure the pore structure is maintained throughout the particle, the O-D stretching modes of D_2O and CH_2-twisting mode of the within-particle hybrid bilayer were monitored as a function of depth in the z-dimension (Figure 4.2A). Here, the O-D stretching modes remain near 60% of maximum (as anticipated based on the solution volume displaced by the silica skeletal structure) until the confocal-probe is translated out of the particle (beginning at ~9 μm from the coverslip-solution interface) and reach maximum intensity when the probe volume has been translated out of the particle and into solution (here solution is no longer being displaced by the silica framework and surface phase). Similarly, the CH_2-twisting mode from the bilayer acyl chains remains at at-or-near maximum throughout the particle dropping off rapidly as the collection volume is translated out of the top of the particle demonstrating homogeneous lipid coverage throughout (Figure 4.2B).

4.3.2 Quantitative Determination of Phospholipid Surface Coverage

An important factor in a model bilayer membrane is the phospholipid packing density. If the packing density is lower than in a vesicle membrane, solution-phase molecules could have greater access to the underlying acyl chains leading to anomalous partitioning behavior. To determine the DMPC packing density within a hybrid-bilayer particle, bare C_{18} particles and hybrid-bilayer particles were dried and sent for carbon analysis. The difference in the mass-fraction of carbon between hybrid-bilayer particles

(0.183±0.002) and the bare C_{18} particles (0.075±0.005) was then used to compute the portion of the carbon fraction in the hybrid-bilayer particles that was due to the phospholipid in the hybrid-bilayer particle. This was accomplished by computing the mass of carbon due to C_{18} ($CMass_{C18}$) in the C_{18} particles by multiplying the mass fraction of carbon due to C_{18} (CFracc18) by the total mass of the sample (Eq. 4.1). By choosing a 1 g sample mass $CMass_{C18}$=$CFracc_{18}$=0.075±0.005 g. Then by rearranging the definition of the mass-fraction equation and using the mass of carbon due to C_{18} and a factor to account for the total mass of C_{18} (F_{C18}=$Mass_{c18}$ /Mass $Carbon_{c18}$) the mass of the silica skeleton is determined (0.91±0.07 g, Eq. 4.2). Finally, using the mass fraction of carbon in the hybrid-bilayer particle ($CFrac_{DMPC+C18}$) mass of carbon due to C_{18}, the factor to correct for total mass of C_{18}, the mass of the silica skeleton, and a factor to convert the mass of carbon due to DMPC to the actual mass of DMPC (F_{DMPC}=$Mass_{DMPC}$/Mass $Carbon_{DMPC}$), the mass of DMPC ($Mass_{DMPC}$=0.152±0.002g) in the hybrid bilayer in 1 g of C_{18} silica can be determined (Eq. 4.3).

$$CMass_{C18} = CFrac_{C18} M_{tot} \qquad \text{[Eq. 4.1]}$$

$$Mass_{sil} = \frac{CFrac_{C18}\left(1 - CFrac_{C18}(F_{C18})\right)}{FC_{C18}} \qquad \text{[Eq. 4.2]}$$

$$Mass_{DMPC} = F_{DMPC}\left[\frac{CFrac_{\,DMPC+C18}(CMass_{C18}(F_{C18}) + Mass_{sil})}{\left(1 - CFrac_{\,DMPC+C18}(F_{DMPC})\right)}\right] \qquad \text{[Eq. 4.3]}$$

Computation of the DMPC surface coverage (3.78±0.08 μmol/m^2) is carried out by converting the mass of DMPC to moles of DMPC and dividing by the specific surface area in 1 g of C_{18}-silica (93 m^2). This surface coverage corresponds to a lipid cross-sectional area of 43.9±0.9 $Å^2$. This area is in remarkably close agreement with cross-sectional areas measured for gel-phase phosphotidyl choline lipids with similar acyl-chain-tail lengths (47.2±0.05 $Å^2$ and 45.9±2 $Å^2$ for C_{14} and C_{16} chain lengths, respectively).[40,41] This

indicates a tightly-packed lipid layer where there are ~2 phosopholipid alkyl chains for each covalently bound C_{18} chain, offering some insight into the structure of the within-particle hybrid bilayer.

4.3.3 Raman Spectrum of a Within-particle Hybrid Bilayer Membrane

One might anticipate that a within-particle hybrid bilayer is structurally similar to a vesicle bilayer at the same temperature with the inner leaflet of C_{18} and outer leaflet of DMPC interacting primarily at the methyl-terminated ends of the lipid tails. If this were the case, one would anticipate that the spectrum of a DMPC hybrid bilayer would have similar structural markers in the Raman spectrum to a vesicle bilayer at the same temperature. However, when the hybrid-bilayer spectrum at room temperature (23℃) is compared with spectrum of an optically-trapped DMPC vesicle at the same temperature, several differences are observed (Figure 4.1). A brief explanation of the structurally informative Raman bands by wavenumber region, and the differences observed between the vesicle spectrum, and hybrid-bilayer spectrum are presented here.

4.3.3.1 Carbon-Carbon Stretching Region (1030-1150 cm^{-1}). Raman bands in the carbon-carbon stretching region are indicative of the ratio of acyl-chain gauche and trans conformers. The pair of narrow peaks observed in the hybrid-bilayer spectrum at 1061 cm^{-1} and 1126 cm^{-1} correspond to the antisymmetric and symmetric C-C stretching modes of the bilayer acyl chains, respectively, which increase in intensity as the C-C bonds adopt symmetric-trans conformation in the more ordered phospholipid gel-phase.[19-21,31,42-45] The broad peak observed at 1086 cm^{-1} is due to a superposition of the C-C stretching of the

acyl-chain gauche conformers and the phospholipid head group PO_2- stretching mode;[21,42-44,46] the area of this peak increases proportional to the number of gauche conformers and also broadens towards lower-energy as the acyl chains adopt a wider range of vibrational frequencies and greater conformational freedom in the liquid-crystalline phase.[20,43-45,47] Comparing the Raman spectrum of the hybrid bilayer to that of the DMPC vesicle, there are clear differences in the acyl-chain structure. The proportion of trans-to-gauche conformers as indicated by the ratio of the antisymmetric C-C intensities (I_{1061}/I_{1086}=1.73 for the hybrid bilayer and 1.62 for a vesicle bilayer) is greater for the hybrid bilayer; additionally, the out-of-phase C-C stretching mode is narrower in the Raman spectrum of the hybrid bilayer than the DMPC vesicle. These results indicate that interaction of the DMPC acyl chains with the underlying surface-bound C_{18} chains leads to less conformational freedom and more ordered acyl-chain structure than for a phospholipid vesicle bilayer.

4.3.3.2 Carbon-Hydrogen Twisting Region (1260-1340 cm^{-1}). The methyl-group carbon-hydrogen twisting region comprises of several modes including CH_2-rocking and CH_2-wagging modes. The most prominent feature is the CH_2-twisting mode at 1303 cm^{-1}.[42,44] It has been shown previously that the CH_2-twisting region is indicative of both acyl-chain order (gauch-to-trans ratio) as well as interchain coupling.[31,44] As the bilayer melts, the decrease in acyl-chain order allows for more freedom of motion about the carbon backbone due to greater gauche-to-trans ratio in the acyl chains. This increase in conformational and rotational freedom results in a range of vibrational energies, leading to broadening and asymmetry of the peak. The typical melting response is a shift in the CH_2-twisting mode to higher frequencies and broadening indicating decoupling of the acyl-

chain vibrations and greater disorder.[20,31,42] In the spectrum of the hybrid bilayer at room temperature, the CH_2-twisting modes appear less asymmetric, less broad, and at lower frequency than the same modes in the vesicle spectrum. This again implies greater acyl chain order and chain-to-chain coupling in the hybrid bilayer compared with a DMPC vesicle.

4.3.3.3 Carbon-Hydrogen Bending Region (1400-1500 cm^{-1}). The C-H bending region is indicative of lipid lattice order.[20,44] The broad band observed in this region is also a superposition of several Raman active vibrational modes, with the most intense bands due to scattering from the antiymmetric methyl bend (1436 cm^{-1}) and methylene scissoring mode (1455 cm^{-1}).[19,31,44,48] The ratio of the intensity of the antisymmetric methyl bend to the intensity of the methylene bend is indicative of chain decoupling and increasing gauche conformers where the resulting increased freedom-of-motion allows more CH_2 functional groups to undergo significant scissoring/bending vibrations.[44] In the Raman spectrum of the hybrid bilayer, the ratio of the methyl scissoring peak intensities is greater than observed in the DMPC vesicle bilayer (1.28 as compared to 1.19). This suggests greater interchain coupling in the gel-phase as compared with the DMPC vesicle, where the ratio of the two bands indicates the bilayer has begun to transition from the gel-phase into the melted phase. This result further indicates the hybrid bilayer is more structured and contains fewer gauche defects than the DMPC vesicle bilayer.

4.3.3.4 Carbon-Hydrogen Stretching Region (2800-3100 cm^{-1}). The carbon-hydrogen stretching region of the phospholipid Raman spectrum is the most complex but well-studied region. The broad band of overlapping peaks in this region consists of three main Raman modes: the CH_2-symmetric-stretching mode (2847 cm^{-1}), the CH_2-

antisymmetric-stretching mode (2883 cm^{-1}), and the CH_3-terminal-methyl-stretching mode (2930 cm^{-1}) which lie superimposed on a number of broad fermi-resonance bands.[19,31,33,43,44,46,49-53] The characteristics of these Raman bands can provide further insight into the acyl-chain structure, and have been characterized as follows: The ratio of the intensity of the CH_2-antisymmetric stretching mode to the CH_2-symmetric-stretching mode (I_{2883}/I_{2847}) provides an indicator of the acyl-chain lateral packing density.[6,22,31,44,52] During a phospholipid thermal phase transition, this ratio undergoes two significant changes: an initial, more subtle decrease which is due to increased rotational freedom in the acyl chains, followed by a larger more rapid decrease (as a function of temperature), which is indicative of increasing gauche conformers.[20] The ratio of the CH_3-terminal-methyl-stretching mode to the CH_2-symmetric-stretching mode (I_{2930}/I_{2847}) is indicative of both structural disorder in the acyl chains (gauch vs trans character) as well as acyl-chain lateral packing density and increases as the bilayer becomes disordered.[6,22,31,44,52] The change in this peak ratio as a function of temperature is the most commonly used spectral indicator of the lipid bilayer main-transition. Frequency shifts of the CH_2-antisymmetric- and symmetric-stretching mode also indicate the level of interchain coupling. Here, decreased interchain order results in decreased H-H interaction between chains and increases in the frequency of both modes of C-H stretching.

In the hybrid bilayer, the Raman spectrum in the C-H stretching region indicates greater order at the same temperature compared with the vesicle bilayer. The I_{2883}/I_{2847} ratio in the hybrid bilayer is (1.11) compared with (1.06) in the vesicle membrane suggesting a higher degree of interchain packing and fewer gauche defects. The I_{2930}/I_{2847} ratio is larger for the hybrid bilayer than the vesicle membrane (1.99 vs. 1.70), leading to the same

conclusion. In addition, the frequency of both the CH_2-symmetric stretch and the CH_2-antiymmetric stretch are higher in the hybrid bilayer, indicating greater coupling between neighboring hydrogen atoms in the acyl chains. To gain a better understanding of within-particle hybrid bilayers we also examine the formation and temperature-dependent structure of DMPC hybrid bilayers within individual chromatographic particles.

4.3.4 Confocal Raman Microscopy of Hybrid Supported Bilayer Formation within a C_{18}-functionalized Chromatographic Silica Particle

To investigate hybrid-bilayer formation, phospholipid and surface-bound C_{18}-acyl chain structures were monitored *in situ* as a function of time as lipid was adsorbed to the C_{18}-interface from solution within an individual porous-silica particle (Figure 4.3). This was accomplished by injecting a dispersion of C_{18} particles prewetted in methanol into a microscopy flow cell and allowing particles to settle and adhere to the surface. The Raman probe volume was translated into the center of an individual particle and the exterior solution switched to 15% v/v isopropanol/water. Raman scattering was collected as a function of time as the solution was switched to 15% v/v isopropanol/water containing 5 mg/mL DMPC. Once the spectra were no longer changing (indicating equilibrium DMPC surface coverage), the solution was switched to pure water.

Examining Raman reporter bands indicative of acyl-chain structure ((C-C stretching (1030-1150 cm^{-1}), C-H bending (1400-1500 cm^{-1}), CH_2 twisting (1260-1340 cm^{-1}), and C-H stretching (2800-3100 cm^{-1})), increases in bands associated with disordered acyl chains such as the broad C-C stretching mode at 1086 cm^{-1}, and the broad CH_2-twisting

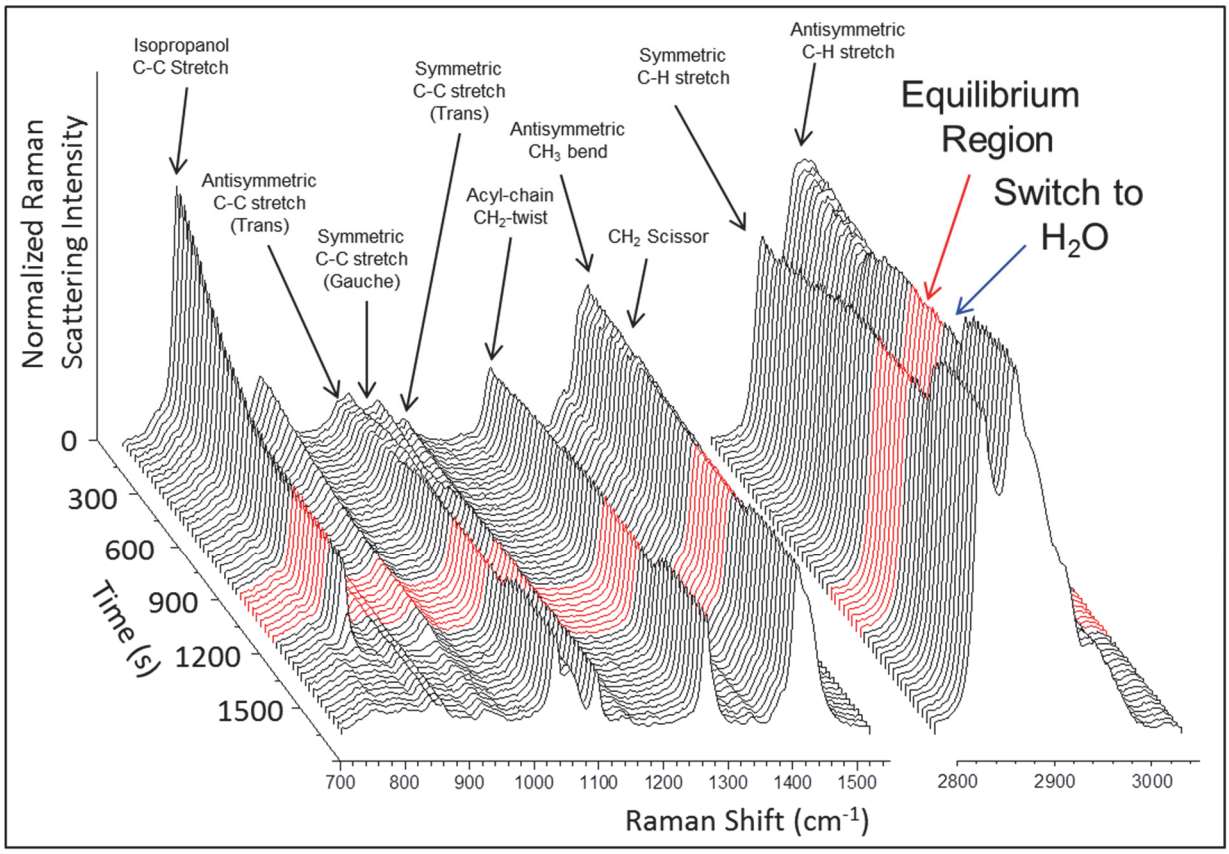

Figure 4.3: Raman spectra collected *in situ* within an individual C_{18}-silica particle as DMPC is adsorbed from solution to the C_{18}-surface. The red region is the equilibrium region where the overlapping portions of the SMCR analysis were carried out.

mode at 1303 cm^{-1} are observed, along with the headgroup CN-stretching mode at 715 cm^{-1}, confirming phospholipid adsorption. Nearly midway through the adsorption process, indicators of acyl-chain ordering begin to appear, most notably the trans-conformer C-C stretching modes at 1061 cm^{-1} and 1126 cm^{-1}, suggesting hybrid-bilayer ordering as the lipid coverage increases. An additional increase in ordering is observed as the solution is switched from isopropanol/water to pure water.

To examine these complex spectra where many peaks overlap and a model for the spectral changes as a function of time is unknown, we use a multivariate statistical approach, self-modeling curve resolution (SMCR).[54] SMCR is a well-established technique that allows resolution of correlated (even overlapped) spectral changes without *a priori* knowledge of a physical model of the process.[34] The details of SMCR have been published previously.[20,34,54-56] Briefly, spectra collected as a function of temperature are organized into a w by t data matrix **D** where each row (w) corresponds to the measured Raman scattering intensity at a given wavenumber and each column (t) corresponds to the temperature at which the spectrum was collected. Thus, a full spectrum at a given temperature is contained in each column of **D**. Under the assumption that each spectrum in **D** can be represented by a linear combination of component spectra (where each component is representative of a structural domain of the bilayer), the data matrix, **D**, is represented by $\mathbf{D} = \mathbf{AC}$, the product of a w by n component spectra matrix, **A**, and **C**, an n by c matrix of component concentrations (c) where rows correspond to the relative contribution of component (n) to the overall spectrum at each temperature. When an explicit mathematical model of the composition changes or the component spectra are unknown, SMCR provides an approach to elucidate these values by examining correlation in the data.

SMCR begins with principle components analysis (PCA),[34] where the spectral data are decomposed into a matrix of orthonormal eigenvectors (**Q**) and respective scores (**λ**). The eigenvectors in (**Q**) correspond to the correlated changes in the spectral data and the diagonal elements of the scores matrix (**λ**) indicate the relative magnitude of the contribution of each eigenvector to the spectral data. By a statistical test of the scores and the shape of the eigenvectors both visually and statistically,[34] **Q** can be truncated a matrix of vectors (principle components) ($\widehat{\mathbf{Q}}$) which capture the meaningful correlation in the data while rejecting uncorrelated noise. The spectral data are then projected onto the composition eigenvectors ($\widehat{\mathbf{Q}}$) to obtain a matrix of (eigenvector) principle-component spectra ($\mathbf{U} = \mathbf{D}\widehat{\mathbf{Q}}$), which correspond to the correlated changes in **Q**. Both sets of abstract eigenvectors are then rotated from eigenvector space into real space by a rotation matrix **K** that produces matrices **A** ($\mathbf{A} = \mathbf{U}\mathbf{K}^{-1}$) and **C** ($\mathbf{C} = \mathbf{K}\widehat{\mathbf{Q}}^{T}$), which are real component spectra and concentration vectors, respectively. The data, **D**, can then be represented by the product of **A** and **C** ($\mathbf{D} = \mathbf{A}\mathbf{C} = \mathbf{U}\mathbf{K}^{-1}\mathbf{K}\widehat{\mathbf{Q}}^{T}$).

In this work, SMCR analysis is used to examine spectral changes occurring during phospholipid adsorption. To reduce contributions of spectral noise in the SMCR analysis, spectra were truncated to regions where structurally informative spectral changes occur. PCA indicated that there were four significant components. Because resolution of four components by SMCR is extremely challenging, the spectra were divided into two overlapping segments: A three-component segment corresponding to the adsorption of the phospholipid from isopropanol and a two component segment corresponding to the switch from isopropanol/water/DMPC to pure water. After completing the curve resolution step, the spectra in the overlapping isopropanol region were confirmed to be equivalent, and four

component spectra were selected (Figure 4.4A) and used in a matrix least-squares step to determine the concentration vectors ($[\mathbf{A}^T\mathbf{A}]^{-1}\mathbf{A}^T\mathbf{D} = \mathbf{C}$) corresponding to the component spectra presented in Figure 4.4B.

The four-component (three-step) adsorption process proceeds as follows:

Disordered phospholipid is initially adsorbed to the C_{18} surface. In the spectral data (Figure 4.3) displacement of isopropanol by the accumulation of phospholipid is indicated by a decrease in intensity of the isopropanol C-C stretching mode[57] (816 cm^{-1}). In the component spectrum, the appearance of disordered phospholipid is indicated by the appearance of the CN stretching mode from the phospholipid head group (715 cm^{-1}) and increase in the broad C-C stretching mode at 1086 cm^{-1} as well as the CH_2-twisting mode at 1303 cm^{-1}. Indicators of an increase in disordered acyl-chains are the less well resolved C-C bending modes at 1436 cm^{-1} and 1455 cm^{-1}. In the C-H stretching region, the broad band at 2853 cm^{-1} also increases; this band is associated with splitting of the CH_2 symmetric-stretching mode and also a strong Fermi resonance between the terminal methyl-group and the symmetric-methylene-stretching mode,[49,51,58] associated with gauche defects. The 2900 cm^{-1} band which is due to the sum of the broad CH-symmetric stretching mode (at 2890 cm^{-1} when acyl chains contain a large fraction of gauche defects[31]) and the Fermi resonance due to the asymmetric CH-bending mode and the symmetric CH_3-stretching mode (2910 cm^{-1}),[49,53] also increases as more freedom in the acyl chains allows interaction between terminal methyl groups and nearby methylene stretching modes.

Interestingly, the initial component spectrum corresponding to the surface-bound C_{18}-chains does not entirely disappear during the first adsorption step (Figure 4.4B), nor does the component corresponding to adsorption of gauche conformers grow to a relative

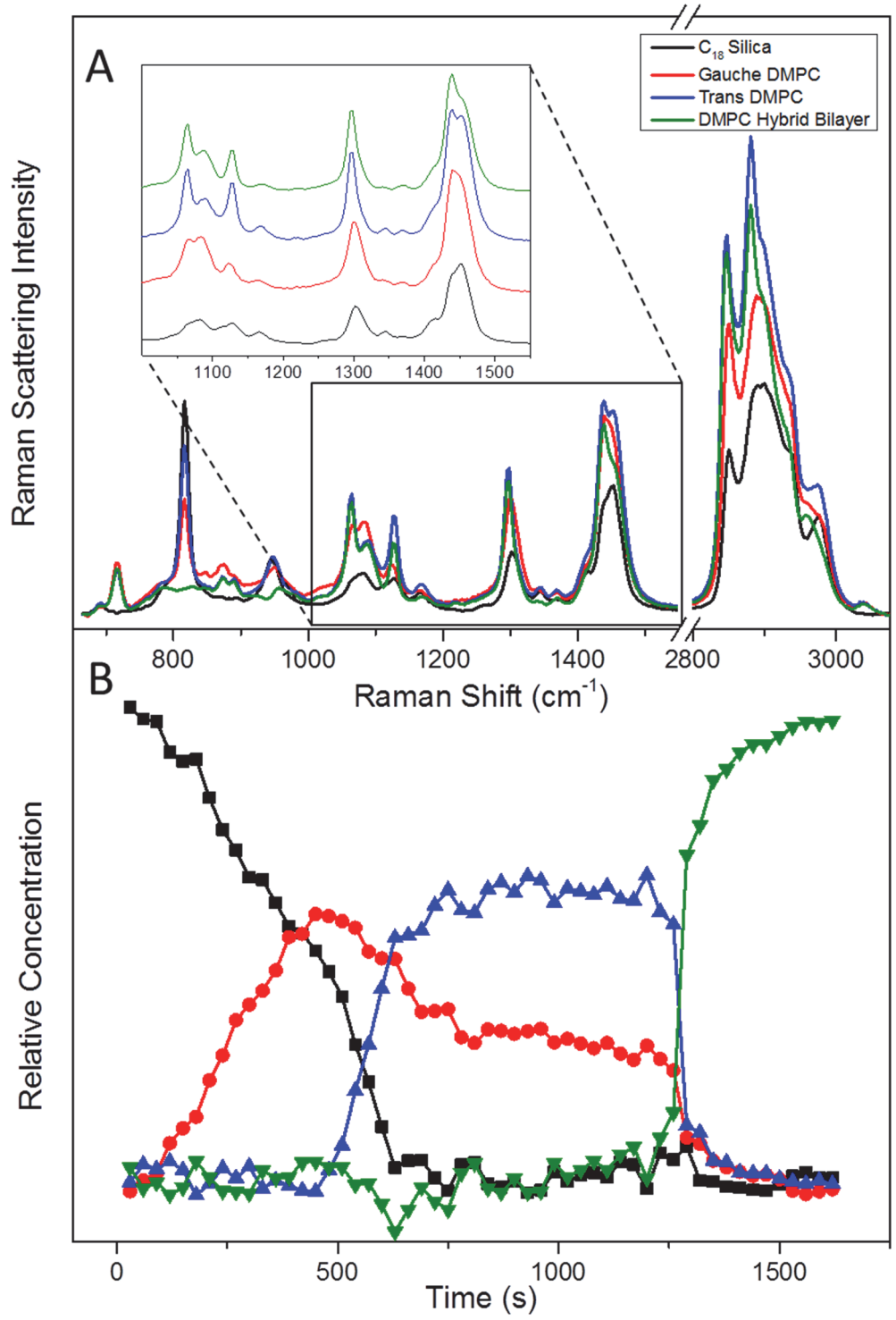

Figure 4.4: Self-modeling curve resolution analysis of hybrid-bilayer formation. A. Component spectra corresponding to the C_{18}-silica prior to adsorption (Blue), the initial adsorption of DMPC where the acyl chains contain a large portion of gauche conformers (Red), the second adsorption step where the DMPC acyl chains adopt mostly trans conformation (Blue) and the final component corresponding to the within–particle hybrid bilayer in water (Green). B. Relative concentration vectors showing the proportion of each component in time as adsorption of DMPC occurs.

composition of unity. Instead, a second step occurs where continued adsorption of phospholipid results in acyl-chain ordering. Displacement of isopropanol continues as a decrease in its relative contribution until it disappears at ~750 s. At 750 s the growth of the CN-stretching mode rolls over indicating no further lipid accumulation, and the spectra are no longer changing in time, indicating adsorption equilibrium. In this region, the sum of the relative contributions of the trans and gauche spectra add to unity, indicating the sum of these two components completely describes the system at equilibrium.

In the trans component spectrum, acyl-chain ordering is evidenced by the appearance of the trans-associated C-C stretching modes at 1061 cm^{-1} and 1126 cm^{-1}, the shift to lower wavenumber (1298 cm^{-1}) of the CH_2-twisting mode and the overlap of the CH-bending modes. Additionally, in the CH-stretching region, the CH-symmetric stretching mode at 2847 cm^{-1} and the CH_2-antisymmetric-stretching mode at 2883 cm^{-1}, which are both sensitive to acyl-chain packing due to interchain vibrational coupling, indicate a gel-phase bilayer with a majority of trans-conformers.

At 1260 s, after the within-particle spectra of the hybrid bilayer in the isopropanol/water/DMPC solution were stable, the exterior solution was switched from isopropanol/water/DMPC to pure water. Further acyl-chain ordering is observed accompanying elimination of isopropanol. This is not surprising, as the disordering effects of alcohols on membranes are well-known.[59,60] It has been shown that association of ethanol with the glycerol moiety in the phospholipid headgroup and interaction with upper-acyl-chain methylene groups likely leads to disordering;[60] a similar interaction likely occurs with isopropanol at the hybrid-bilayer membrane. Thus, removal of isopropanol results in further chain ordering.

4.3.5 Temperature-dependent Raman Spectroscopy and Differential Scanning Calorimetry to Investigate the Structure of Within-particle Hybrid-bilayer Membranes

Phospholipid bilayer membranes are well-known to exhibit temperature-dependent structural changes which can affect small molecule and protein partitioning.[61,62] Because the structure of the within-particle hybrid bilayer is clearly different than a vesicle bilayer of the same phospholipid at room temperature, a temperature-dependent study of the within-particle bilayer was conducted by placing DMPC hybrid-bilayer-containing particles in a temperature-controlled microscopy cell[35] and collecting Raman spectra of the within-particle hybrid bilayer as a function of temperature (Figure 4.5).

PCA of the temperature-dependent Raman spectra of within-particle hybrid bilayers indicated two significant (principle-component) eigenvectors. Following SMCR, it was determined that the two components represent the gel- and fluid-phases of the bilayer, respectively. The component spectra and respective concentration vectors are presented in Figure 4.6A and 4.6B. Here the gel- and fluid-bilayer spectra have characteristics expected for lipid bilayer melting, resulting in acyl-chain disordering as temperature is increased.[20,35]

In the C-C region of the spectrum, the peaks at 1061 cm^{-1} and 1126 cm^{-1} corresponding to the in-phase and out-of-phase C-C stretching modes of the bilayer acyl chains are present as intense narrow bands in the gel-phase spectrum, indicating a majority of symmetric-trans conformers in the acyl chains; these peaks are lost at high temperature in the more disordered fluid-phase spectrum. The superposition of the out-of-phase C-C

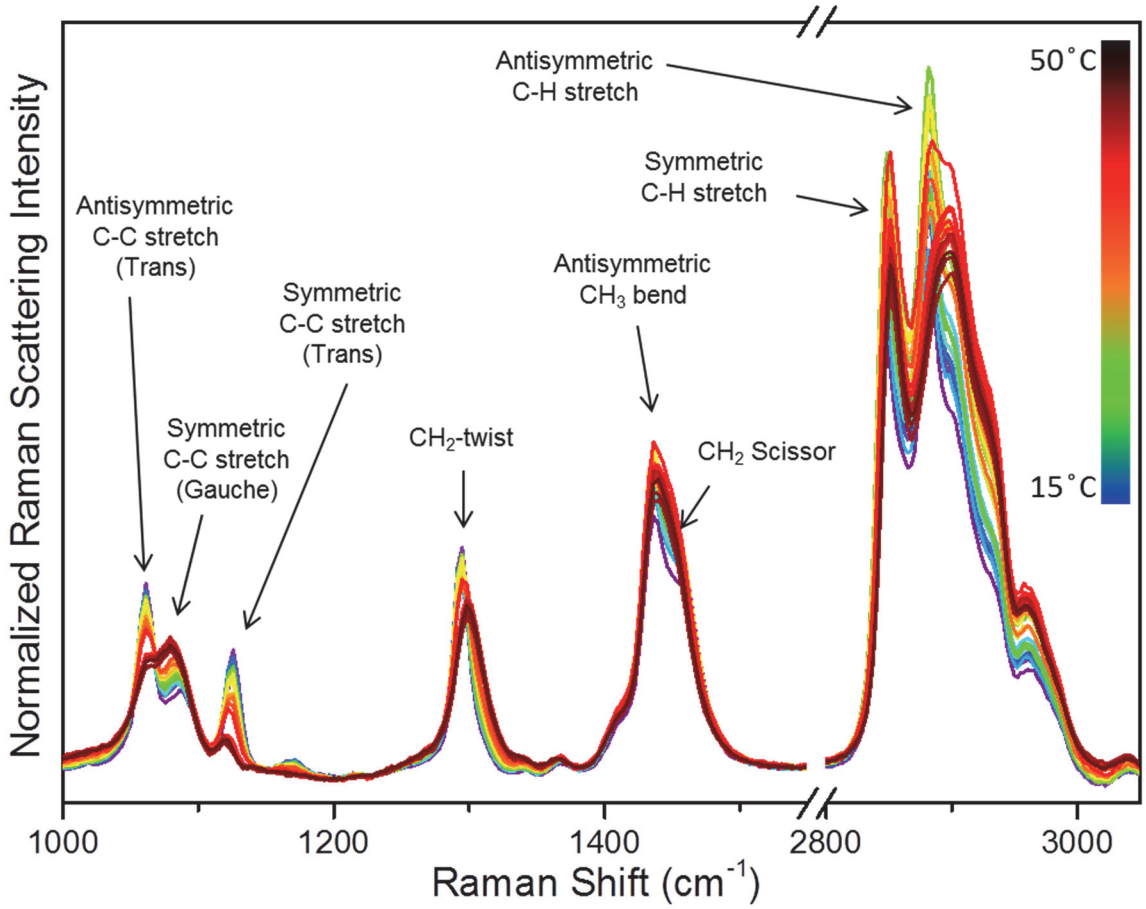

Figure 4.5: Raman spectra collected *in situ* as a function of temperature of the DMPC hybrid- bilayer melting transition.

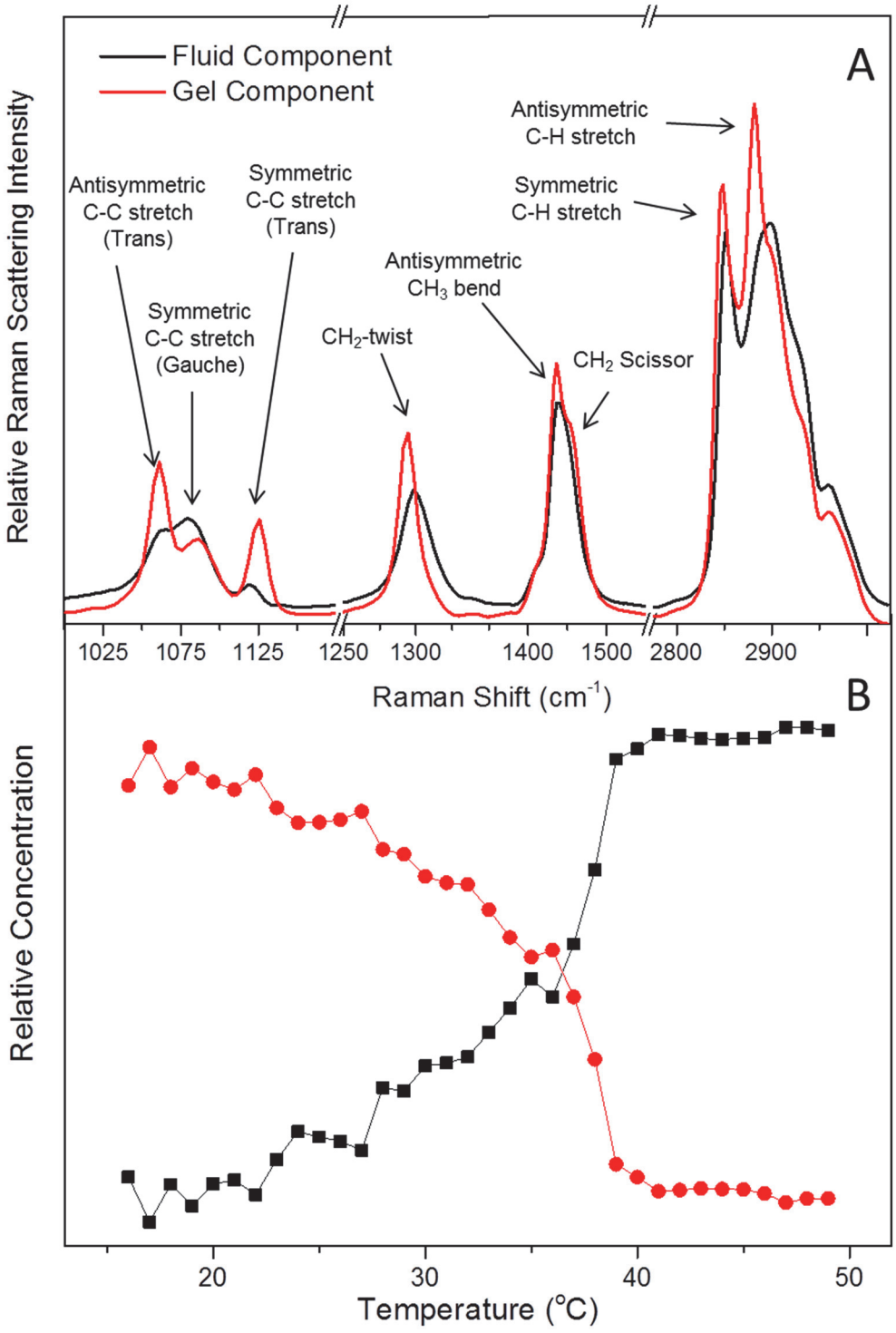

Figure 4.6: A. Component spectra resolved from the temperature-dependent Raman spectrum of the DMPC hybrid bilayer. The red spectrum corresponds to the gel-phase. The black spectrum corresponds to the melted-phase. B. Corresponding concentration vectors showing the change in relative concentration of each of the spectra in A as a function of temperature.

stretching of the acyl-chain gauche conformers with the phospholipid head group PO_2-stretching mode (the broad peak at 1086 cm^{-1}) shows increased intensity and is broadened toward lower frequency indicating an increase in the proportion of gauche conformers in the acyl chains at higher temperatures. In the carbon-hydrogen twisting region, the gel-phase spectrum shows a sharp peak at 1296 cm^{-1} which becomes broad and shifted to higher frequency (1306 cm^{-1}) in the fluid-phase. This indicates acyl-chain disordering as temperature is increased resulting from a greater gauche-to-trans C-C bond ratio and a decrease in interchain coupling in the fluid-phase. Similarly, in the C-H bending region, the ratio of the intensity of the antiymmetric methyl bend (1436 cm^{-1}) to the intensity of the methylene bend (1455 cm^{-1}) changes from 1.3 in the gel-phase spectrum to 1.2 in the melted-phase spectrum indicating chain decoupling, a change in lattice order, and increasing gauche conformers.

The spectra of the gel- and fluid-phases in the carbon-hydrogen stretching region are also indicative of chain disordering and similar to vesicle spectra over the main phase transition. The ratio of the intensity of the CH_2-antisymmetric-stretching mode to the CH_2-symmetric-stretching mode (I_{2883}/I_{2847}) changes from 1.2 in the gel-phase spectrum to 1.1 in the fluid-phase spectrum, indicating a decrease in the acyl-chain lateral packing density. The ratio of the CH_3-terminal-methyl-stretching mode to the CH_2-symmetric-stretching mode (I_{2930}/I_{2847}) changes from 0.47 to 0.69 demonstrating an increase in both structural disorder in the acyl chains (gauch vs trans character) and, again, a shift in the acyl-chain lateral packing density to less-dense in the fluid-phase. Frequency shifts of the CH_2-antisymmetric- and symmetric-stretching mode from 2848 cm^{-1} and 2881 cm^{-1}, respectively, in the gel-phase, to 2851 cm^{-1} and 2886 cm^{-1} in the fluid-phase indicate a

decrease in interchain coupling in the fluid hybrid bilayer, where decreased interchain order results in less hydrogen interactions between neighboring acyl chains and increases in the frequency of both modes of C-H stretching.

Although the spectral changes in transitioning from the gel-phase to the melted-phase are similar to those that occur across a DMPC vesicle phase transition, the temperature-dependence of the changes is much different. In a DMPC vesicle, the main phase transition occurs both spectroscopically (Raman) and calorimetrically (differential scanning calorimetry) at 24℃, is narrow (23℃ - 25℃).[35] The Raman spectra in this work, however, show changes across a broad temperature range from 20℃-40℃ (Figure 4.6B), suggesting the hybrid-bilayer phase transition is less cooperative than the transition in a vesicle bilayer.[28] Additionally, the phase transition temperature is shifted upwards to 40℃. These results suggest that the interaction between the upper leaflet of DMPC and the covalently-bound lower leaflet of C_{18} chains inhibit chain melting and lead to a more localized (less cooperative) phase transition.

To confirm the spectroscopic results, the melting transition of the within-particle DMPC hybrid bilayer was measured using differential scanning calorimetry (DSC, Figure 4.7). The resulting calorimetric transition curve is in good agreement with the spectroscopy in the broadness and location of the main-transition. Interestingly, the calorimetry shows a pretransition very near the DMPC vesicle phase transition. This transition has been observed previously in DSC endotherms of hybrid bilayers in macroporous silica and has been suggested due to phospholipid multilayers adsorbed to the hybrid bilayer, despite multiple washing steps.[63] Unfortunately, we were unable to resolve Raman spectral changes associated with this transition. One literature source suggests the possibility of

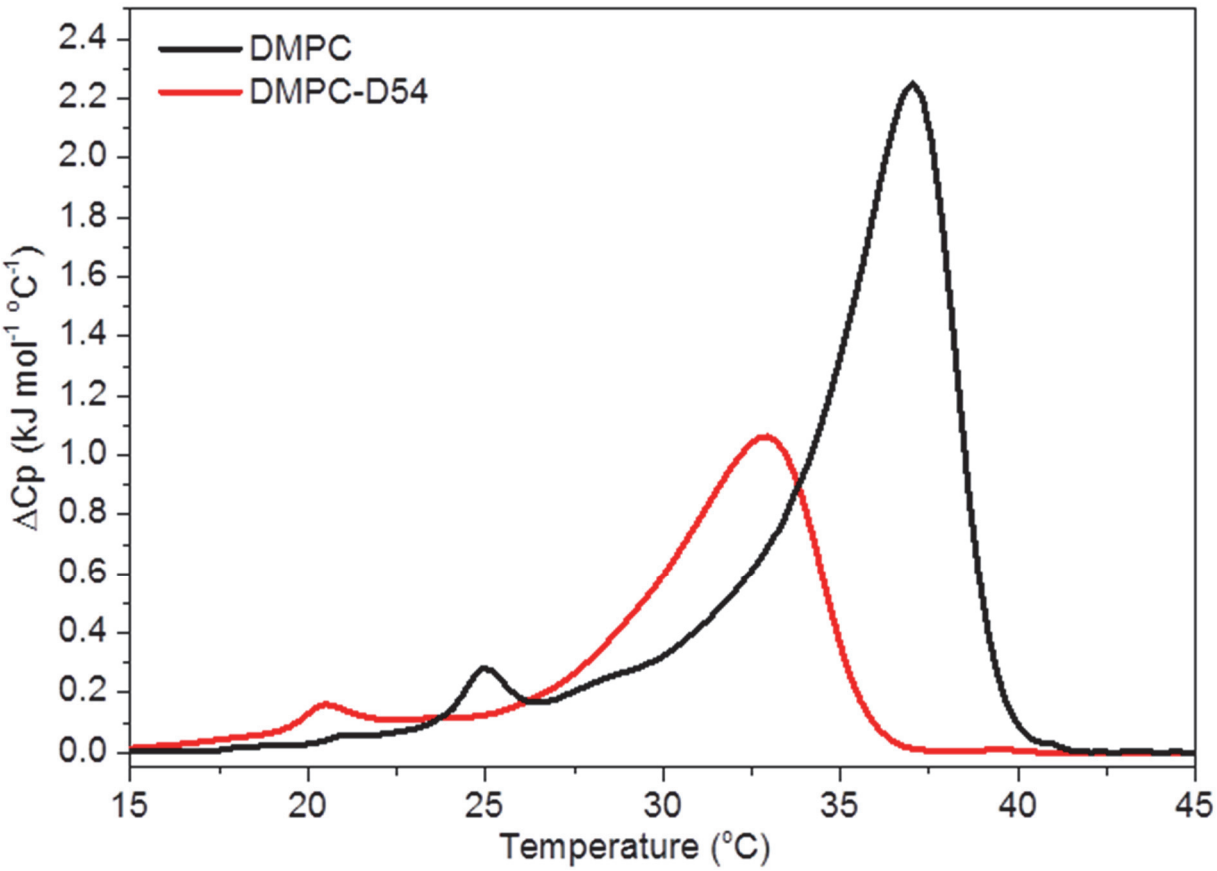

Figure 4.7: Calorimetric endotherms of the DMPC (Black) and DMPC-D54 (Red) phase-transitions.

lipid monolayers at 'defect' sites in the underlying C_{18} chains[64], while others have shown formation of supported lipid bilayers in the SiO_2 regions of substrates where both C_{18} and bare silica interfaces have been prepared in patterns.[65] It is plausible that the observed transition is due to these defects, and not multilayers, explaining the inability of additional wash-off steps to remove them.

The broadening and higher temperature of a DMPC hybrid-bilayer phase transition at the silica-C_{18} interface compared to a DMPC vesicle membrane has been reported previously in low-curvature macroporous-silica experiments[63] and similarly shifted, less-broad, transitions have been observed in sum-frequency generation experiments carried out at flat gold interfaces.[66] Using differential scanning calorimetry, Bayerl and coworkers discovered that the phase transitions of several phospholipids in C_{18} hybrid bilayers were shifted to higher temperatures and also had broad phase transitions compared with vesicles of the same lipid. By examining the acyl-chain-length dependence of the phase transition temperature, it was hypothesized that the acyl chains of the upper leaflet of phospholipid interdigitate with the lower leaflet of C_{18} leading to less cooperativity and higher-temperature transition because the acyl-chain structure is stabilized by interaction with the stationary C_{18} chains. To test this hypothesis, Bayerl and coworkers measured deuterium nuclear magnetic resonance (^{2}H-NMR) spectra of hybrid bilayers confirming hindered axial motions of selectively deuterated acyl chains providing evidence of interdigitation.[63] Similar results were observed at a planar substrate, where neutron reflection from a DMPC monolayer adsorbed to a C_{18} modified silica layer on a silicon support showed the DMPC acyl chains were interdigitated with the C_{18} chains on the silica surface.[64] These results are in contrast with those of Swanson et al. where infrared spectroscopy, x-ray scattering, and

ellipsometric experiments which support a noninterdigitated structure at a planar C_{18}-modified interface.[67] These results, however, come without calorimetric evidence of a broadened or higher-temperature phase transition. Interestingly, Bayerl and coworkers report that in unpublished infrared spectroscopic data the underlying C_{18}-chain structure is constant through the phase-transition.[63] These conflicting results motivate further investigation into the source of broadening and increase in temperature of the hybrid-bilayer phase transition.

4.3.6 Temperature-dependent Raman Spectroscopy of Within-particle Hybrid Bilayers with Deuterated Phospholipid Acyl Chains

To investigate the broadened, higher-temperature phase transition observed in the within-particle hybrid bilayers, and to gain a better understanding of the structure of the within-particle hybrid bilayer, Raman scattering from the phospholipid acyl chains was resolved from that of the surface C_{18} chains by using acyl-chain deuterated DMPC (1,2-dimyristoyl-d54-sn-glycero-3-phosphocholine, DMPC-D54). Raman spectra of the deuterated phospholipid hybrid bilayers within particles were collected as a function of temperature through the hybrid-bilayer phase transition (Figure 4.8), where changes in both the deuterated and nondeuterated acyl-chain structure are observed. Spectral changes occur, across a broad temperature range but the melting transition occurs at a lower temperature. This is anticipated, however, based on previous calorimetric studies where the deuterated lipid phase transitions in vesicles are shifted to lower temperature.[68] Due to the high degree of spectral overlap, the deuterated-phospholipid phase-transition spectral

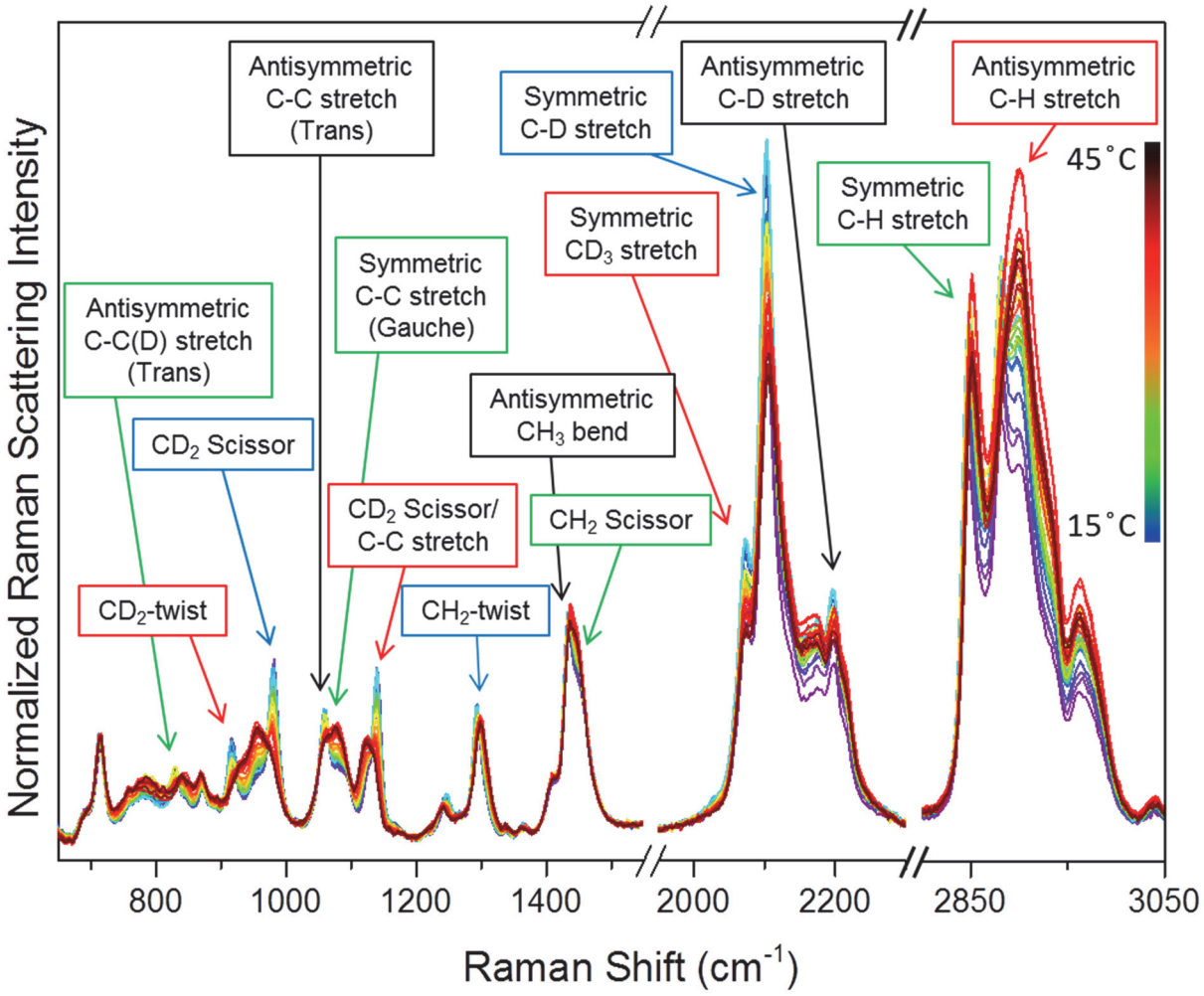

Figure 4.8: Raman spectra collected *in-situ* as a function of temperature of the DMPC-D54 hybrid-bilayer melting transition.

data were also analyzed using SMCR. PCA for the deuterated lipid yielded, similarly to the nondeuterated case, two principle components across the melting transition. The component spectra and concentration vectors from SMCR analysis are presented in Figure 4.9A and 4.9B. Here, structure changes observed in the Raman spectra, and the composition vectors describing the changes as a function of temperature, clearly demonstrate the phospholipid acyl chains and underlying C_{18}-chains undergo simultaneous disordering as the melting transition progresses. Spectral changes for the gel-phase and fluid-phase deuterated hybrid bilayer are discussed as follows. The lower wavenumber region of the deuterated-phospholipid hybrid bilayer (750 cm^{-1}- 1520 cm^{-1}) contains the deuterated and nondeuterated C-C stretching modes and the C-H and C-D bending, scissoring, and stretching modes. The spectral components are not shifted uniformly, thus, we will discuss all deuterated modes in this region with respect to the corresponding C-H modes.

4.3.6.1 Carbon-Carbon Stretching Region. The antisymmetric C-C stretching mode (1061 cm^{-1}) corresponding the surface-bound C_{18} acyl-chain trans C-C stretching decreases in intensity at high temperatures indicating loss of order in the C_{18} acyl-chain structure. Similarly, the antisymmetric C-C stretching mode of the deuterated phospholipid (shifted to 830 cm^{-1}) decreases in intensity with increased temperature indicating more gauche defects in the phospholipid acyl chains. The out-of-phase C-C modes for the deuterated and nondeuterated chains overlap to form the peak at 1139 cm^{-1}.[69] Here, both bands decrease simultaneously to a smaller broad peak. The C-C stretching mode due to the deuterated lipid has been shown to be more intense for both gel- and melted-phases,[69] explaining the intensity of the melted-phase peak in the deuterated hybrid bilayer, which

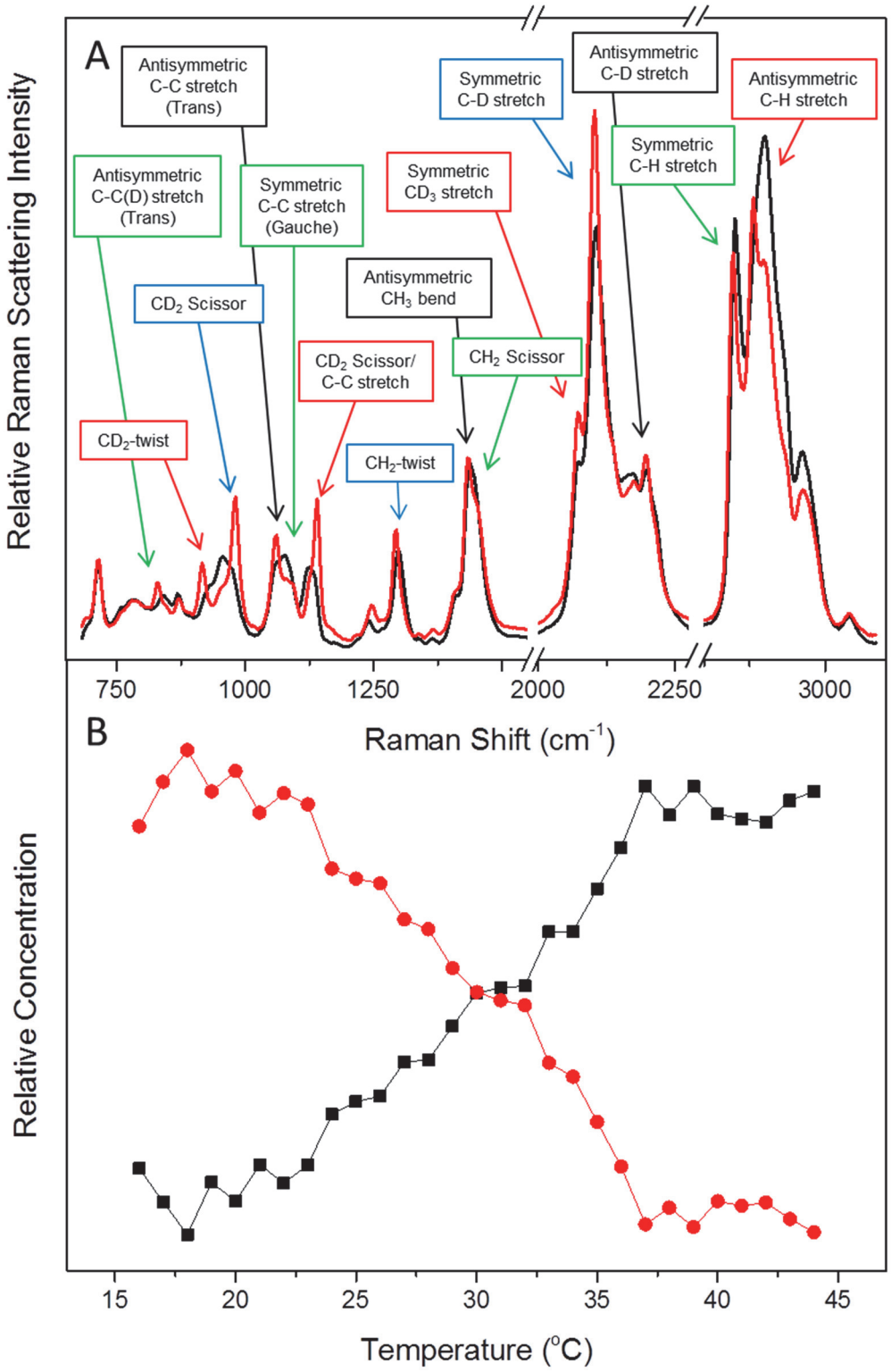

Figure 4.9: A. Component spectra resolved from the temperature-dependent Raman spectrum of the DMPC-D54 hybrid bilayer. The red spectrum corresponds to the gel-phase. The black spectrum corresponds to the melted-phase. B. Corresponding concentration vectors showing the change in relative concentration of each of the spectra in A as a function of temperature.

has greater amplitude in the melted-phase than in the nondeuterated case. The gauche, symmetric C-C stretching mode (1086 cm^{-1}) of the C_{18}-acyl chains also increases in intensity and broadens indicating disordering of the C_{18}-acyl chains. The equivalent mode in deuterated phospholipids has not been assigned.

4.3.6.2 Carbon-Hydrogen and Carbon-Deuterium Twisting. The CH_2-twisting mode from the C_{18}-acyl chains is decreased in intensity and broadened in the melted-phase spectrum compared with the gel-phase spectrum, consistent with decreased order in the C_{18}-chains as temperature is increased. Again, the CD_2-twisting mode has been shown to qualitatively undergo the same changes on melting, as is observed in the deuterated-phospholipid bilayer, where the frequency-shifted CD_2-twist (916 cm^{-1})[69] decreases in intensity and broadens indicating decreased acyl-chain ordering in the phospholipid acyl chains at raised temperatures.

4.3.6.3 Carbon-Hydrogen and Carbon-Deuterium Bending. The overlapping CH-bending and scissoring modes at 1436 cm^{-1} and 1455 cm^{-1}, respectively are not overlapping with deuterated modes, thus the ratio of the peaks is a valid indicator of C_{18} structure. Here, I_{1436}/I_{1455} changes from 1.36 in the gel-phase spectrum to 1.30 in the fluid-phase spectrum consistent with increasing gauche conformers. The CD-bending and scissoring modes in the deuterated acyl chains do not overlap, and additionally, analogous changes in the CD-scissoring mode are not expected due to the lack of an infrared Fermi resonance that leads to this behavior in the CH spectrum (see Gaber et. al.)[69] The CD-scissoring mode (981 cm^{-1}) instead decreases in intensity and shifts to lower frequency as a function of increased temperature indicating melted acyl chains.[69] The behavior of the CD scissoring mode is consistent with this result.

4.3.6.4 Carbon-Deuterium Stretching Region. Unlike the low-to-mid wavenumber region where many deuterated and nondeuterated acyl-chain Raman bands overlap, the C-H and C-D stretching regions of the spectrum are entirely resolved. The C-D stretching modes occur in the region from 2000 cm^{-1} to 2250 cm^{-1}, and the C-H stretching modes in the region from 2800 cm^{-1} to 3100 cm^{-1}.[31,69] In the C-D stretching region, several changes indicative of acyl-chain disordering at higher temperature are observed. The most obvious change occurs in the CD_2-symmetric-stretching band (2101 cm^{-1}), where the decrease in intensity and shift to higher frequency (2106 cm^{-1}) as temperature is raised are indicative of decreased coupling between the acyl chains and an increase in gauche defects; this is analogous to the C-H symmetric stretch, where decreased coupling results in less damping, higher frequency, and lower polarizability vibrations.[31,69] The CD_3-symmetric stretching mode at 2073 cm^{-1} decreases as the bilayer acyl chains decouple, similar to the nondeuterated case as does the antisymmetric C-D stretching mode at 2195 cm^{-1}, while the CD_2-symmetric stretch increases slightly as shown by Gaber.[69] These results all confirm decoupling and disordering of the CD tails of the phospholipid at higher temperature.

4.3.6.5 Carbon-Hydrogen Stretching Region. The C-H stretching region of the Raman spectrum is particularly sensitive to acyl-chain packing and interchain vibrational coupling, also, many modes lie superimposed on broad fermi-resonances. These characteristics make this region valuable for characterizing the asymmetric bilayer in this work. The lowest wavenumber peak at 2847 cm^{-1} which is attributed to the CH_2-symmetric stretching mode is interestingly less intense in the low-temperature spectrum than expected for an all-trans gel-phase bilayer. Previous work has shown that increased intensity at low temperatures of the narrow CH_2-symmetric stretching mode is due to increased interchain-

interaction resulting in vibrational coupling of adjacent CH_2-symmetric stretching modes.[31,50,70] The absence of the intense CH_2-symmetric stretching mode despite all-trans configuration of the corresponding acyl chains suggests that despite having structural character of a close-packed layer, the methylene C-H vibrations of the C_{18}-acyl chains are not coupled due to their lack of close contact. We attribute this to an interdigitated gel-phase, where the deuterated acyl chains (which do not vibrationally couple with the protonated chains) pack between the surface-bound acyl chains preventing vibrational coupling at low temperatures.

In the high-temperature spectrum, the CH_2-symmetric stretch is slightly increased in intensity and shifted to 2853 cm^{-1} typical of melting of phospholipid acyl chains and indicating adoption of triclinic crystal structure typical of liquid-crystalline phases. The 2853 cm^{-1} mode is attributed to splitting of the CH_2 symmetric stretching mode and also a strong Fermi resonance between the terminal methyl-group and the symmetric methylene stretching mode.[50-52] The increase, then, is likely due to decreased acyl-chain mobility in the melted phase where the bilayer acyl chains can adopt configurations where terminal methyl groups on the protonated chains are more likely to couple with methylene symmetric stretching modes on neighboring protonated acyl chains. This indicates increased gauche conformers and increased methyl-to-methylene C-H coupling.

The prominent peak at 2881 cm^{-1} in the low-temperature spectrum has been attributed to the headgroup methylene stretching mode in the deuterated phospholipid[69] which lies superimposed on the CH_2 antisymmetric stretching mode at 2883 cm^{-1},[49,53] both of which have been shown to decrease with increased gauche defects as is seen in the high temperature spectrum. The broad peak which grows in at 2900 cm^{-1} is due to the sum of

the decreased broadened 2883 cm^{-1} band and the Fermi resonance due to the asymmetric CH-bending mode and the symmetric CH_3-stretching mode.[49,53] The increase in this band is, then, again indicative of decreased order in the bilayer acyl chains, where an increase in gauche defects again results in greater likelihood of vibrational interaction between terminal methyl groups and protonated acyl chains.

The temperature-dependent concentration profiles determined using SMCR (Figure 4.9B) show two distinct components which on examination of the corresponding spectra (Figure 4.9A) represent the gel-phase and fluid-phase, which change simultaneously as a function of temperature. Similarly to the protonated lipid bilayer the phase transition temperature predicted using spectroscopy is shifted from that of DMPC-D54 vesicles and is quite broad. Therefore, to confirm the spectroscopic result, the melting transition of the within-particle DMPC-D54 hybrid bilayer was measured using DSC (Figure 4.7) following the protocol previously described for protonated lipid. The resulting calorimetric transition curve is again in good agreement with the spectroscopic result in broadness and location of the main-transition. Interestingly, the calorimetry again shows a low-temperature transition which we are unable to resolve in Raman spectral changes. This pre-transition is near the DMPC-D54 vesicle melting transition[68] and may be attributable to DMPC-D54 bilayers formed at defects in the C_{18} layer on the silica.

The results of Raman spectral analysis and calorimetry of the deuterated-phospholipid hybrid bilayer are informative of the bilayer structure. The bands indicative of acyl-chain trans character in all regions of the spectrum show that both the deuterated and nondeuterated acyl chains are in all-trans-conformation at low temperatures and have a much greater portion of gauche defects at high temperature. The C-H stretching region

indicates a lack of vibrational coupling despite the all-trans acyl-chain character and other indicators of hexagonal packing in the gel-phase. The spectroscopic "concentration" vectors and calorimetric endotherms are in good agreement, showing that the structural changes associated with melting in the deuterated acyl chains and the surface C_{18} chains occur together as the temperature is raised.

These results suggest a fully interdigitated gel-phase bilayer where the deuterated and nondeuterated acyl-chain structures are mixed which explains the increase in temperature and broadening of the hybrid-bilayer phase transitions. This is in contrast with the infrared and ellipsometric measurements made at a planar, oxidized silicon-C_{18} interface, which show a structurally decoupled, noninterdigitated layer of DPPC at the C_{18} interface.[67] We hypothesize these structural differences are due to the surface density of alkyl chains at the planar silica interface where polymeric self-assembled monolayer films have greater acyl-chain packing density preventing interdigitation. In the current work, chromatographic silica particles were monofunctionally derivitized, limiting the maximum C_{18} coverage to the free surface silanols on the silica support. Here, the sparsity of C_{18}-chains on the surface (~2.4 C_{18}-chains/nm^2) provides space where the phospholipid acyl chains can form an interdigitated structure between the surface-bound acyl chains.

4.4 Conclusions

In this work, the formation and temperature-dependent structure of hybrid-bilayer membranes formed at the C_{18}-surface within porous chromatographic silica particles was investigated using confocal Raman microscopy. To explore hybrid-bilayer formation, DMPC adsorption was monitored as a function of time from 15% isopropanol. Self-

modeling curve resolution (SMCR) analysis of the spectra indicated a three-step, four-component process where disordered phospholipid is initially adsorbed to the C_{18} surface, followed by an ordering step where phospholipid and C_{18} acyl chains adopt trans conformations with increasing lipid coverage. As the solution is switched from isopropanol-water to pure water, further acyl-chain ordering is observed accompanying the loss of isopropanol, likely due to the dissociation of isopropanol from the lipid head-group and upper-acyl-chain region. DMPC surface coverage (3.78±0.08 μmol/m^2) was quantified by carbon analysis and the corresponding phospholipid cross-sectional area (43.9±0.9 $Å^2$) is in close agreement with inner-leaflet cross-sections in vesicles. By monitoring acyl-chain conformation versus temperature, it was possible to observe the hybrid-bilayer main phase transition which is broad and shifted to higher temperature than a DMPC vesicle, in agreement with differential scanning calorimetry (DSC) results. To understand the nature of hybrid-bilayer melting, Raman scattering from lipid acyl chains was resolved from C_{18}-chains through the use of deuterated DMPC. Raman and DSC measurements indicate that hybrid bilayers within C_{18} chromatographic particles are interdigitated and the immobility of C_{18}-chains likely leads to the shift to higher temperature and broadening of hybrid-bilayer thermal phase transitions.

4.5 References

(1) Liu, X.; Testa, B.; Fahr, A. *Pharm. Res.* **2011**, *28*, 962-977.

(2) Seydel, J. K.; Coats, E. A.; Cordes, H. P.; Wiese, M. *Archiv. Pharm.* **1994**, *327*, 601-610.

(3) Pignatello, R.; Musumeci, T.; Basile, L.; Carbone, C.; Puglisi, G. *J. Pharm.Bioall. Sci.* **2011**, *3*, 4-14.

(4) Beigi, F.; Gottschalk, I.; Lagerquist Hägglund, C.; Haneskog, L.; Brekkan, E.; Zhang, Y.; Österberg, T.; Lundahl, P. *Int. J. Pharm.* **1998**, *164*, 129-137.

(5) Litman, G. W.; Litman, R. T.; Henry, C. J. *Cancer Res.* **1976**, *36*, 438-444.

(6) Weissmann, G.; Troll, W.; van Duuren, B. L.; Sessa, G. *Biochem.Pharmacol.* **1968**, *17*, 2421-2434.

(7) Snart, R. S. *Biochim. Biophys. Acta (BBA)* **1967**, *144*, 10-17.

(8) Plant, A. L. *Langmuir* **1999**, *15*, 5128-5135.

(9) Plant, A. L. *Langmuir* **1993**, *9*, 2764-2767.

(10) Meuse, C. W.; Krueger, S.; Majkrzak, C. F.; Dura, J. A.; Fu, J.; Connor, J. T.; Plant, A. L. *Biophys. J.* **1998**, *74*, 1388-1398.

(11) Hong, G.; Guoan, L.; Jun, F.; Ottova, A. L.; TIEN, H. T. *Acta Chim. Sinica* **2001**, *59*, 220-223.

(12) Millo, D.; Bonifacio, A.; Moncelli, M. R.; Sergo, V.; Gooijer, C.; van der Zwan, G. *Colloids Surf. B* **2010**, *81*, 212-216.

(13) Kundu, J.; Levin, C. S.; Halas, N. J. *Nanoscale* **2009**, *1*, 114-117.

(14) Plant, A. L.; Brighamburke, M.; Petrella, E. C.; Oshannessy, D. J. *Anal. Biochem.* **1995**, *226*, 342-348.

(15) Mozsolits, H.; Wirth, H.-J.; Werkmeister, J.; Aguilar, M.-I. *Biochim. Biophys. Acta* **2001**, *1512*, 64-76.

(16) Krause, E.; Dathe, M.; Wieprecht, T.; Bienert, M. *J. of Chromatogr. A* **1999**, *849*, 125-133.

(17) Ollila, F.; Halling, K.; Vuorela, P.; Vuorela, H.; Slotte, J. P. *Arch. Biochem. Biophys.* **2002**, *399*, 103-108.

(18) Tsirkin, I.; Grushka, E. *J. Chromatogr. A* **2001**, *919*, 245-254.

(19) Wallach, D. F.; Verma, S. P.; Fookson, J. *Biochim. Biophys. Acta* **1979**, *559*, 153-208.

(20) Fox, C. B.; Uibel, R. H.; Harris, J. M. *J. Phys. Chem. B* **2007**, *111*, 11428-11436.

(21) Schultz, Z. D.; Levin, I. W. *Annu. Rev. Anal. Chem.* **2011**, *4*, 343-366.

(22) Fox, C. B.; Myers, G. A.; Harris, J. M. *Appl. Spectrosc.* **2007**, *61*, 465-469.

(23) Gasser-Ramirez, J. L.; Harris, J. M. *Anal. Chem.* **2010**, *82*, 5743-5750.

(24) Gasser-Ramirez, J. L.; Harris, J. M. *Anal. Chem.* **2009**, *81*, 2869-2876.

(25) Gasser-Ramirez, J. L.; Harris, J. M. *Anal. Chem.* **2009**, *81*, 7632-7638.

(26) Kitt, J. P.; Harris, J. M. *Anal. Chem.* **2014**, *86*, 1719-1725.

(27) Houlne, M. P.; Sjostrom, C. M.; Uibel, R. H.; Kleimeyer, J. A.; Harris, J. M. *Anal. Chem.* **2002**, *74*, 4311-4319.

(28) Sturtevant, J. M. *Annu. Rev. Phys. Chem.* **1987**, *38*, 463-488.

(29) Mie, G. *Ann. Phys.* **1908**, *330*, 377-445.

(30) Kitt, J. P.; Harris, J. M. *Anal. Chem.* **2015**, *87*, 5340-5347.

(31) Wong, P. T. T. *Annu. Rev. Biophys. Bioeng.* **1984**, *13*, 1-24.

(32) Kyrikou, I.; Hadjikakou, S. K.; Kovala-Demertzi, D.; Viras, K.; Mavromoustakos, T. *Chem. Phys. Lipids* **2004**, *132*, 157-169.

(33) Levin, I. *Adv. Infrared Raman Spectrosc.* **1984**, *11*, 1-48.

(34) Malinowski, E. R. *J. Chemometrics* **1991**, *5*, 545-545.

(35) Kitt, J. P.; Bryce, D. A.; Harris, J. M. *Appl. Spectrosc.* **2015**, *69*, 513-517.

(36) Cherney, D. P.; Conboy, J. C.; Harris, J. M. *Anal. Chem.* **2003**, *75*, 6621-6628.

(37) Cherney, D. P.; Bridges, T. E.; Harris, J. M. *Anal. Chem.* **2004**, *76*, 4920-4928.

(38) Williams, K. P. J.; Pitt, G. D.; Batchelder, D. N.; Kip, B. J. *Appl. Spectrosc.* **1994**, *48*, 232-235.

(39) Akutsu, H. *Biochem.* **1981**, *20*, 7359-7366.

(40) Tristram-Nagle, S.; Liu, Y.; Legleiter, J.; Nagle, J. F. *Biophys. J.* **2002**, *83*, 3324-3335.

(41) Wiener, M.; Suter, R.; Nagle, J. *Biophys. J.* **1989**, *55*, 315-325.

(42) Lippert, J.; Peticolas, W. *Biochim. Biophys. Acta (BBA)-Biomembranes* **1972**, *282*, 8-17.

(43) Grell, E. *Membrane Spectrosc.* Springer: Berlin, Germany, 1981, pp 377-436.

(44) Orendorff, C. J.; Ducey, M. W.; Pemberton, J. E. *J. Phys. Chem. A* **2002**, *106*, 6991-6998.

(45) Levin, I. W.; Bush, S. F. *Biochim. Biophys. Acta* **1981**, *640*, 760-766.

(46) Spiker, R. C.; Levin, I. W. *Biochim. Biophys. Acta* **1975**, *388*, 361-373.

(47) Gaber, B. P.; Yager, P.; Peticolas, W. L. *Biophys. J.* **1978**, *21*, 161-176.

(48) Yellin, N.; Levin, I. W. *Biochem.* **1977**, *16*, 642-647.

(49) Hill, I. R.; Levin, I. W. *J. Chem. Phys.* **1979**, *70*, 842-851.

(50) Snyder, R.; Hsu, S.; Krimm, S. *Spectrochim. Acta A* **1978**, *34*, 395-406.

(51) MacPhail, R.; Strauss, H.; Snyder, R.; Elliger, C. *J. Phys. Chem.* **1984**, *88*, 334-341.

(52) Snyder, R.; Strauss, H.; Elliger, C. *J. Phys. Chem.* **1982**, *86*, 5145-5150.

(53) Cirak, J.; Horvath, L. *Chem. Phys. Lipids* **1988**, *49*, 197-204.

(54) Lawton, W. H.; Sylvestre, E. A. *Technometrics* **1971**, *13*, 617-633.

(55) Malinowski, E. R.; Cox, R. A.; Haldna, U. L. *Anal. Chem.* **1984**, *56*, 778-781.

(56) Zhao, Z.; Malinowski, E. R. *Anal. Chem.* **1999**, *71*, 602-608.

(57) Green, J. *J. Chem. Soc. Faraday Trans.* **1963**, *59*, 1559-1563.

(58) Snyder, R. G.; Scherer, J. R.; Gaber, B. P. *Biochim. Biophys. Acta* **1980**, *601*, 47-53.

(59) Ingólfsson, Helgi I.; Andersen, Olaf S. *Biophys. J.* **2011**, *101*, 847-855.

(60) Holte, L. L.; Gawrisch, K. *Biochem.* **1997**, *36*, 4669-4674.

(61) Fox, C. B.; Harris, J. M. *J. Raman Spectrosc.* **2010**, *41*, 498-507.

(62) Russell, C. J.; Thorgeirsson, T. E.; Shin, Y.-K. *Biochem.* **1996**, *35*, 9526-9532.

(63) Käsbauer, M.; Bayerl, T. *Langmuir* **1999**, *15*, 2431-2434.

(64) Hollinshead, C. M.; Hanna, M.; Barlow, D. J.; De Biasi, V.; Bucknall, D. G.;

Camilleri, P.; Hutt, A. J.; Lawrence, M. J.; Lu, J. R.; Su, T. J. *Biochim. Biophys. Acta* **2001**, *1511*, 49-59.

(65) Babayco, C. B.; Turgut, S.; Smith, A. M.; Sanii, B.; Land, D.; Parikh, A. N. *Soft Matter* **2010**, *6*, 5877-5881.

(66) Anderson, N. A.; Richter, L. J.; Stephenson, J. C.; Briggman, K. A. *Langmuir* **2006**, *22*, 8333-8336.

(67) Parikh, A. N.; Beers, J. D.; Shreve, A. P.; Swanson, B. I. *Langmuir* **1999**, *15*, 5369-5381.

(68) Guard-Friar, D.; Chen, C. H.; Engle, A. S. *J. Phys. Chem.* **1985**, *89*, 1810-1813.

(69) Gaber, B. P.; Yager, P.; Peticolas, W. L. *Biophys. J.* **1978**, *22*, 191-207.

(70) Abbott, R. J.; Oxtoby, D. W. *J. Chem. Phys.* **1979**, *70*, 4703-4707.

APPENDIX A

SPATIAL FILTERING OF A DIODE LASER BEAM FOR CONFOCAL RAMAN MICROSCOPY

A.1 Introduction

Development of inexpensive, single-longitudinal-mode diode lasers has led to an increase in their use as sources for Raman spectroscopy. Compared to an ion-laser source, a single-mode diode laser represents a 10-fold smaller capital investment, a 3000-fold improved electrical efficiency,[1, 2] elimination of cooling requirements, a 10-fold increase in operating lifetime,[3] and a much smaller footprint on the bench. Despite the benefits, single-mode diode lasers have not replaced gas-ion lasers in all Raman spectroscopy applications, especially those that require high transverse-mode quality, which is lacking in diode-laser beams.[2] The problem arises from the highly-divergent, asymmetric light 'cone' produced by the planar diode junction. The resulting beam is divergent and astigmatic, having a non-Gaussian (sometimes 'circularized') intensity profile in the far-field, producing asymmetric foci in the near-field that impede high-resolution confocal or optical-trapping Raman microscopy applications.[4-6]

Adapted with permission from: Kitt, J.P.; Bryce, D.A.; Harris J.M.; Spatial Filtering of a Diode Laser Beam for Confocal Raman Microscopy, *Appl. Spectrosc.*, **2015**, 69(4), 513-517, DOI: 10.1366/14-07671.

A common way to address this challenge is to couple the beam into a single-mode optical fiber and collimate the beam at the fiber exit. However, there are several drawbacks to using an optical fiber for this purpose. Coupling the laser to the fiber is challenging and losses from Fresnel reflection at the fiber end-face and poor mode matching of the beam into the fiber result in coupling efficiencies typically 40% or less.[7] In addition feedback from reflections from the fiber ends back into the laser can lead to intensity and frequency instabilities, requiring optical isolation with a Faraday rotator.[8] Additionally, optical fibers allow limited power density to avoid generating color-centers in the fiber core resulting in absorption losses and luminescence in the fiber.[9] Excitation through a fiber can also lead to Raman-specific problems, including within-fiber spontaneous- and stimulated-Raman scattering and Brillouin scattering, which contribute to band-broadening and interfering backgrounds.[10] Filtering these interferences from the excitation light is a challenge as they are spectrally close to the laser wavelength and require specialized filters to remove, which can be expensive and lossy. These issues suggest the need for a nonfiber-based method of beam cleanup for use in confocal Raman microscopy.

In this work, we develop a spatial filter for a diode-laser beam using a pinhole aperture in the near-field to produce a symmetrical Gaussian-shaped beam suitable for a confocal-Raman microscope assembled on an optical table or breadboard. The beam from a 638-nm single-longitudinal-mode diode laser with poor transverse-mode quality was cleaned up to produce comparable results for confocal Raman microscopy as a 647-nm Kr^+ laser. The capabilities of the spatially filtered, collimated excitation are tested for application in optical-trapping confocal Raman microscopy of 1-μm phospholipid vesicles.

A.2 Experimental Section

A.2.1 Confocal Raman Microscope

The Raman microscope used in this study was constructed as follows. The beam from a 638-nm single-longitudinal-mode diode laser (Innovative Photonic Solutions Part# 10638SH0035B-TH-L) is directed into a spatial filter (Thorlabs, KT310) where the standard x-y pinhole translator has been replaced with a micrometer driven translator (Thorlabs, ST1XY-D/M). The beam is focused through a 5 μm pinhole and subsequently collimated using a pair of anti-reflection coated, aspheric lenses (Thorlabs, C560TME-A). The collimated beam is then directed through an excitation filter (Semrock, FF01-640/14) and reflected off of a dichroic beam-splitter (Semrock, Di02-R635) to slightly overfill the back aperature of a 100X, 1.4 N.A. oil immersion objective (Nikon, Plan APO VC) mounted on an inverted fluorescence microscope frame (Nikon Eclipse TE-200). Scattered light is collected back through the objective and passed back through the dichroic beam-splitter. The light emerging from the microscope side-port is then collected, collimated and passed through a final high-pass filter (Semrock, BLP01-635R). The Raman scattered light is then focused onto the entrance slit of a Chromex 250IS spectrograph set to 50 μm, defining the confocal aperture in the horizontal-dimension. The vertical dimension of the aperture is defined[11] by limiting acquisition to 3-pixel rows (78 μm) on a charge couple device (CCD) detector (Andor, iDus DU401A). Spectra were dispersed with a 600 lines/mm diffraction grating blazed at 750-nm. A photo and diagram of the spatial filter showing its relationship to the microscope and spectrograph are in Figure A.1.

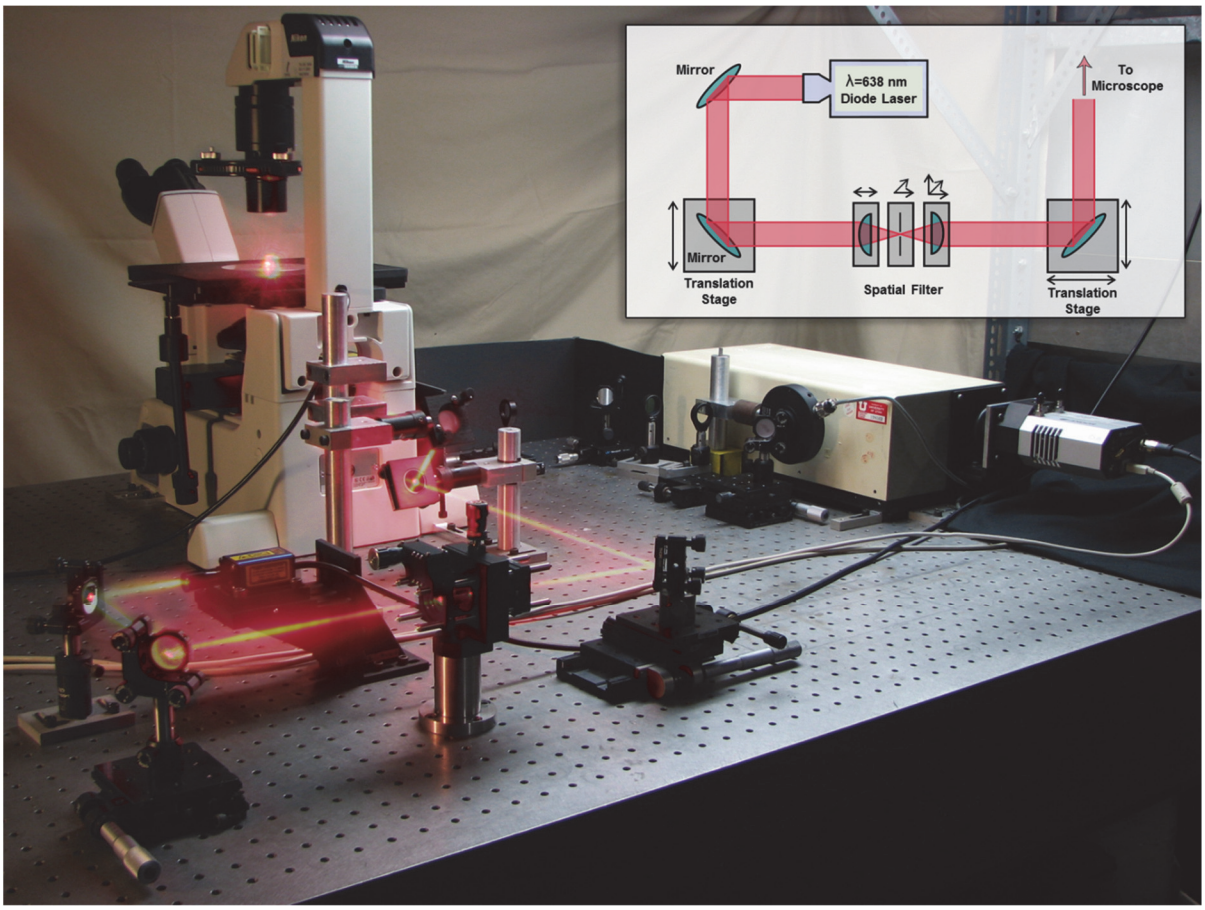

Figure A.1. Confocal Raman microscope with the spatial filter in the excitation beam path. Inset is a schematic diagram of the alignment optics and spatial filter.

A.2.2 Beam Characterization and Raman Microscopy Applications

Images of the excitation beam in the far field were acquired by impinging it on freshly-smoked magnesium-oxide[12, 13] deposited onto a glass microscope slide, and photographing the scattered light with a digital camera (Canon Powershot S3 IS). Images of the near-field focused spot were obtained by photographing the reflection of the focused beam at the coverslip-water interface using an eyepiece camera (EM-310C, BigCatchUSA), where the image size-scale was calibrated with a Ronchi ruling (Edmund Optics). Neutral density filters were used to adjust the beam intensity to maintain a linear response in the center pixels. Color maps of beam intensity profiles were produced using ImageJ[14] software. Near-field cross-sectional intensity profiles of filtered and unfiltered were fit to Gaussian and Lorentzian shapes, respectively, in Origin.

To measure the divergence of the filtered and unfiltered beam, the beam diameter was measured as a function of distance from the source. This was accomplished by photographing the beam projected onto a ruled-paper target where both the beam and a printed ruling were visible in the image. The ruling was used to calibrate each image for measurement in imageJ[14].

Typically, the diameter of a Gaussian laser beam is measured where the intensity decreases to $1/e^2$ (13.5%) of the intensity maximum. In the present experiments, however, because the unfiltered beam has a non-Gaussian shape, the beam radius was determined by numerically integrating the beam intensity in ImageJ[14] to determine the radius of a circular area which contains 86% of the total light power (equivalent to the intensity contained within the $1/e^2$ diameter of a Gaussian beam).

To demonstrate optical-trapping confocal-Raman microscopy with this setup, 1-μm

vesicles having membranes of 1,2-dipalmitoyl-sn-glycero-3-phosphocholine (DPPC) were prepared by extrusion of a 1 mg/mL solution of DPPC at 60°C through a 1-μm track-etched polycarbonate membrane (Whatman, Nucleopore). Trapping of these vesicles from aqueous solution was confirmed in bright field images, Raman scattering from the phospholipid bilayer was detected with sensitivity comparable to focused Kr^+-laser excitation.

A.3 Results and Discussion

A.3.1 Spatial Filter Optimization and Performance

Spatial filtering is a well-established technique for removing high spatial frequencies from a laser beam in the far-field by focusing the beam through a small aperture in the near-field.[8] The angular dispersion that defines the high-frequency noise is projected spatially outside of the low-frequency (Gaussian) beam-waist in the near-field.[6, 8, 15] By choosing an appropriate aperture size, it is possible to block the higher spatial-frequency noise and produce a Gaussian beam when the image is recollimated in the far-field. The diameter of the pinhole required depends on the lowest spatial frequency of the noise that is to be blocked, according to:[8]

$$d = 2f\lambda\nu \qquad \text{[Eq. A.1]}$$

where d is the diameter of the pinhole, f is the focal length of the focusing lens, λ is the wavelength of the source, and ν is the lowest spatial frequency of the noise to be filtered. Thus to eliminate spatial noise on the order of half the beam size, typical of a diode laser (see Figure A.2A), the pinhole diameter must be of $d = 2f\lambda/w$ (where the lowest spatial frequency, $\nu \sim 1/w$, where w is the $1/e^2$ radius of the beam). For the current application,

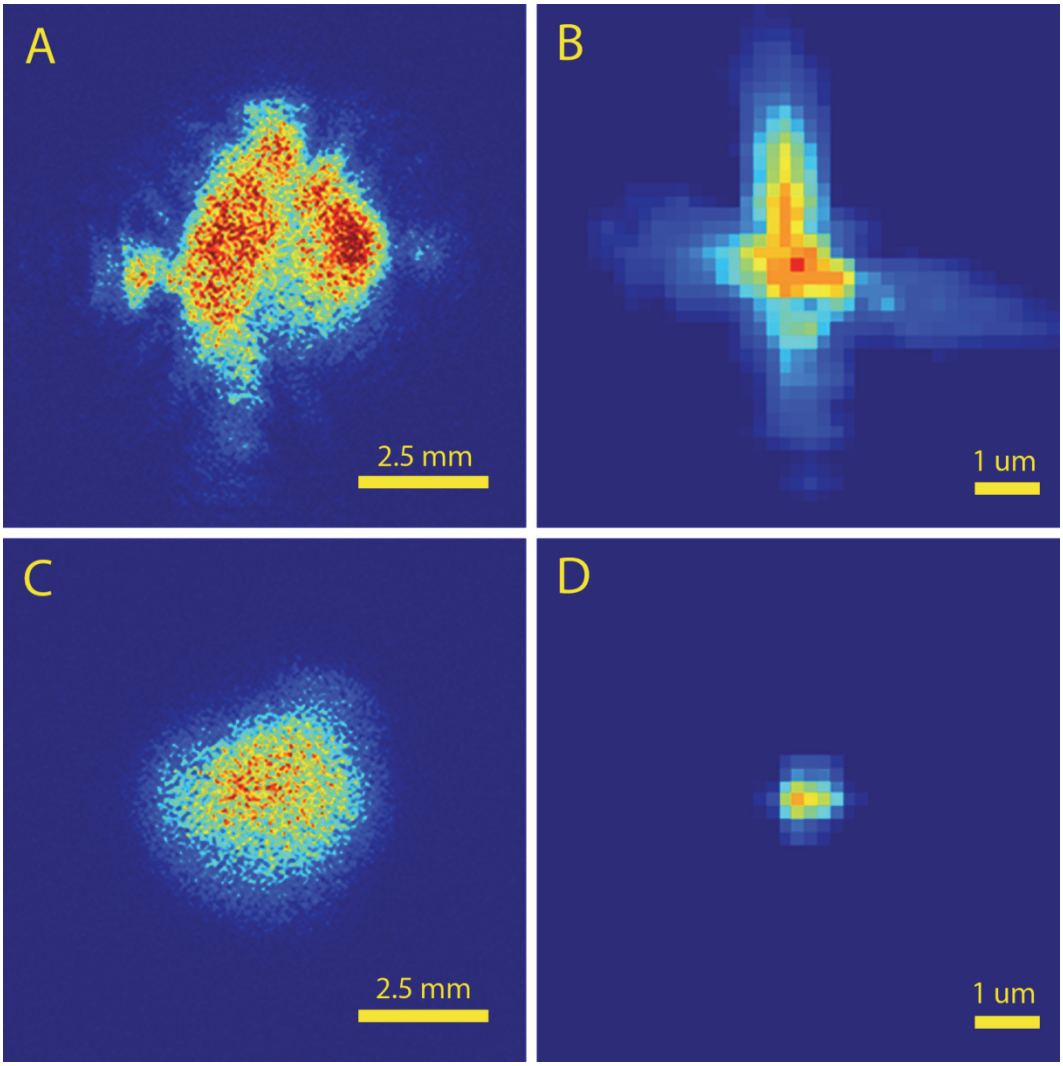

Figure A.2. Intensity maps of the diode laser beam in the far field (A and C) and at the near-field focus (B and D) before (top) and after (bottom) spatial filtering.

the diameter of the beam in the far field corresponds to a spatial frequency $\nu = 1/w$ = ~1/2.8 mm (Figure A.2A), requiring a pinhole radius of ~7.7 μm in diameter, where λ = 638-nm radiation and the focusing lens, f = 13.86 mm. The aperture chosen for this experiment was 5 μm based on commercial availability, which if used with a TEM_{00} laser beam of the same diameter, would result in less than a 2% loss in transmitted light intensity.[8, 16]

Aligning the spatial filter is straightforward. The laser beam is first oriented using a pair of mirrors and a micrometer-driven translation stage to be centered on the focusing and collimating lenses and perpendicular to the plane of the pinhole (see Figure A.1). It is then possible to optimize throughput by translating the pinhole in the x- y- plane and adjusting the focusing lens along the optical axis in the z-dimension. Using this approach, it was possible to achieve 63% throughput, more than 50% improvement over a typical single-mode optical fiber, while eliminating the need for spectral filtering at the fiber terminus. The spatially filtered far-field beam is symmetrical and exhibits a Gaussian intensity profile in both dimensions (compare Figure A.2A and A.2C). While transmission through a 5-μm pinhole of a purely TEM_{00} laser beam of the same diameter under these conditions would be 98%, the observed 37% loss is a consequence of the higher-order transverse-mode character of the diode-laser beam, which contains low-frequency spatial noise that accounts for its non-Gaussian far-field profile (Figure A.2A). The critical spatial characteristic of an excitation beam in confocal-Raman microscopy is quality of its near-field focus. A tightly-focused excitation beam allows the collected scattered light to be passed through a confocal aperture in the image plane of the microscope, to exclude out-of-focus radiation in both lateral (x,y) and longitudinal (z) dimensions of the sample.[4] The

vastly improved near-field performance of the spatially-filtered excitation beam is clear in the comparison of the beam images in Figure A.2B and A.2D, where the quality of the minimum focused spot reflected from a coverslip surface is greatly improved in size and symmetry. The improvement in the near-field focus is also demonstrated in one-dimensional near-field intensity profiles plotted in Figure A.3. The unfiltered diode laser focuses to a broad distribution that approximately fits a Lorentzian distribution with a radius at $1/e^2$ of the peak amplitude of $w = 2.08 \pm 0.01$ μm. The spatially filtered beam fits a Gaussian function exhibits a 72% smaller $1/e^2$ radius, $w = 0.59 \pm 0.01$ μm; this focused beam radius is still twice the diffraction-limited spot size predicted[17] for the 1.4 NA objective at a wavelength of 638 nm, where $w_0 = 0.61\,\lambda/NA = 0.28$ μm, which indicates that the spatially-filtered diode-laser beam is not a purely TEM_{00} mode. A Kr^+ laser beam focused through the same objective produces a Gaussian profile[18] that matches within 10% the predicted diffraction-limited spot size. Nevertheless, spatial filtering reduces the focused spot of the diode-laser beam by more than a 70%, to a nearly Gaussian profile at a cost of only a 37% loss in laser power.

In addition to poor transverse mode quality that limits how tightly a diode-laser beam can be focused, these beams also exhibit large divergence angles. Characterizing the propagation diode-laser beams is challenging because their poor transverse-mode affects all aspects of the propagating beam. A simple way of describe these beams, however, is to neglect mode-specific features by introducing an "M^2 factor" to account for their divergence characteristics:

$$M^2 = \frac{\theta \pi w_o}{\lambda} \qquad \text{[Eq. A.2]}$$

where θ is the laser beam divergence half-angle, w_o is the beam waist radius and λ is the

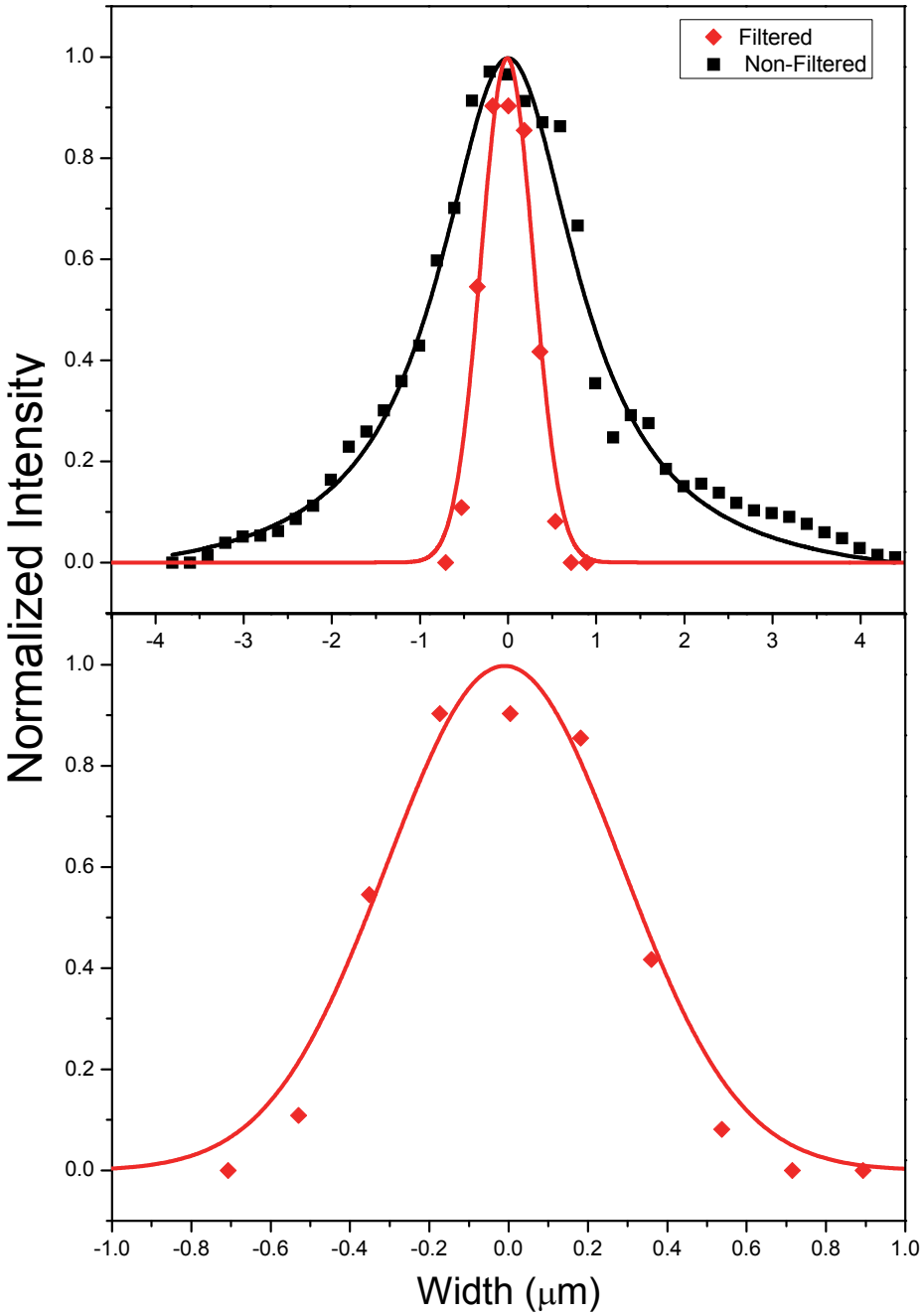

Figure A.3. Intensity maps of the diode laser beam in the far field (A and C) and at the near-field focus (B and D) before (top) and after (bottom) spatial filtering.

wavelength of the laser light. This M^2 factor is the ratio of the beam divergence and waist radius ($\theta\ w_o$) to the expected product for a diffraction-limited beam (λ/π), with a lower bound of 1, for a TEM_{00} beam.[2] The greater divergence of a non-TEM_{00} beam is reflected in a value of $M^2 >> 1$.

For the unfiltered diode-laser beam, the divergence half-angle was measured to be $\theta = 0.5 \pm 0.1$ mrad, which was consistent with the manufacturer specifications. This is much greater than the expected divergence for a diffraction-limited (0.08 mrad) beam having a $1/e^2$ beam radius, $w_o = 2.8$ mm, as reflected in an factor $M^2 = 6.8$. The spatially filtered and recollimated diode-laser beam exhibited a measured half-angle divergence of $\theta = 0.12 \pm 0.04$ mrad, which when multiplied by its measured $1/e^2$ radius, $w_o = 2.3$ mm, indicates a factor $M^2 = 1.4$, which is nearly 5-times smaller and within 40% of the M^2 factor of a single-transverse mode TEM_{00} laser beam.

The greater divergence of an unfiltered diode laser beam results in a shorter collimated region (Rayleigh range) near the beam waist given by:[19]

$$z_R = \frac{\pi {w_o}^2}{M^2 \lambda} = w_o/\theta \qquad \text{[Eq. A.3]}$$

This greater beam divergence and correspondingly shorter Rayleigh range influences the location of a new waist produced by focusing the beam, z_f, from the lens of focal length f, according to:[19]

$$z_f = f\,\frac{(2z_R/M^2 f)+1}{2z_R/M^2 f} \qquad \text{[Eq. A.4]}$$

For beams with a large M^2 factor, the focus is found well beyond the focal length of the objective. This is problematic for confocal Raman microscopy work where the sample is located through bright-field imaging at the focal plane of the infinity-corrected objective;

collection of Raman scattering is maximized by re-imaging the focal plane by means of the tube lens and relay optics onto the entrance slit of the spectrograph. Excitation light focused outside of the focal plane is subject to much lower collection efficiency. For the $M^2 = 6.8$ factor of the unfiltered diode laser beam and the $f = 2$-mm effective focal length of the 100x objective, Equations 3 and 4 predict a shift in the focus, $(z_f - f) = 3$ μm, which indeed required major adjustments of the relay optics to optimize collection of Raman scattering. For the spatially filtered beam, however, where $M^2 = 1.4$, the focus shift is negligible, $(z_f - f) = 75$ nm, which means that the excitation-beam focus is within the depth-of-field of the infinity-corrected focal plane of the objective.

A.3.2 Application to Optical-trapping Confocal-Raman Microscopy

Optical-trapping Raman microscopy, first developed for levitation and trapping of particles in the gas phase,[20-22] has more recently been applied to investigate dispersed particles in liquids,[5, 23] and both the membranes,[24, 25] and contents,[26-28] of individual phospholipid vesicles dispersed in water. Optical trapping is essential to measurement of Raman scattering from individual dispersed particles in liquids, where trapping forces counteract Brownian motion to maintain the particle in the confocal probe volume.[5] The trapping of individual phospholipid vesicles, which can be used to analyze both their membranes[24, 25] and their contents,[26-28] is more challenging than trapping solid particles. This is because the polarizability contrast responsible for the optical-trapping forces on the particle[29] is limited to the phospholipid membrane (the optical properties of the interior and exterior solutions are virtually identical), and the lipid membrane represents only a few percent of the vesicle volume.[24] Stable optical-trapping of a lipid vesicle depends on the

optical field-induced dipoles in the more polarizable vesicle membrane lowering the free energy by an amount that depends on the average squared electric field (intensity) at the center of the focus $<E^2>$, which in turn depends on the inverse of the area of the focused beam. The optical forces on the particle depend on the *spatial gradient* in intensity,[29, 30] which depend even more sensitively (3^{rd} power) on the inverse of the beam radius.

The diode laser source, prior to spatial filtering, produces a nonuniform and large (2.1-μm radius) spot in the near-field (Figures A.2B and A.3) resulting in an asymmetric profile and a modest peak intensity at its center. This produces weak optical trapping forces, where a 1-μm DPPC vesicle will remain trapped for typically less than 30 seconds, and where manipulating a vesicle in any direction through the solution causes the vesicle to be lost from the trap. By comparison, the spatially filtered and recollimated beam produces a symmetric, 0.59-μm radius focused spot in the near-field. Accounting for the 37% smaller total power, the spatially filtered beam should exhibit 7.7-times greater intensity at its center, and thus lower the free energy of an optically-trapped vesicle by a proportionally greater amount. The improved trapping energy is indeed observed in practice, where vesicles trapped in the focus of the spatially-filtered beam remain for hours and are easily dragged through the solution without escaping the trap.

The tightly focused, Gaussian-shaped beam not only improves optical-trapping, it also increases the efficiency of exciting and collecting Raman scattering from a small vesicle. Example Raman spectra from individual 1-μm DPPC vesicles trapped and excited with the unfiltered and spatially-filtered beams are compared in Figure A.4. The spectrum from the vesicle trapped and excited by the spatially filtered beam shows a 7-fold greater Raman scattering signal than the spectrum from the vesicle in the unfiltered beam, which

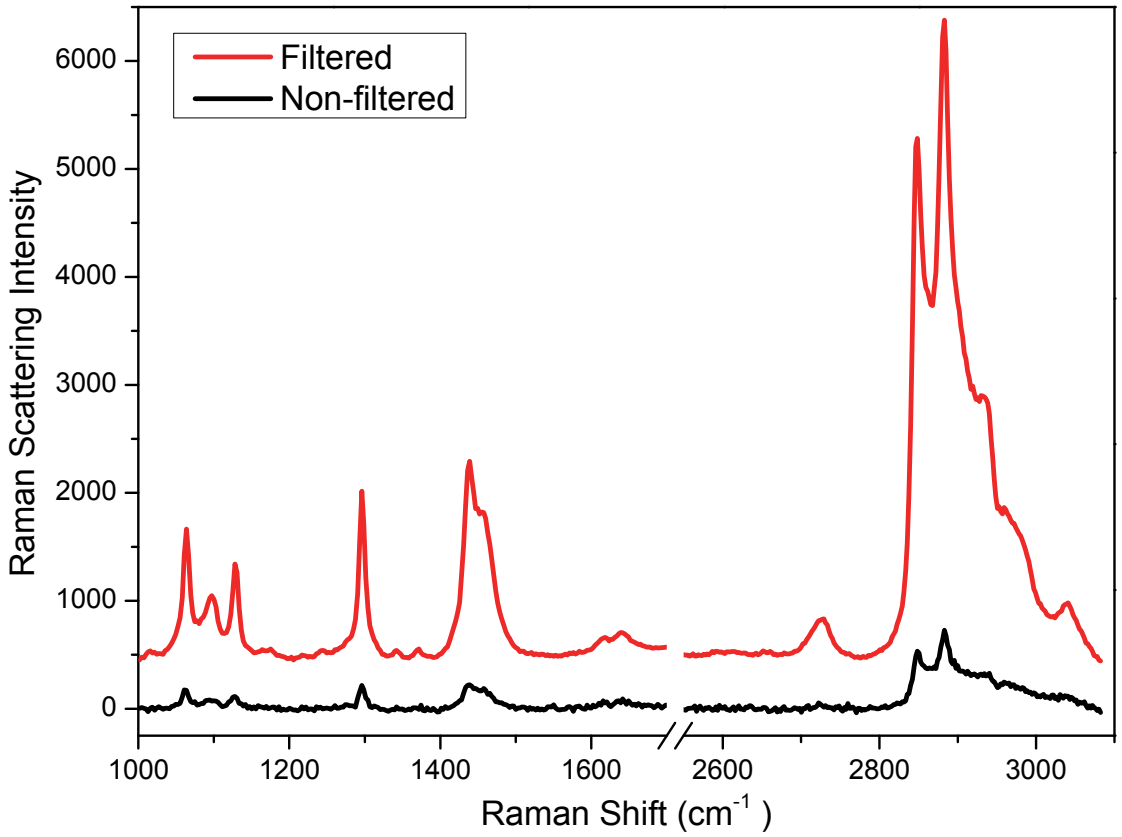

Figure A.4. Raman scattering collected from an optically-trapped 1-μm DPPC vesicle. Spectra from 30-s integrations using the unfiltered diode-laser beam are shown in black and using the spatially-filtered source are in red. A 7-fold greater Raman scattering intensity is observed with the spatially filtered source due to tighter focused excitation in the confocal volume.

is very close to the ratio of the excitation intensities at the centers of the two beams, as predicted from their relative beam sizes and the difference in total power, above. This is a reasonable result, because in both cases, the optically-trapped phospholipid vesicle is significantly smaller than the beam diameter, so that entire vesicle can reside near the center of the beam.

A.4 Conclusions

In this work, we have applied spatial filtering, with a pinhole aperture and recollimation, to a 638-nm diode laser beam that initially has poor transverse mode quality and large divergence; the resulting spatially filtered beam generates a smooth, Gaussian excitation profile at its focus in a Raman microscope. This is a simple and inexpensive approach to replacing an ion laser in a confocal Raman microscope. The improvement in the quality of the focused excitation is especially important when the laser beam is also used for optical-trapping of small particles, where trapping energies depend on the beam center intensity and trapping forces depend on the corresponding intensity gradient.[29] Spatial filtering reduced the power of the diode-laser beam by 37%, but at its focus in a confocal Raman microscope, the symmetric, near-Gaussian and 70% smaller radius excitation beam yielded more stable optical trapping and 7-fold greater Raman scattering intensity from optically-trapped 1-μm phospholipid vesicles.

A.4 References

1. A.K. Maini. Lasers and Optoelectronics: Fundamentals, Devices and Applications. West Sussex, UK.: John Wiley and Sons Ltd., 2013. 1st ed.

2. R. Paschotta. Encyclopedia of Laser Physics and Technology. Weinheim,

Germany: Wiley-VCH, 2008.

3. W.T. Silfvast. Laser Fundamentals. Cambridge, UK.: Cambridge University Press, 2004. 2nd ed.

4. O. Hollricher, W. Ibach. "High-Resolution Optical and Confocal Microscopy", In: T. Dieing, O. Hollricher and J. Toporski, Eds. Confocal Raman Microscopy, T. Dieing, O. Hollricher and J. Toporski, Eds. Springer Berlin Heidelberg, 2011, 1, Pp. 1-20.

5. D.P. Cherney, J.M. Harris. "Confocal Raman microscopy of optical-trapped particles in liquids". Ann. Rev. of Anal. Chem. 2010. 3: 277-297.

6. E. Gratton. "Laser sources for confocal microscopy", Handbook of biological confocal microscopy Springer, 1995. Pp. 69-97.

7. I. Ladany. "Laser to single-mode fiber coupling in the laboratory". Appl. Opt. 1993. 32(18): 3233-3236.

8. A.E. Siegman. Lasers. Mill Valley, CA.: University Science Books, 1986.

9. R.H. Phillip St.J., D.P.; Chow, Y.K.; Poyntz-Writght, L.J.;, "Optically induced creation, transformation and organisation of defects and color centers in optical fibers" In: F. Ouellette, editor. Proc. SPIE 1516, International Workshop on Photoinduced Self-Organization Effects in Optical Fiber. Quebec City, Canada; December 30, 1991. Pp. 47-54.

10. N.G. Singh, R.; Singh, S.P.;. "Nonlinear Scattering Effects in Optical Fibers". Prog. Electromagn. Res. 2007. 74: 379-405.

11. K.P.J. Williams, G.D. Pitt, D.N. Batchelder, B.J. Kip. "Confocal Raman microspectroscopy using a stigmatic spectrograph and CCD detector". Appl. Spectrosc. 1994. 48(2): 232-235.

12. G.W. Gordon-Smith. "The Spectral Reflection Characteristics of a Smoked Magnesium Oxide Surface". Proc. Phys. Soc., London, Sec. B. 1952. 65(4): 275.

13. W. Budde. "Calibration of Reflectance Standards". J. Res. Natl. Bur.Stand., Sect A. 1976. 80(4): 585- 595.

14. W.S. Rasband, "ImageJ", U.S. National Institutes of Health, Bethesda, Maryland, USA, 1997-2014.

15. B.D. Beier. "Confocal Raman Microscpectroscopy of Oral Streptococci" [Ph.D. Dissertation]. Rochester, NY, University of Rochester, 2011.

16. J.D. Gaskill, ;. Linear Systems, Fourier Transforms, and Optics. New York, NY.: John Wiley and Sons Inc., 1978.

17. N.J. Everall. "Modeling and Measuring the Effect of Refraction on the Depth Resolution of Confocal Raman Microscopy". Appl. Spectrosc. 2000. 54(6): 773-782.

18. T.E. Bridges, M.P. Houlne, J.M. Harris. "Spatially Resolved Analysis of Small Particles by Confocal Raman Microscopy: Depth Profiling and Optical Trapping". Anal. Chem. 2003. 76(3): 576-584.

19. H. Sun. Laser Diode Beam Basics, Manipulations and Characterizations. New York: Springer 2012.

20. R. Thurn, W. Kiefer. "Raman-Microsampling Technique Applying Optical Levitation by Radiation Pressure". Appl. Spectrosc.. 1984. 38: 78-83.

21. R. Thurn, W. Kiefer. "Structural resonances observed in the Raman spectra of optically levitated liquid droplets". Appl. Opt. 1985. 24(10): 1515-1519.

22. R.E. Preston, T.R. Lettieri, H.G. Semerjian. "Characterization of single levitated droplets by Raman spectroscopy". Langmuir. 1985. 1(3): 365-367.

23. M.P. Houlne, C.M. Sjostrom, R.H. Uibel, J.A. Kleimeyer, J.M. Harris. "Confocal Raman Microscopy for Monitoring Chemical Reactions on Single Optically Trapped, Solid-Phase Support Particles". Anal. Chem. 2002. 74(17): 4311-4319.

24. D.P. Cherney, J.C. Conboy, J.M. Harris. "Optical-Trapping Raman Microscopy Detection of Single Unilamellar Lipid Vesicles". Anal. Chem. 2003. 75(23): 6621-6628.

25. C.B. Fox, G.A. Myers, J.M. Harris. "Temperature-Controlled Confocal Raman Microscopy to Detect Phase Transitions in Phospholipid Vesicles". Appl. Spec. 2007. 61(5): 465-469.

26. K. Ajito, C. Han, K. Torimitsu. "Detection of Glutamate in Optically Trapped Single Nerve Terminals by Raman Spectroscopy". Anal. Chem. 2004. 76(9): 2506-2510.

27. G.A. Myers, J.M. Harris. "Confocal Raman Microscopy of pH-Gradient-Based 10,000-Fold Preconcentration of Compounds within Individual, Optically Trapped Phospholipid Vesicles". Anal. Chem. 2011. 83(15): 6098-6105.

28. J.J. Schaefer, C. Ma, J.M. Harris. "Confocal Raman Microscopy Probing of Temperature-Controlled Release from Individual, Optically-Trapped Phospholipid Vesicles". Anal. Chem. 2012. 84(21): 9505-9512.

29. A. Ashkin, J.M. Dziedzic, J.E. Bjorkholm, S. Chu. "Observation of a single-beam gradient force optical trap for dielectric particles". Opt. Lett. 1986. 11(5): 288-290.

30. D.P. Cherney, T.E. Bridges, J.M. Harris. "Optical Trapping of Unilamellar Phospholipid Vesicles: Investigation of the Effect of Optical Forces on the Lipid Membrane Shape by Confocal-Raman Microscopy". Anal. Chem. 2004. 76(17): 4920-4928.

APPENDIX B

CALORIMETRY-DERIVED COMPOSITION VECTORS TO RESOLVE COMPONENT RAMAN SPECTRA IN PHOSPHOLIPID PHASE TRANSITIONS

B.1 Introduction

Vibrational spectroscopy is a well-established technique for investigating composition of mixed samples and their variation during a chemical process. As a process proceeds, changes in molecular structure or sample composition result in variation in spectral features. Thus, by measuring spectra as a function of an experimental or process variable (e.g., time, temperature, pH), an understanding of structural changes during the process can be gained. The challenge of this type of analysis is developing knowledge of the relationship between spectral changes and the variable driving the chemical process or change in composition.

The analysis of multicomponent spectral data is simplified in the case where the measured spectra can be represented as linear combinations of underlying components, whose contributions vary as a function of the chemical process. These data can be

---

Adapted with permission from: Kitt, J.P.; Bryce, D.A.; Harris J.M.; Calorimetry-Derived Composition Vectors to Resolve Component Raman Spectra in Phospholipid Phase Transitions, *Appl. Spectrosc.*, **2016**, In-Press.

expressed as an *r* x *c* matrix, $\boldsymbol{D}$, of spectra measured at *r* wavelengths or wavenumbers arranged in columns at *c* different values of the chemical process variable that controls composition. If the spectral response of the underlying *n* components is independent of their concentrations, then data matrix can be represented by the product[1-3] of an *r* x *n* matrix of spectral components ($\boldsymbol{A}$) and an *n* x *c* matrix ($\boldsymbol{C}$) of the component concentrations over the *c* conditions:

$$\boldsymbol{D} = \boldsymbol{AC} \qquad \text{[Eq. B.1]}$$

If the composition variation ($\boldsymbol{C}$) is known, a classical least-squares estimate of the component spectra ($\widehat{\boldsymbol{A}}$) can be determined by multiplying the data matrix ($\boldsymbol{D}$) by the right pseudoinverse[4] of the composition matrix ($\boldsymbol{C}$):

$$\widehat{\boldsymbol{A}} = \boldsymbol{DC^T}[\boldsymbol{CC^T}]^{-1} \qquad \text{[Eq. B.2]}$$

With knowledge of the resolved component spectra, one can use these to query the composition of unknown samples.[1-3] The contributions of these component spectra in a data set, $\boldsymbol{D}$, can be determined by multiplying the data matrix by the left pseudoinverse of $\widehat{\boldsymbol{A}}$ to obtain a least-squares estimate of the composition matrix $\widehat{\boldsymbol{C}}$.

$$\widehat{\boldsymbol{C}} = \left[\widehat{\boldsymbol{A}}^{\boldsymbol{T}}\widehat{\boldsymbol{A}}\right]\widehat{\boldsymbol{A}}^{\boldsymbol{T}}\boldsymbol{D} \qquad \text{[Eq. B.3]}$$

The initial resolution of the component spectra, therefore, depends on knowledge of the composition variation, $\boldsymbol{C}$. In the simplest case, a calibration data set can be acquired with known concentrations of components in a series of samples, $\boldsymbol{C}$. The resulting data set can be analyzed by least squares (Eq. B.3) to discover the component spectra $\widehat{\boldsymbol{A}}$ in the data. This approach has been used to resolve spectral contributions to mixtures and those spectra can be used to determine the compositions of unknown samples (Eq. B.3).[3]

Even without prior knowledge of the composition variation, it is possible to

discover that variation in an unknown spectral data set through the use of a physical model for the chemical process. In this case, a functional form for the component variation is used to model the rows of the matrix $\boldsymbol{C}$, where each composition vector depends on a small number of typically nonlinear parameters. A search for the parameters to define the optimal $\widehat{\boldsymbol{C}}$ is carried out, where for any set of parameters, the best-fit spectra are determined by linear least-squares (Eq. B.2); the quality of fit is optimized by minimizing the sum of the squared residuals, given by the sum of the square of the residuals = $\boldsymbol{tr(R^T R)}$, where $\boldsymbol{R} = \boldsymbol{D} - \widehat{\boldsymbol{A}}\widehat{\boldsymbol{C}}$. Examples of physical models that have been successfully applied to the analysis of component vibrational spectra from unknown data sets include the resolution of ground and excited-state Raman spectra from their excitation intensity-dependence,[5] the determination of donor and acceptor triplet-state Raman spectra through modeling their time-resolved energy transfer kinetics,[6] the separation of adsorbate infrared spectra on heterogeneous surfaces by modeling their concentration-dependent isotherms,[7, 8] and finally, by modeling differences in the time-dependent accumulation of adsorbed versus and surface-bound silane reagents in sol-gel silica films; the infrared spectra of these component could be resolved.[9]

In the present work, we propose to employ multidimensional least-squares analysis to resolve temperature-dependent component variations in vibrational spectra. Because vibrational spectroscopy can provide both structurally-informative and quantitative results, it is frequently used to investigate changes in materials as a function of temperature. Despite the need for resolution of structural variation in these processes, there is a challenge of finding an adequate model that captures the temperature-dependent evolution of component composition. Composition variation based on simple Van't Hoff models rarely

describe the actual temperature-dependent behavior of complex materials.[10, 11] This situation has led to more complex models to predict temperature-dependent evolution in structure.[12, 13] These models, however, often require time consuming iterative calculations, with many variables that must be simultaneously varied and optimized to fit a set of data.

In the absence of prior knowledge of $\boldsymbol{C}$ or a physical model for its composition variation in a complex system, one can search out the correlated behavior in a set of spectra by a model-free method, self-modeling curve resolution (SMCR).[14, 15] SMCR is accomplished by eigenvector decomposition of the spectral data to determine a small basis-set of eigenvectors that capture the correlated spectral variation in the process. The matrices of the spectral components and their respective concentrations are found by searching for the *n* x *n* elements of a rotation matrix that transforms the eigenvector representation into the real-space vectors, $\widehat{\boldsymbol{A}}$ and $\widehat{\boldsymbol{C}}$.

Self-modeling curve resolution in multidimensional vibrational spectroscopy has been used to determine component Raman spectra of sulfuric-acid species in solutions of varying sulfuric-acid concentration[16] and methanol-water complexes from infrared spectra of their aqueous solutions.[17] SMCR has been employed to elucidate Raman spectra of triplet excited-states[5, 18] and to determine intermediate structures in surface-enhanced Raman spectra of potential-dependent self-assembly of monolayers.[19] SMCR has also been applied in temperature-dependent Raman spectroscopy to investigate DPPC bilayer melting using piecewise two-component approach to solving an intractable four-component curve resolution problem.[20] This piecewise decomposition approach highlights a major challenge of self-modeling curve resolution: that the number of elements in rotation matrix, which transforms the abstract eigenvectors into component spectra, is the square of

the number of spectral components.[14, 15] For systems with two varying components, four parameters specify the coordinates of the two pure components that lie at the ends of a line defining their relative contributions in an eigenvector space to the samples that were measured. The search along a line for the elements of the 2 × 2 rotation matrix is relative easy; for a 3-component system, however, the search is for the 9 elements of a 3 × 3 matrix that define the apices of a triangle lying on a plane in a 3-dimensional space. The dimensionality of the larger space makes determination of the transformation matrix increasingly challenging. Additionally, this search is not based on least-squares criteria because the solution is underdetermined. Searches are typically bounded or penalized for solutions that produce negative-going spectral components or concentrations, and programming these bounds in an optimization algorithm is daunting, especially when the number of components is large.[21, 22]

Given the inadequacies of simple models for temperature-dependent processes and the limitations of model-free methods for resolving multiple spectral components in these data sets, we propose a simple empirical approach to resolving component spectra that arise in thermal phase-transitions of materials. Our approach is to derive empirical composition vectors from differential scanning calorimetry (DSC) of the material, which are then used for least-squares resolution of the component spectra. The enthalpy changes associated with a thermal phase transition can be determined by integrating heat-capacity profiles from DSC. The temperature-dependent transfer of heat into the sample through the phase transition is proportional to the extent of melting,[23] corresponding to the relative change in the concentrations of the two phases. The measured enthalpy change across a phase transition versus temperature can, therefore, be used to construct empirical composition

vectors for the two phases, which can then be employed in the analysis of temperature-dependent spectra.

In the present work, this concept is applied to the analysis of thermal phase transitions of DMPC (1,2-dipalmitoyl-sn-glycero-3-phosphocholine) phospholipid vesicles, which are investigated through the acquisition Raman spectra of individual vesicles, collected as a function of temperature using optical-trapping confocal Raman microscopy. A traditional self-modeling curve resolution analysis of these spectra shows that there are insufficient spectral differences between the lipid phases to provide a clean separation of the component responses. The temperature dependent heat-capacity of an aliquot of the vesicle suspension can, however, be readily measured with differential scanning calorimetry. The enthalpy changes corresponding to each transition are determined by integrating the heat-capacity profile and used to construct a series of composition vectors, where the relative concentration of each component is proportional to the enthalpy change between phases. A modified least-squares analysis is then carried out using these empirical composition vectors to resolve spectra corresponding to gel, ripple, and liquid-crystalline phases of DMPC, whose projections onto the original temperature-dependent data are optimized for their consistency with the calorimetry-derived composition vectors.

B.2 Experimental Section

B.2.1 Reagents and Materials

Chloroform (Chromasolv Plus, ≥99.9%) was obtained from Sigma Aldrich (St. Louis, MO). DMPC (1,2-dimyristoyl-sn-glycero-3-phosphocholine) was acquired from

Avanti Polar Lipids, Inc. Stock solutions of DMPC in chloroform were made without further purification and stored at -20°C until use. Water used in all experiments was filtered using a Barnstead GenPure UV system (ThermoFisher Scientific, Waltham, MA) and had a minimum resistivity of 18 MΩ·cm.

B.2.2 Sample Preparation and Characterization

Vesicles for confocal Raman microscopy, and differential scanning calorimetry (DSC) experiments were prepared from stock solutions of DMPC in chloroform. Aliquots of chloroform-lipid solution were pipetted into glass vials and dried under a stream of nitrogen. The dry samples were then placed under vacuum (150 mTorr) for ~2 h to ensure complete removal of chloroform from the dried lipid. Vesicles were prepared using the following procedure.[24, 25] Dried lipid was hydrated in 50 °C water (well above the DMPC phase-transition temperature of 24 °C), transferred to a preheated (50°C) bath sonicator (Branson CPX 5800, Branson Ultrasonics, Danbury, CT), and sonicated at maximum-intensity until solutions went clear ~60 min. DMPC samples for calorimetry had a final concentration of 2.5 mg/mL. Samples for spectroscopy were diluted 10-fold; sufficient to minimize the probability of an optically-trapped vesicle being bumped from the trap by another vesicle in solution.

B.2.3 Temperature-Controlled Optical-Trapping

Confocal Raman Microscopy

The confocal Raman microscope used in this work has been described previously.[26, 27] In brief, a beam expanded (50-25-4X-647 Special Optics) 647 nm Kr^+ laser beam

(Coherent, Santa Clara, CA) is reflected off of a dichroic mirror (Semrock, Lake Forest, IL), slightly overfilling the back aperture of a 100X oil immersion objective (Nikon Plan Fluor, El Segundo, CA) mounted on an inverted fluorescence microscope frame (Nikon TE-200, El Segundo, CA). The focused beam is directed into a lipid dispersion which is contained in a temperature controlled microscopy cell (Figure B.1). The polarizability contrast between the lipid bilayer of the vesicle and bulk water allows optical trapping of a single vesicle in the strong oscillating electric field at the laser focus. Excitation of Raman scattering form an individual optically-trapped vesicle is accomplished by the same laser beam. Scattered light from the trapped vesicle is collected back through the objective, and passed through a dichroic mirror and high pass filter (Semrock, Lake Forest, IL). The Raman scattered light is then focused onto the entrance slit of a grating monochromator (Bruker 500-IS, Preston, Victoria, Australia) and detected using a charge-couple-device CCD camera (Andor, iDus DU401A, South Windsor, CT). Spectra were acquired using a 300 lines/mm diffraction grating blazed at 750 nm with a resolution of 2 cm^{-1}. Confocal microscopy was accomplished by defining a confocal aperture in the horizontal dimension using the entrance slit of the monochromator (50 μm) and by binning 3-rows of pixels on the CCD camera (78 μm) in the vertical dimension.[28]

Temperature-controlled experiments were conducted in a brass microscopy sample cell. The cell comprised a cylindrical 3-mm o.d., 2-mm i.d. brass tube which transitions to a 5 cm wide base. The 2 mm inner diameter of the opening at the top of the tube was tapered to 0.5 mm at the base to prevent temperature gradients across the fluid in the measurement portion of the cell. A 22-mm x 22-mm glass coverslip was attached to the base of the cell using 140 μm thick double stick tape with a 0.25-mm radius hole cut in the center to allow

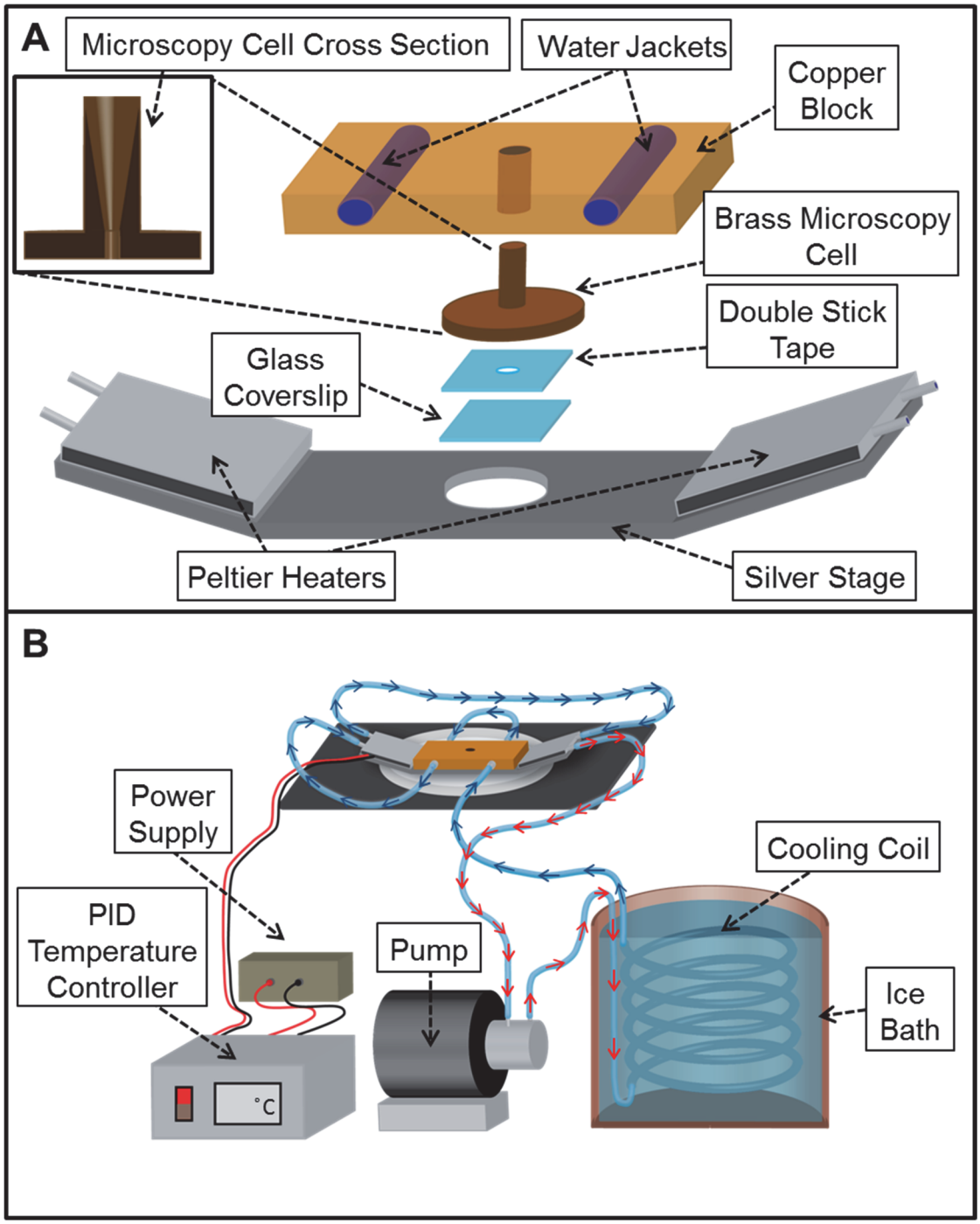

Figure B.1. Diagram of the microscope well cell temperature control apparatus. A. Expanded view of the brass well cell and temperature-controlled stage. B. Diagram of the temperature-controller fully assembled on the microscope.

fluid in the sample cell to contact the glass coverslip. The brass microscopy cell was covered by a jacketed copper block and mounted on a silver stage. The block is cooled by flowing chilled 50:50 water:ethylene glycol solution through the copper jacket using a magnetic drive pump (Micropump Inc., Vancouver, WA). Cell temperature is adjusted using a proportional-integral-derivative (PID) controller to modulate the current supplied by a DC power supply to a pair of Peltier stacks attached to either side of the stage. A diagram of the temperature control apparatus and well cell is presented in Figure B.1. Sample temperature was measured using a thermocouple inserted into the base of the sample cell.

To conduct temperature controlled Raman experiments, a series of vesicles were optically-trapped at each temperature set point. The temperature was manually adjusted (using the PID controller) in 1℃ increments across the chosen temperature range. At each temperature set point, a Raman spectrum of three optically-trapped vesicles were acquired with integration times of 30 s. Temperatures during acquisitions remained within ±0.3℃ of the PID set point.

B.2.4 Differential-Scanning Calorimetry

Calorimetry experiments were conducted using a VP-DSC (Microcal) differential-scanning calorimeter. Vesicles were prepared in 2-mL aliquots at a concentration of 2.5 mg/mL and were degassed under mild vacuum (~5 min) just prior to transfer into the calorimeter cell. Following baseline stabilization, samples were loaded into the calorimeter, and the integration of calorimetric heat-capacity curves was carried out in OriginPro 8.5.1 (OriginLab Corporation, Northampton, MA). Integral shapes were fit to

logistic functions by calorimeter cell temperature was lowered to 10℃ and allowed to equilibrate for 15 min. Calorimetry data were collected at a scan rate of 1℃/min. Baseline correction and non-linear least-squares using an OriginPro algorithm; the fitted functions provide interpolation between measured points for use in spectral analysis.

B.2.5 Multidimensional Data Analysis

Spectral data analysis was carried out in programs executed in Matlab (Mathworks, Natick, MA). Raman spectra were first corrected by fitting a 7-order polynomial function to baseline regions of the spectrum and subtracting this function from the spectral data. A baseline-corrected spectrum, with spectral regions of interest highlighted, is presented in Figure B.2. Spectra acquired in a temperature-dependent series were normalized to the phospholipid headgroup C-N stretching mode, which is insensitive to the acyl-chain structure of the lipid-tails.[29] Least-squares analysis and self-modeling curve resolution were performed on spectra that were truncated to include only regions with prominent vibrational peaks (Figure B.2), so that noise in the baseline regions did not contribute to the uncertainty in the results. The algorithm for using calorimetry-derived concentration vectors in a concentration-residuals-modified least-squares analysis[30] is presented in the next section; piece-wise self-modeling curve resolution analysis has been previously described in the literature[20] and is summarized below.

Self-modeling curve resolution (SMCR)[14, 15] for piece-wise analysis of lipid phase transitions has been previously described.[20] A brief description of the approach used in this work is provided here. Similarly to matrix least-squares spectral data (***D***) is represented by the product of an r x n matrix of pure spectral components (***A***) and an n x c matrix (***C***) of

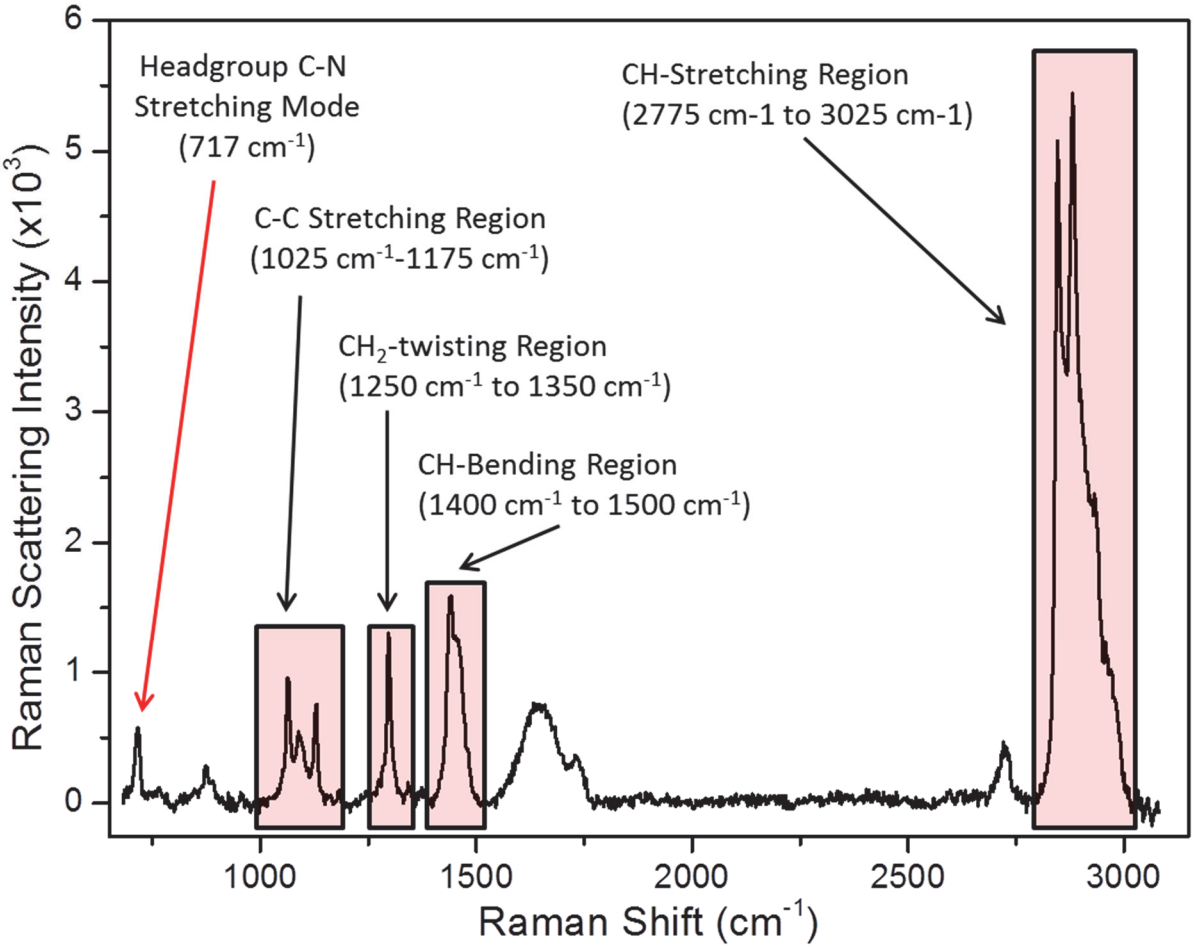

Figure B.2. Baseline corrected Raman spectrum of an optically-trapped DMPC vesicle at 12.5°C. The phospholipid headgroup CN-stretching mode used to normalize Raman spectra prior to analysis is marked by a red arrow. Regions of the spectra used for phase-transition analysis are highlighted in light-red boxes.

concentration coefficients:

$$\boldsymbol{D} = \boldsymbol{AC} \qquad \text{[Eq. B.4]}$$

In the first step of SMCR, a covariance matrix $\boldsymbol{Z}$ is produced by multiplying the intensity-normalized data matrix $\boldsymbol{D}$ and its transpose:

$$\boldsymbol{Z} = \boldsymbol{D^T D} \qquad \text{[Eq. B.5]}$$

The temperature correlation in the data is represented in the off-diagonal elements of $\boldsymbol{Z}$. To determine the number of components which adequately describe the data, $\boldsymbol{Z}$ is decomposed into a set of orthonormal eigenvectors ($\boldsymbol{Q}_o$) and corresponding eigenvalues (λ) where:

$$\boldsymbol{Q}_o^T \lambda \boldsymbol{Q}_o = \boldsymbol{Z} \qquad \text{[Eq. B.6]}$$

Much of the variation contained in the data is due to noise, thus $\boldsymbol{Q}_o$ is truncated to remove the vectors which represent the noise, leaving only eigenvectors capturing significant correlated variation in the data. The number of significant components is determined by using the Malinowski IND function and F-tests of reduced eigenvalues,[15] and by examining the eigenvector shapes for structure. Once the number of significant components is determined, vectors due to noise are removed leaving the truncated matrix of eigenvectors $\boldsymbol{Q}$. By then projecting the data ($\boldsymbol{D}$) matrix back onto the eigenvectors ($\boldsymbol{Q}$) a set of orthonormal Raman spectra is produced:

$$\boldsymbol{U} = \boldsymbol{DQ} \qquad \text{[Eq. B.7]}$$

The abstract spectral matrix $\boldsymbol{U}$ is then "rotated" into real space by postulating a rotation matrix $\boldsymbol{K}$. By recognizing that the correlated intensity variation in $\boldsymbol{D}$ is produced by a linear combination of the pure component loadings in $\boldsymbol{U}$, a plot of the columns of $\boldsymbol{U}$ against each-other is linear, and for a two-component system produces a line where the

points at the extremes represent the "purest" spectra that were measured. The search for $\boldsymbol{K}$ is confined along this line where the proper coefficients are accepted when non-negative spectra and component concentrations are found.

Because this search is challenging for more than two components, in this work, the data matrix was divided into two overlapping temperature regions (12.5 ℃ - 22.1 ℃ and 19.2 ℃ – 31.8 ℃), each containing only a single phase transition (two-components) by examining the measured calorimetry profiles. The 'redundant' component spectra corresponding to the component in the overlapping region were examined to verify equivalence and then averaged into a single component. The component spectra corresponding to each component were then loaded into a matrix ($\widehat{\boldsymbol{A}}$). The component concentration variation as a function of temperature was then determined by classical least-squares:

$$\widehat{\boldsymbol{C}} = \left[\widehat{\boldsymbol{A}}^{\boldsymbol{T}}\widehat{\boldsymbol{A}}\right]\widehat{\boldsymbol{A}}^{\boldsymbol{T}}\boldsymbol{D} \qquad \text{[Eq. B.8]}$$

B.3 Results and Discussion

B.3.1 Deriving Concentration Vectors from Calorimetry Data

The goal of this work is to use calorimetry-derived enthalpy curves as composition variables to resolve the components that comprise the vibrational spectra of a temperature-dependent process. As a model for exploring these ideas, well-characterized thermal-phase transitions of phospholipid (DMPC) vesicles were investigated. The Raman spectral data to characterize this process were acquired using confocal-Raman microscopy of individual

optically-trapped DMPC-vesicles, collecting spectra in 1°C increments as the sample temperature was increased from 10° to 30°C (Figure B.3). Spectra were truncated to regions where temperature-dependent changes occur. These regions include C-C stretching from 1025 cm^{-1}-1175 cm^{-1}, CH_2-twisting region from 1250 cm^{-1} to 1350 cm^{-1}, the CH bending region from 1400 cm^{-1} to 1500 cm^{-1}, and the CH stretching region from 2775 cm^{-1} to 3025 cm^{-1}. In the absence of a model for the composition variation with temperature, the traditional approach to the analysis of the phase-transitions in data like Figure B.3 is to search for the correlated behavior versus temperature using self-modeling curve resolution (SMCR).[14-16] SMCR is accomplished by eigenvector decomposition of the spectral data to determine a small basis-set of eigenvectors that capture the correlated spectral variation in the process. The matrices of the spectral components and their respective concentrations are found by searching for the elements of a rotation matrix that transforms the eigenvector representation into the real-space vectors, $\widehat{\boldsymbol{A}}$ and $\widehat{\boldsymbol{C}}$.

Three-component self-modeling curve resolution was carried out by piecewise decomposition of the temperature-dependent data into a pair of two-component segments,[20] one containing the gel-to-ripple transition, and the other the ripple-to-liquid crystalline transition. SMCR was carried out on each segment, and the middle components were examined to verify equivalence and then averaged to produce a component spectrum of the ripple-phase (Figure B.4). The component spectra were then used in a least-squares step (Eq. B.3) to compute the composition vectors (Figure B.5A), which show evidence of two phase transitions but also include significant levels of noise and the trading of intensity between components. The similarity of the spectra of the three phases does not provide sufficient spectral resolution to separate their contributions to the temperature-dependent

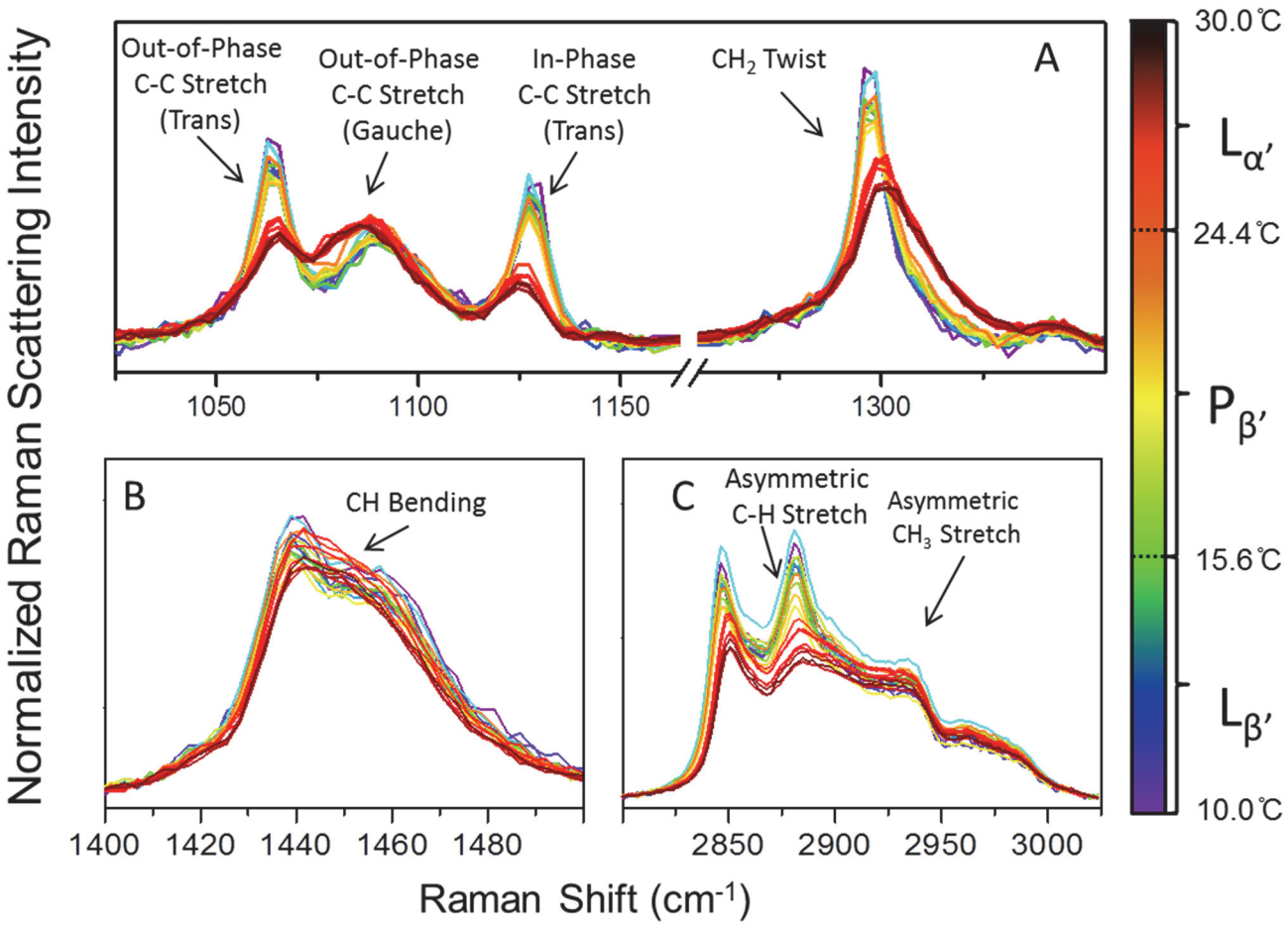

Figure B.3. Raman spectra of individual DPMC vesicles collected as a function of temperature. Only regions used for spectral analysis are shown: C-C and C-H twisting regions (A), the C-H bending region (B), and the C-H stretching region (C).

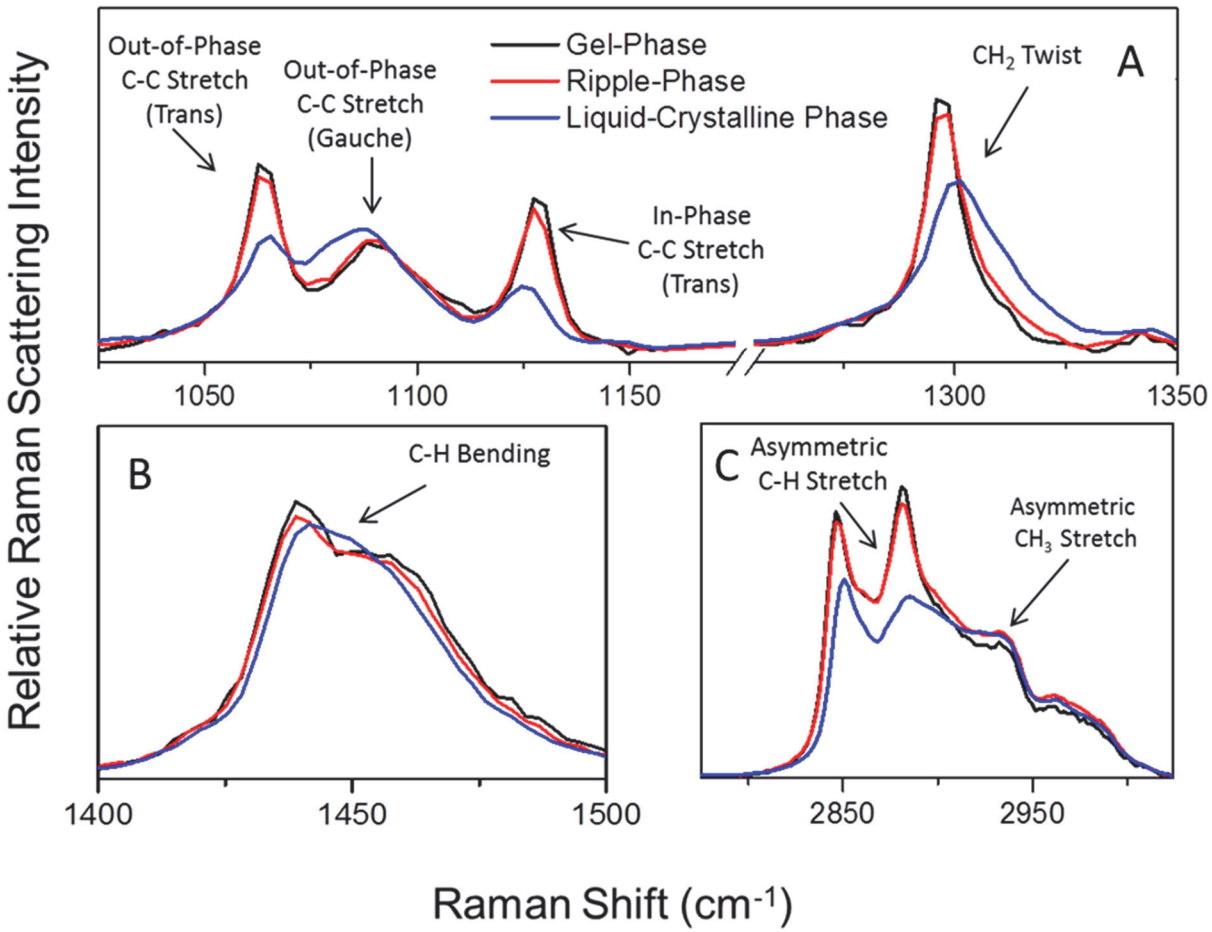

Figure B.4. Component Raman spectra resolved using self-modeling curve resolution of the C-C and C-H twisting regions (A), the C-H bending region (B), and the C-H stretching region (C). Colors correspond to the phases: Gel phase (black), ripple phase (red), and liquid-crystalline phase (blue).

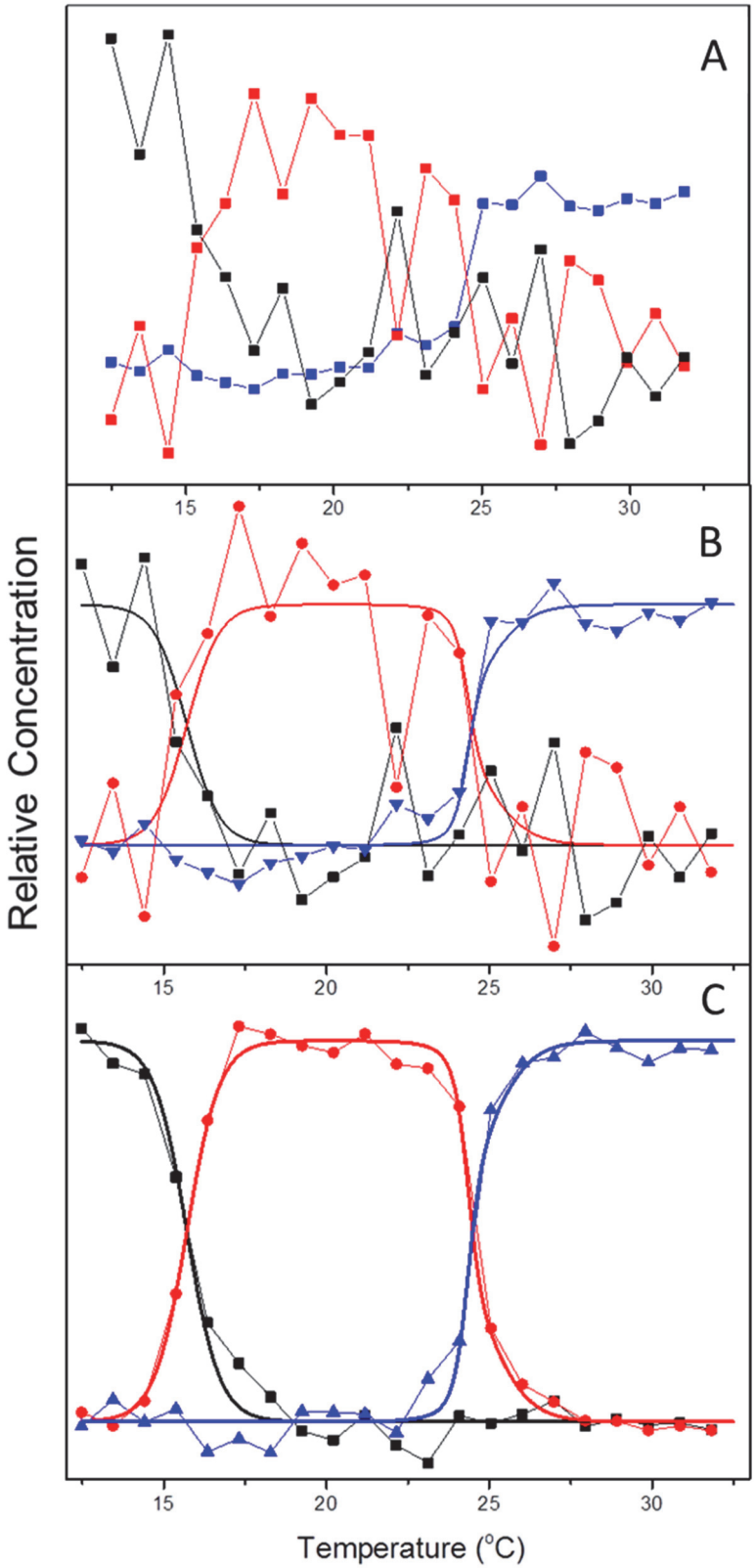

Figure B.5. Concentration vectors predicted from fitted spectra for self-modeling curve resolution (A), classical least-squares (B), and concentration-residual modified least-squares (C).

data.

The similarity of component spectra, in this case, limits the power of self-modeling curve resolution to separate the component responses; this illustrates the potential value of having a model for the temperature-dependent composition in order to resolve these data.

Differential scanning calorimetry (DSC) is a common method for characterizing phase transitions of phospholipid bilayers. The measurement is conducted by filling a sample cell with vesicle suspension and a reference cell with the suspending solution (without vesicles) and measuring the difference in power required to raise the sample and reference cell temperatures at an equivalent rate across a range of temperatures bracketing the phase transition. The difference in power is proportional to the difference in heat capacity between the sample and reference at the current temperature; thus by tracking the power required to maintain the temperature of each cell, the heat capacity as a function of temperature can be measured.

Interpretation of DSC heat capacity curves is frequently carried out using the Van't Hoff expression for enthalpy change:[23]

$$\left(\frac{\partial \ln\left(\frac{1-\alpha}{\alpha}\right)}{\partial T}\right)_p = \frac{\Delta H_{vh}}{RT^2} \qquad \text{[Eq. B.9]}$$

Here ΔH_{vh} is the Van't Hoff enthalpy, α is the degree of the phase transition (fraction melted) at temperature T and R is the ideal-gas constant. Integration of this equation with the proper set of initial conditions yields the theoretical heat-capacity curve:

$$C_p(T) = \frac{e^{-\frac{\Delta H_{vh}}{RT}\left(1-\frac{T}{Tm}\right)}\Delta H_{vh}\Delta H_{cal}}{\left(1+e^{-\frac{\Delta H_{vh}}{RT}\left(1-\frac{T}{Tm}\right)}\right)^2 RT^2} \qquad \text{[Eq. B.10]}$$

In practice, phospholipid bilayer heat capacity profiles are rarely well-fitted by a single

Van 't Hoff curve, and the present case is no exception (Figure B.6). Because the goal of this work is to develop a concentration axis for resolving the spectral components, knowledge of the degree of the transition versus temperature, $\alpha(T)$, can be determined empirically directly from the heat capacity curve, $C_p(T)$:[31]

$$C_p(T) = \Delta H_{cal} \frac{d\alpha}{dT} \qquad \text{[Eq. B.11]}$$

which can be integrated to determine the temperature-dependence of the enthalpy change:

$$\int C_p(T)\, dT = \Delta H_{cal} \alpha(T) \qquad \text{[Eq. B.11]}$$

For spectral resolution, the magnitude of the enthalpy change, ΔH_{cal}, is not essential to determining the composition profiles, so that integrated heat capacity curves are normalized to report the degree of the transition versus temperature. For multiple well-resolved phase transitions, such as the gel-to-ripple and ripple-to-liquid-crystalline phase transitions of DMPC, the concentration profiles of each component are determined by the normalized integrated enthalpy curve or by difference for components which are disappearing. For example, for the two phase transitions of a DMPC bilayer:

$$C_g = 1 - \left(\int Cp_{g\rightarrow r} dt\right)_{norm} \qquad \text{[Eq. B.12]}$$

$$C_l = \left(\int Cp_{r\rightarrow l}\, dt\right)_{norm} \qquad \text{[Eq. B.13]}$$

$$C_r = 1 - \left[\left(\int Cp_{g\rightarrow r}\, dt\right)_{norm} + \left(\int Cp_{g\rightarrow r} dt\right)_{norm}\right] \qquad \text{[Eq. B.14]}$$

Here C_g, C_l, and C_r are the concentration coefficients corresponding to each of the phases and $\left(\int Cp_{x\rightarrow y} dt\right)_{norm}$ is the normalized integral of the heat capacity curve for the transition from phase *x* to phase *y*. The calorimetry axis and corresponding empirical concentration profiles are plotted in Figure B.7.

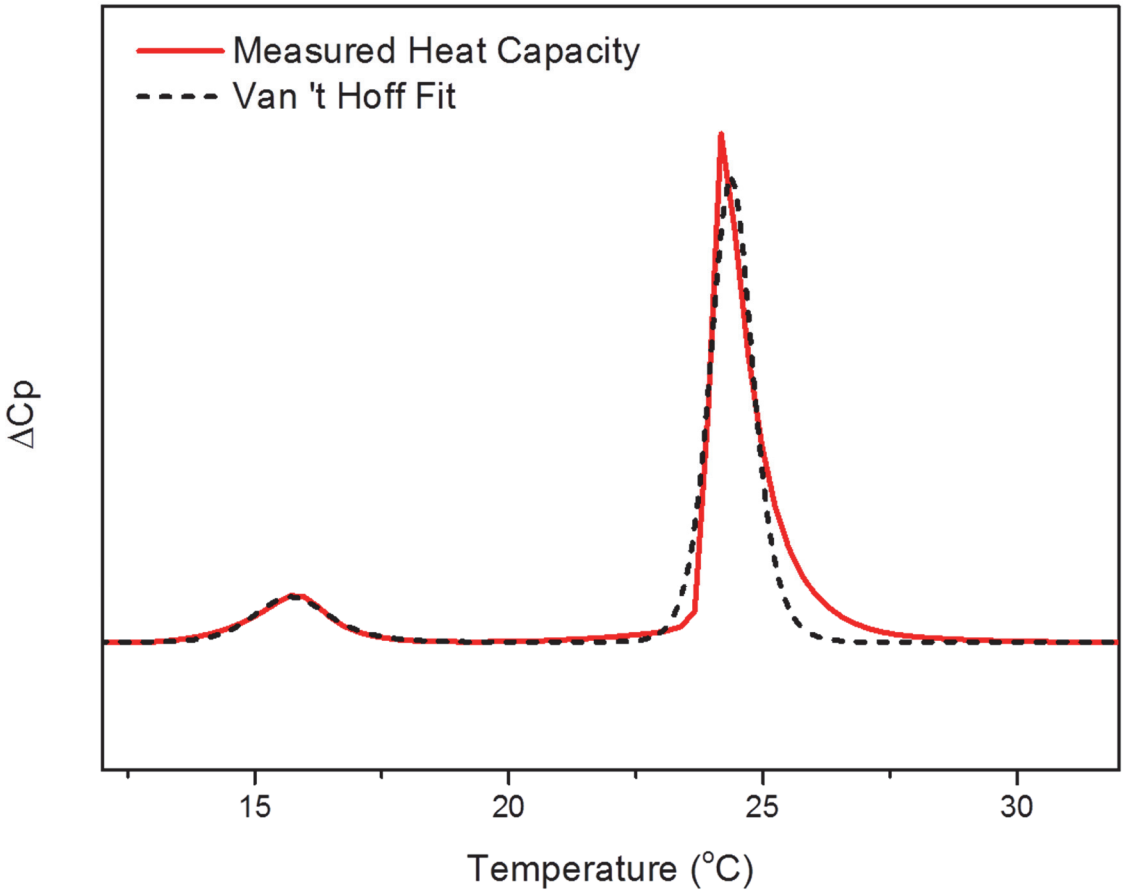

Figure B.6. Measured calorimetric heat-capacity profile (red, solid) and a nonlinear least squares fit of a single Van ‘t Hoff function to each transition (black, dashed).

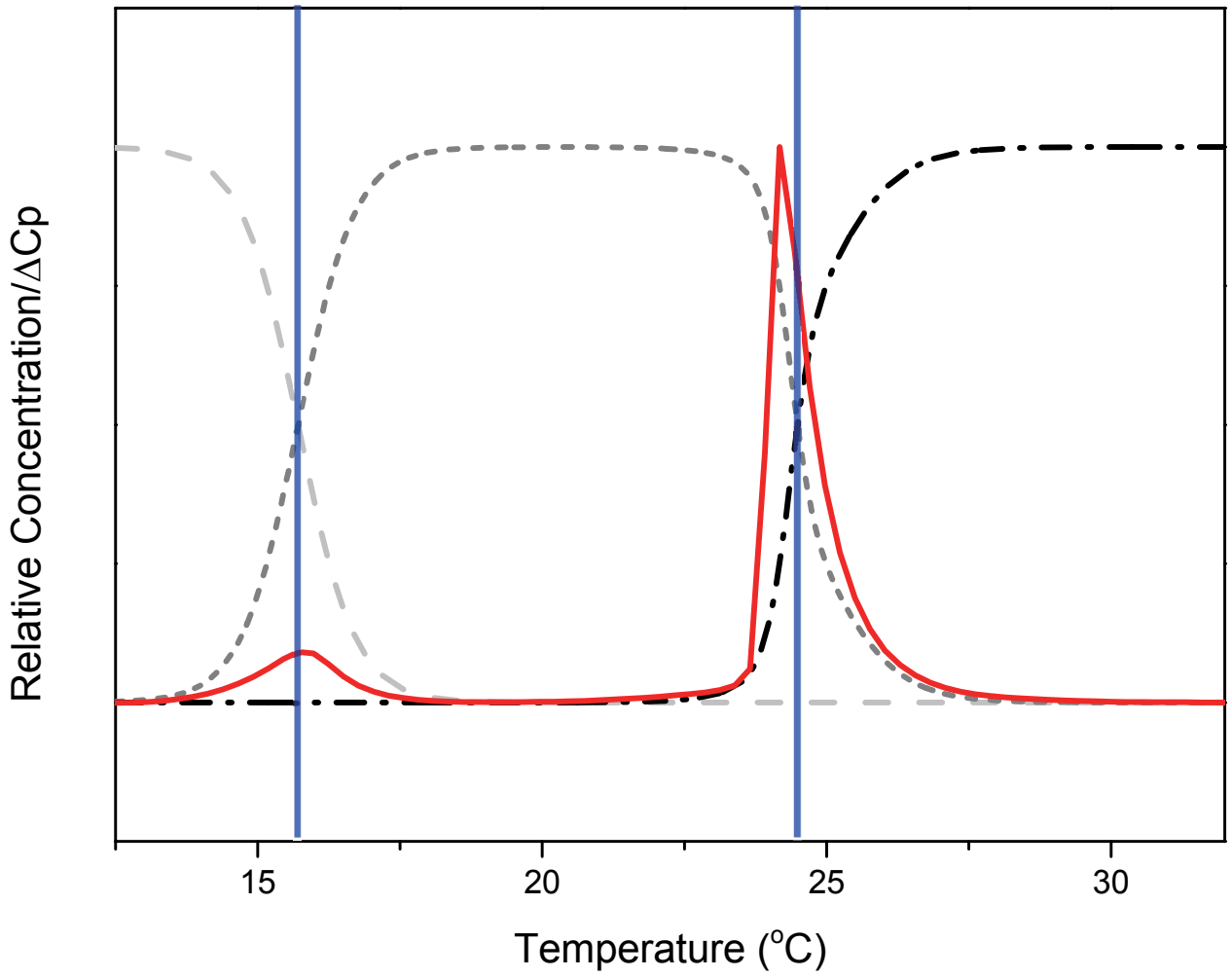

Figure B.7. Calorimetric heat-capacity profiles (red) and the resulting concentration curves (dashed lines) representing the degree of the melting transition with respect to each component. Phase transitions (marked in blue) denote the point where the previous phase and new phase are in 50/50 mol fraction.

B.3.2 Resolving Component Raman Spectra from the Phase Transitions of Optically-trapped DMPC Vesicles

With a model for the temperature-dependent concentration variation derived from the calorimetry data, classical least-squares analysis can be employed to resolve the component spectra corresponding to the individual phases in the temperature-dependent phospholipid phase transition. Each phase is assumed to have a characteristic spectrum that is temperature-independent, and a spectrum of a vesicle measured at any temperature is assumed to be a linear combination of the individual phase components. Under this assumption the data (***D***) are represented by the product of an *r* x *n* matrix of component spectra (***A***) and an *n* x *c* matrix (***C***) of temperature-dependent concentrations; see Eq. B.1. Using the concentration variations of the gel, ripple, and liquid phases (Eq. B.12–B.14) to build the matrix, ***C*** (Figure B.6) a least-squares estimate of the component spectra, $\widehat{\boldsymbol{A}}$, can be determined by right multiplying the data matrix, ***D*** (Figure B.3) by the pseudoinverse of the composition matrix (***C***), Eq. B.2. The spectra resolved by this simple approach, $\widehat{\boldsymbol{A}}$, are plotted in Figure B.7. The consistency of the results with the calorimetry-derived composition model, ***C***, can be tested by multiplying the data matrix, ***D***, by the left pseudoinverse of $\widehat{\boldsymbol{A}}$ (Eq. B.3), to produce a least-squares estimate of the composition matrix, $\widehat{\boldsymbol{C}}$, which can be compared with the model with ***C***. Following this approach, the classical least-squares-derived component spectra projected composition vectors, $\widehat{\boldsymbol{C}}$, that exhibit significant residuals when compared to the calorimetry-derived model, ***C***, as shown in Figure B.5B Most of the residuals were intensity trade-offs, where the concentration of one component trades amplitude with another, leading to large deviations from the model

concentrations including nonphysical (negative) values. These errors are likely due to the similarity between component spectra, the sensitivity of classical least-squares analysis to noise, and variation in temperature (±0.3°C) relative to the PID set-point. These issues also influence the magnitudes of the spectral residuals, $\boldsymbol{R_{\widehat{A}C} = D - \widehat{A}C}$, from a classical least-squares fit, which are plotted Figure B.8.

In cases where component spectra are similar, both noise from the spectral data and fluctuations in the process variable (in this case, temperature) can contribute to large deviations in the resulting least-squares coefficients, $\widehat{\boldsymbol{C}}$. To limit the impact of noise on the resolved components, modifications to classical least-squares search criteria for component spectra have been developed. One example incorporates a penalty that increases the value of χ^2 when component spectra have nonphysical (e.g., negative) values,[32] thus attempting to force the search to find physically meaningful results. This penalty does lead to more meaningful spectra, but in three-component cases, in particular, it is incapable of completely resolving the problem of component trade-offs, where individual components will trade intensity while both remain within user-defined bounds (e.g., both remain positive).

A more direct approach to driving a least-squares search toward a result that is consistent with a concentration model is to modify the least-squares search to include a penalty for deviations of $\widehat{\boldsymbol{C}}$ from $\boldsymbol{C}$. This modified least-squares approach is very similar to one introduced in near-infrared spectroscopy, where concentration residuals were used to augment a classical least-squares optimization to avoid an unmodeled component that might be present in the data.[30] In the present case, the relative variance that will be optimized includes a sum of squared residuals from the overall fit to the data and from the

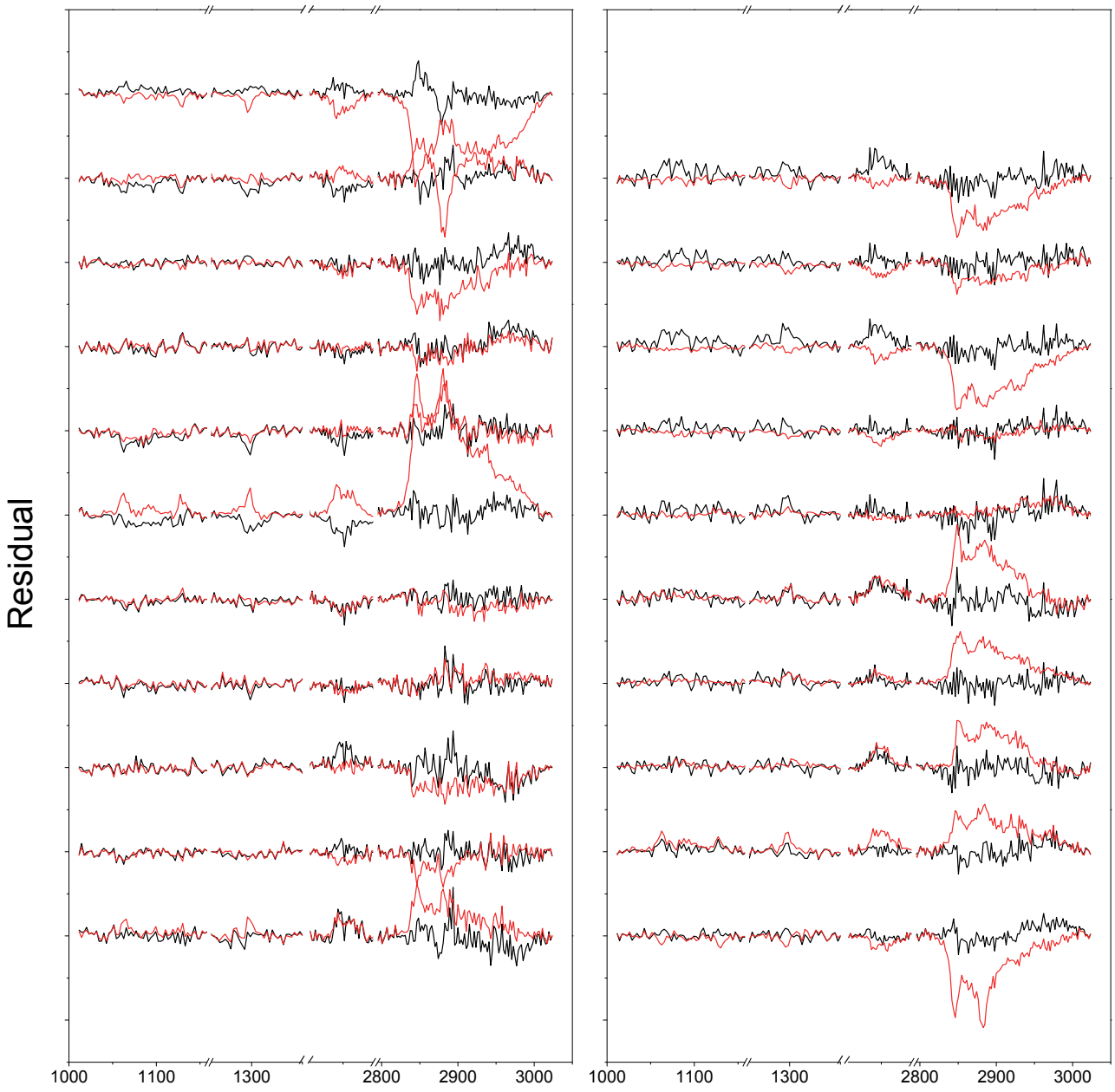

Figure B.8. Spectral residuals arising from classical least-squares analysis (Red, $D - \hat{A}C$) and the concentration-residuals modified least-squares analysis (Black, $D - \hat{A}\hat{C}$) and the relative-root-mean-square error for each analysis method (top right). Note, the greater apparent error in the C-H stretching region is due to the 5-fold greater scattering from these bands; the RRMSE values for this region were comparable: 0.094 and 0.030, for the classical and modified least squares analysis, respectively.

fitted concentrations to the calorimetry model:

$$Rel\,Var_{\hat{D}\hat{C}} = \frac{tr(\boldsymbol{R}_{\hat{\boldsymbol{D}}}^{\boldsymbol{T}}\boldsymbol{R}_{\hat{\boldsymbol{D}}})}{\nu_{\hat{\boldsymbol{D}}}\,(mean\boldsymbol{D})^2} + \frac{tr(\boldsymbol{R}_{\hat{\boldsymbol{C}}}^{\boldsymbol{T}}\boldsymbol{R}_{\hat{\boldsymbol{C}}})}{\nu_{\hat{\boldsymbol{C}}}\,(mean\boldsymbol{C})^2} \qquad \text{[Eq. B.15]}$$

where, $\boldsymbol{R}_{\hat{\boldsymbol{D}}}$ and $\boldsymbol{R}_{\hat{\boldsymbol{C}}}$ are the matrix and vector of residuals, respectively:

$$\boldsymbol{R}_{\hat{\boldsymbol{D}}} = \boldsymbol{D} - \hat{\boldsymbol{D}} = \boldsymbol{D} - \hat{\boldsymbol{A}}\hat{\boldsymbol{C}} \qquad \text{[Eq. B.16]}$$

$$\boldsymbol{R}_{\hat{\boldsymbol{C}}} = \boldsymbol{C} - \hat{\boldsymbol{C}} \qquad \text{[Eq. B.17]}$$

and the traces (*tr*) of the variance-covariance matrices ($\boldsymbol{R}_{\hat{\boldsymbol{D}}}^{\boldsymbol{T}}\boldsymbol{R}_{\hat{\boldsymbol{D}}}$ and $\boldsymbol{R}_{\hat{\boldsymbol{C}}}^{\boldsymbol{T}}\boldsymbol{R}_{\hat{\boldsymbol{C}}}$) give the sums of the squared residuals. The degrees of freedom for the residuals of the overall fit of the data are $\nu_{\hat{\boldsymbol{D}}} = (N_{\boldsymbol{D}} - n_{\hat{A}} - n_{\hat{C}})$ and for the concentration residuals, $\nu_{\hat{\boldsymbol{C}}} = n_{\boldsymbol{C}}$. Because both variances are relative to the squared mean of the data they describe, they contribute equal weight in the optimization. To compute the optimum $\hat{\boldsymbol{A}}$, a Simplex search is implemented where the initial guess for $\hat{\boldsymbol{A}}$ is computed using classical least squares (Eq. 2) and the corresponding $\hat{\boldsymbol{C}}$ is recalculated according to Eq. 3, within a search for the values of $\hat{\boldsymbol{A}}$ that minimize $Var_{\hat{D}\hat{C}}$.

The results of this optimization procedure are component spectra corresponding to the gel, ripple, and liquid-crystalline phases (Figure B.9). To evaluate goodness-of-fit of the spectral components resolved using the concentration-residuals modified least-squares compared with those resolved by classical least-squares, spectral data matrices predicted from each analysis were compared to the original data and the residuals were plotted (Figure B.8). Modified least-squares analysis produced a relative-root-mean-squared error (RRMSE) of 0.047, which was a 2.4-fold improvement over classical least-squares RRMSE of 0.115. In addition to allowing determination of well-resolved component spectra, an effective spectral-analysis method should accurately predict the progress of the temperature dependent process using measured spectra. This is accomplished by projecting

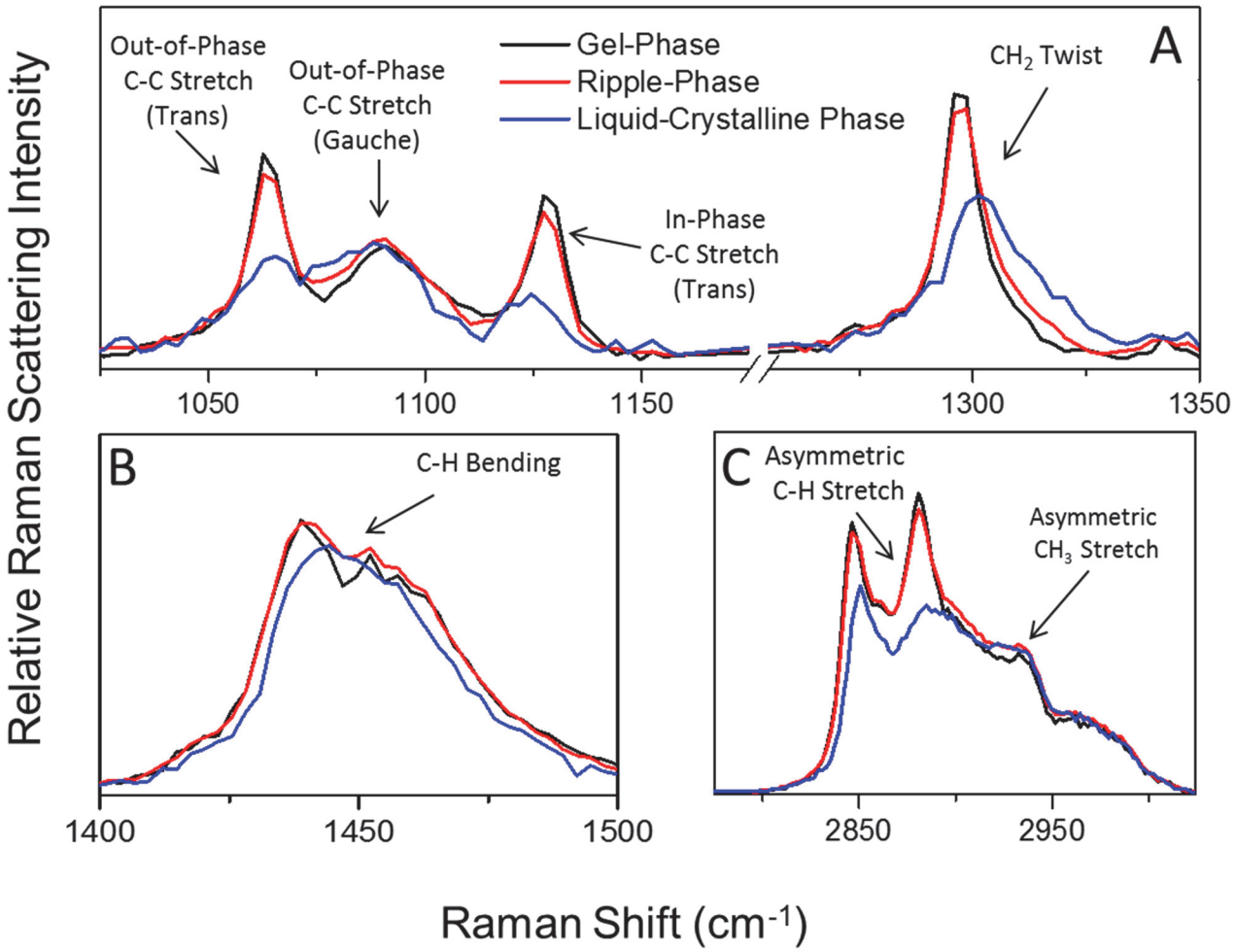

Figure B.9. Component Raman spectra resolved using the concentration-residuals modified least-squares approach of the C-C and C-H twisting regions (a), the C-H bending region (b), and the C-H stretching region (c). Colors correspond to the phases: Gel phase (black), ripple phase (red), and liquid-crystalline phase (blue).

spectral data onto the resolved component spectra (Eq. B.3) to produce temperature-dependent concentrations or contributions to each spectrum in the data matrix. Taking this approach, concentration curves corresponding to the measured spectra were predicted using the concentration-residuals modified least-squares method (Figure B.5C). The concentration-residual modified least-squares approach clearly produces spectra which are more predictive of the bilayer composition, eliminating amplitude trade-offs and minimizing fluctuations in the composition vectors.

B.4 Conclusions

In this work we demonstrate a simple, empirical approach to resolving the spectral components of DMPC melting-transitions using empirical composition vectors derived from differential-scanning calorimetry. The enthalpy changes of each melting transition are employed to construct a series of concentration vectors, which are then used to resolve the component spectra corresponding to each phase of DMPC melting transitions using multidimensional least-squares. Improvement to a classical least-squares fit was accomplished by modifying the analysis to also optimize the consistency of the results with the calorimetry-derived composition model. Spectral data predicted using this modified least-squares method agree with the measured spectra better than those predicted using classical least-squares. The concept of employing calorimetry-derived composition vectors in the analysis of temperature-dependent spectral data could be readily applied in many other areas of materials characterization, where one is seeking to learn about structural changes that occur through temperature-dependent phase transitions.

B.5 References

1. D.M. Haaland, R.G. Easterling, D.A. Vopicka. "Multivariate Least-Squares Methods Applied to the Quantitative Spectral Analysis of Multicomponent Samples". Appl. Spectrosc. 1985. 39(1): 73-84.

2. K.R. Beebe, B.R. Kowalski. "An Introduction to Multivariate Calibration and Analysis". Anal. Chem. 1987. 59(17): 1007A-1017A.

3. J.E. Franke. "Inverse Least Squares and Classical Least Squares Methods for Quantitative Vibrational Spectroscopy", Handbook of Vibrational Spectroscopy John Wiley & Sons, Ltd, 2006.

4. N.R. Draper, H. Smith. Applied Regression Analysis, 3rd Ed. Wiley New York, 1998.

5. J.C. Fister, J.M. Harris. "Resolving Component Overlap in Multiwavelength Kinetic Spectroscopy: Application to Raman Scattering from Intermediates in Triplet-State Photoreactions". Photochem. Photobiol. 1997. 65(1): 47-56.

6. J.A. Kleimeyer, J.M. Harris. "Monitoring the Formation and Decay of Transient Photosensitized Intermediates Using Pump-Probe UV Resonance Raman Spectroscopy. II: Kinetic Modeling and Multidimensional Least-Squares Analysis". Appl. Spectrosc. 2003. 57(4): 448-453.

7. D. Rivera, J.M. Harris. "In Situ Studies of Pyridine Adsorption to Bare and Cyano-Derivatized Silica Sol−Gel Films Using Attenuated-Total-Internal-Reflection Fourier-Transform Infrared Spectroscopy". Langmuir. 2001. 17(18): 5527-5536.

8. D. Rivera, P.E. Poston, R.H. Uibel, J.M. Harris. "In Situ Adsorption Studies at Silica/Solution Interfaces by Attenuated Total Internal Reflection Fourier Transform Infrared Spectroscopy: Examination of Adsorption Models in Normal-Phase Liquid Chromatography". Anal. Chem. 2000. 72(7): 1543-1554.

9. D. Rivera, J.M. Harris. "In Situ ATR-FT-IR Kinetic Studies of Molecular Transport and Surface Binding in Thin Sol−Gel Films: Reactions of Chlorosilane Reagents in Porous Silica Materials". Anal. Chem. 2001. 73(3): 411-423.

10. N. Albon, J.M. Sturtevant. "Nature of the gel to liquid crystal transition of synthetic phosphatidylcholines". Proc. Natl. Acad. Sci. U.S.A. 1978. 75(5): 2258-2260.

11. H. Naghibi, A. Tamura, J.M. Sturtevant. "Significant discrepancies between van't Hoff and calorimetric enthalpies". Proc. Natl. Acad. Sci. U.S.A. 1995. 92(12): 5597-5599.

12. C. Johann, P. Garidel, L. Mennicke, A. Blume. "New approaches to the simulation of heat-capacity curves and phase diagrams of pseudobinary phospholipid mixtures". Biophys. J. 1996. 71(6): 3215-3228.

13. S. Mabrey, J.M. Sturtevant. "Investigation of phase transitions of lipids and lipid mixtures by sensitivity differential scanning calorimetry". Proc. Natl. Acad. Sci. U.S.A. 1976. 73(11): 3862-3866.

14. W.H. Lawton, E.A. Sylvestre. "Self Modeling Curve Resolution". Technometrics. 1971. 13(3): 617-633.

15. E.R. Malinowski. Factor analysis in chemistry, (2nd edition). Wiley-Interscience, 1991.

16. E.R. Malinowski, R.A. Cox, U.L. Haldna. "Factor analysis for isolation of the Raman spectra of aqueous sulfuric acid components". Anal. Chem. 1984. 56(4): 778-781.

17. Z. Zhao, E.R. Malinowski. "Detection and Identification of a Methanol−Water Complex by Factor Analysis of Infrared Spectra". Anal. Chem. 1999. 71(3): 602-608.

18. J.A. Kleimeyer, J.M. Harris. "Monitoring the Formation and Decay of Transient Photosensitized Intermediates Using Pump-Probe UV Resonance Raman Spectroscopy. I: Self-Modeling Curve Resolution". Appl. Spectrosc. 2003. 57(4): 439-447.

19. R.H. Uibel, J.M. Harris. "Resolution of Intermediate Adsorbate Structures in the Potential-Dependent Self-Assembly of n-Hexanethiolate on Silver by in situ Surface-Enhanced Raman Spectroscopy". Appl. Spectrosc. 2004. 58(8): 934-944.

20. C.B. Fox, R.H. Uibel, J.M. Harris. "Detecting Phase Transitions in Phosphatidylcholine Vesicles by Raman Microscopy and Self-Modeling Curve Resolution". J. Phys. Chem. B. 2007. 111(39): 11428-11436.

21. P.D. Wentzell, J.-H. Wang, L.F. Loucks, K.M. Miller. Can. J. Chem. 1998. 76(8): 1144-1155.

22. K. Sasaki, S. Kawata, S. Minami. "Estimation of component spectral curves from unknown mixture spectra". Appl. Opt. 1984. 23(12): 1955-1959.

23. J.M. Sturtevant. "Biochemical applications of differential scanning calorimetry". Ann. Rev. Phys. Chem. 1987. 38(1): 463-488.

24. A. Laouini, C. Jaafar-Maalej, I. Limayem-Blouza, S. Sfar, C. Charcosset, H. Fessi. "Preparation, characterization and applications of liposomes: state of the

art". J. Coll. Sci. and Biotechnol. 2012. 1(2): 147-168.

25. A. Akbarzadeh, R. Rezaei-Sadabady, S. Davaran, S.W. Joo, N. Zarghami, Y. Hanifehpour, M. Samiei, M. Kouhi, K. Nejati-Koshki. "Liposome: classification, preparation, and applications". Nanoscale Res. Lett. 2013. 8(1): 102.

26. M.P. Houlne, C.M. Sjostrom, R.H. Uibel, J.A. Kleimeyer, J.M. Harris. "Confocal Raman Microscopy for Monitoring Chemical Reactions on Single Optically Trapped, Solid-Phase Support Particles". Anal. Chem. 2002. 74(17): 4311-4319.

27. J.P. Kitt, J.M. Harris. "Confocal Raman Microscopy for in Situ Detection of Solid-Phase Extraction of Pyrene into Single C18–Silica Particles". Anal. Chem. 2014. 86(3): 1719-1725.

28. K.P.J. Williams, G.D. Pitt, D.N. Batchelder, B.J. Kip. "Confocal Raman microspectroscopy using a stigmatic spectrograph and CCD detector". Appl. Spectrosc. 1994. 48(2): 232-235.

29. H. Akutsu. "Direct determination by Raman scattering of the conformation of the choline group in phospholipid bilayers". Biochemistry. 1981. 20(26): 7359-7366.

30. D.K. Melgaard, D.M. Haaland, C.M. Wehlburg. "Concentration Residual Augmented Classical Least Squares (CRACLS): A Multivariate Calibration Method with Advantages over Partial Least Squares". Appl. Spectrosc. 2002. 56(5): 615-624.

31. J.M. Sturtevant. "A scanning calorimetric study of small molecule-lipid bilayer mixtures". Proc. Natl. Acad. Sci. U.S.A. 1982. 79(13): 3963-3967.

32. F.J. Knorr, J.M. Harris. "Resolution of multicomponent fluorescence spectra by an emission wavelength-decay time data matrix". Anal. Chem. 1981. 53(2): 272-276.